6-24-2016

Delayed Feedback Control Schemes for Vibration Suppression and Energy Harvesting with Piezoelectric Resonators

Ayhan S. Kammer
University of Connecticut, kammer@engineer.uconn.edu

Delayed Feedback Control Schemes for Vibration Suppression and Energy Harvesting with Piezoelectric Resonators

Ayhan Sebastian Kammer, PhD

University of Connecticut, 2016

Time delays in feedback control systems have intrigued researchers especially over the past five decades. Some recent studies have discovered that deliberate introduction of delays within certain control laws yields favorable results. This work follows the same philosophy and stems from a pedigree of research where delays are viewed as a tool, and their unique features are exploited. Delayed Resonators use the destabilizing effect of delays to induce resonance in an active vibration absorber, providing complete vibration suppression against time varying tonal disturbances. Inspired by these developments, this work embarks on another exploration on systems that harvest energy from mechanical vibrations. In this research, an analytical framework is developed on generic active mechanical vibration absorbers with delayed feedback control. The interplay between the generated and consumed energy is investigated from a physics viewpoint. It is shown that energy harvesting capacity can be significantly enhanced by introducing a properly designed time-delayed feedback.

A critical feature in this work is the use of piezoelectric materials. Considerable research has been devoted to the use of piezoelectric components for both vibration control and energy harvesting. Piezoelectricity provides a bi-directional coupling between mechanical strain and electrical fields. This allows the use of resistive-inductive electrical circuits, which are reconfigured to serve as resonators for mechanical structures. In this work, time-delayed control laws are devised for such systems, primarily to serve two purposes: (a) effective vibration suppression and (b) increased energy harvesting. The essence of the scientific contribution lies at

the point that the electrical circuit is actively sensitized to replace a conventional proof-mass absorber (or harvester). This idea could evolve into a design mechanism which has many advantages, such as compactness, reduced weight, and deployment practicality. An experimental setup, consisting of a cantilever beam with piezoelectric patches connected to a shunt circuit, is constructed to demonstrate the core concepts in this effort. Delayed proportional control is applied within the electrical circuit to test the analytical findings. As expected, many practical issues are encountered and addressed during this effort. Favorable experimental results on vibration control and energy harvesting are presented and discussed in detail.

Delayed Feedback Control Schemes for Vibration Suppression and Energy Harvesting with Piezoelectric Resonators

Ayhan Sebastian Kammer

B.S., Mechanical Engineering, Middle East Technical University, 2012

A Dissertation

Submitted in Partial Fulfillment of the

Requirements for the Degree of

Doctor of Philosophy

at the

University of Connecticut

2016

APPROVAL PAGE

Doctor of Philosophy Dissertation

Delayed Feedback Control Schemes for Vibration Suppression and Energy Harvesting with Piezoelectric Resonators

Presented by

Ayhan Sebastian Kammer, B.S.

Major Advisor

_____

Nejat Olgac

Associate Advisor

_____

Jiong Tang

Associate Advisor

_____

Chengyu Cao

Associate Advisor

_____

Xu Chen

University of Connecticut
2016

Acknowledgements

This thesis serves as the culmination to my doctoral degree, which has been a life-changing journey in all aspects. Many people have guided and supported me through life and this work. I would not be typing these words without them and the least I can do to show my appreciation is to acknowledge their contributions here.

First and foremost, I would like to thank my advisor and mentor, Professor Nejat Olgac for accepting me into his group and opening the doors to the exclusive world of scientific research. His leadership, unique in many aspects such as the amount of time devoted to his students, has enabled me to accomplish phenomenal things in a short duration of time. Just four years ago I started out as an undergraduate engineer, and under his wings I have grown into the well-rounded researcher and individual that I am today. Indeed they say time flies when you're productive and enjoying your work.

I am very thankful to my advisory committee, Professors Jiong Tang, Chengyu Cao and Xu Chen, for their guidance and supervision throughout this work. I am especially grateful to Prof. Tang and his graduate student Jiawen Xu for sharing their expertise and knowledge on piezoelectric materials with me.

The laboratory is where I spent most of my time and learned a great deal. This work would not have been possible without my collaborators from ALARM: Umut Zalluhoglu, Qingbin Gao and Rudy Cepeda-Gomez. I would specifically like to thank Umut as I firmly believe that our teamwork on many projects enabled rapid progress and fast learning.

Many others helped me through my journey at UConn. I would like to thank Professors Robert Gao (now with CWRU MAE department) and Shalabh Gupta (UConn ECE department)

for their insightful lectures, and their assistance with other professional matters. Thanks to Peter Glaude from the Machine Shop for providing me with quality materials for my experiments. The ME department staff was always keen to help whenever needed. I would like to thank Tina Barry, Thomas Mealy, Laurie Hockla, Steve White, Kelly Tyler and Elizabeth Dracobly.

This work would not have been possible without the support from my family. I would like to thank my mother Hildegard Kammer and my father Kayhan Bayırlı. I am very fortunate to be raised with their unconditional love and support. I would like to shout out to my siblings Taylan, Nikolas and Ellen; especially Taylan for interesting and deep conversations about technology, politics and many aspects of life. I would like to acknowledge my grandparents for always being there for me and providing me with a rich sense of family. I am infinitely grateful to my paternal grandmother Melahat Bayırlı for providing care to me throughout my teen years. I would not have made it through middle should and high school without her. I am very thankful to my maternal grandparents, Ulrich and Gertrud Kammer, for their love and consistent support to my education. They have always made me feel at home in Laubach and I have countless happy memories with them.

I would like to thank my girlfriend Mary Orechia for her love and support throughout my doctoral studies. I am very fortunate to have her as a guide and companion while exploring the New England region and going on adventures. I would also like to thank her family, the Orechias for inviting me to many of their family celebrations and events. They have made me feel at home in a place far away from my native countries. A shout out to my cheeky group of friends from my hometown Izmir: Ege Bilican, Semih Aykut, Serdar Cakan, Mert Erbil, Gurcan Gurses and Emre Dokmeci. I would also like to thank Enes Gokkus, my close friend from college and now fellow expat in the USA. Thanks for all the fun and sense of comradeship.

Table of Contents

Chapter 1. Introduction and Preliminaries

1.1.Problem Statement

This work details efforts in several fronts that revolve around the concept of utilizing time delays within feedback control laws in order to achieve certain objectives. The main inspiration behind this research is the Delayed Resonator (DR), an innovative idea to inject deliberate time-delays within feedback controllers to yield an advanced and tunable vibration absorber. Following this philosophy, this work pursues to implement the same idea in a completely new platform: namely, energy harvesting from mechanical vibrations. The main theoretical contribution is to develop time-delayed feedback control schemes that would increase the capacity of energy harvesting systems. An extensive analytical framework is constructed and many aspects are analyzed within this context. A secondary contribution of this work is to introduce time-delayed control laws to active piezoelectric networks. Piezoelectric materials have been a prominent subject of both vibration suppression and energy harvesting research. These two objectives are very interesting platforms for delayed feedback control implementations, as apparent from the DR literature and the energy harvesting capacity research that is pursued here.

1.2.Review on Delayed Resonator and Related Developments

The Delayed Resonator concept evolved in the 90s after Olgac and Holm-Hansen (1994) first proposed the use of a time-delayed feedback control over an active vibration absorber in order to induce resonance to it. It is well established in vibration control literature, that resonant structures offer ideal vibration absorption characteristics (Inman, 2014). On the other hand, in control theory, time-delays are usually regarded as contaminants that may cause closed-loop

instabilities in feedback systems (Richard, 2003). The DR idea originates from these two facts and suggests an alternative means to achieve ideal vibration control. An actuator is added to the absorber substructure, to implement a feedback control action. By intentionally delaying the feedback signal, marginal stability (i.e., resonance) may be induced in the absorber substructure at a controllable frequency. Naturally, a critical argument accompanying this idea is that the control parameters need to be tuned in-situ, so that the desired resonance and the consequential vibration suppression characteristics can be achieved. The combined system containing the primary and absorber structures effectively becomes a time-delayed system. The delay effect introduces infinite-dimensional dynamics and the system characteristics are governed by an infinite spectrum. This point brings complex challenges for control synthesis, such as assuring asymptotic stability for the closed-loop operation.

Within 2 decades following the introduction of DR theory, many investigators pursued the underlying philosophy from various interesting aspects including those issues raised above. The concept was proven by the group on several experiments, including some distributed systems (i.e., infinite dimensional) as primary structures (Olgac et al., 1997; Olgac and Jalili, 1998). Torsional vibration problems were also considered. Hosek et al. (1997) first proposed a practicable centrifugal delayed resonator, and later considered applications on multi-degree-of-freedom structures (Hosek et al., 1999). Filipovic and Olgac (2002) conducted experimental studies on a test setup and reported performance characteristics. Robustness of the control parameters to system uncertainties and variations were addressed by introducing automatic tuning methods. Renzulli et al. (1999) proposed a multiple-step tuning scheme based on gradient analysis of frequency transfer functions. Hosek and Olgac (2002) later developed a single-step tuning method based on real-time frequency domain analysis.

The delayed resonator concept also influenced widespread use of user-injected time-delays in feedback control laws in the broader research community. Jalili and Esmailzadeh (2001) studied active vehicle suspensions with actuator time-delay. Henry et al. (2001) proposed to implement a DR-based feedback control method to suppress cargo oscillations in ship-mounted cranes. Masoud et al. (2005) later demonstrated this concept experimentally. Librescu and Marzocca (2005) discuss time-delay feedback control as a potential method to reduce vibrations in aeroelastic structures. Udwadia and Phohomsiri (2006) proposed a time-delayed proportional control to mitigate vibrations in structures stemming from earthquakes. Talole et al. (2006) applied similar principles for navigation guidance control. Bisgaard et al. (2010) applied time-delay regulation to devise an adaptive control system, reducing helicopter slung load oscillations. Delayed feedback control and DR theory have also been investigated as potential methods to mitigate railroad vehicle vibrations (Huang and Zhao, 2013; Eris et al., 2014). Vyhlídal et al. (2014) investigated design guidelines for delayed resonators based on spectral analysis methods.

1.3.Theory of the Delayed Resonator

A review on DR theory and some preliminaries are presented in this section. Consider a DR vibration absorber attached to the ground as depicted in Figure 1.1. A displacement measurement is used in the feedback line with a simple control logic: It involves a proportional-type control to the displacement along with an artificially introduced delay. This introduces two adjustable control parameters: the gain g and delay τ. The control action is executed through a force actuator for the active tuning of the device.

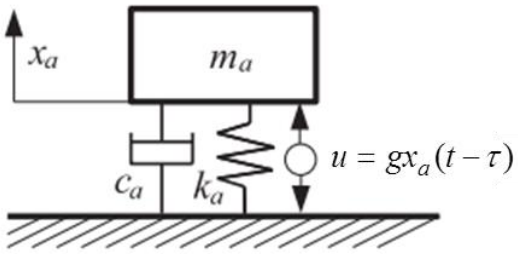

Figure 1.1. Delayed resonator vibration absorber with displacement feedback.

The governing equation for the absorber is

$$m_a\ddot{x}_a(t) + c_a\dot{x}_a(t) + k_a x_a(t) - g x_a(t-\tau) = 0\,. \tag{1.1}$$

Applying Laplace transformation, the characteristic equation for this dynamics is obtained as

$$m_a s^2 + c_a s + k_a - g\,\mathrm{e}^{-\tau s} = 0\,. \tag{1.2}$$

Because of the added feedback delay, this is a quasi-polynomial equation. As such it has infinitely many roots. For a desired DR tuning, the feedback gain g and the delay τ have to be adjusted such that the system has a pair of characteristic roots at $\pm\omega\mathrm{i}$. Substituting $s = \omega\mathrm{i}$ in (1.2), the necessary control parameters to achieve this are solved using the magnitude and phase conditions as

$$g(\omega) = (-1)^{l-1}\sqrt{(k_a - m_a\omega^2)^2 + (c_a\omega)^2}\,,$$

$$\tau(\omega) = \frac{1}{\omega}\left[\tan^{-1}\left(\frac{c_a\omega}{m_a\omega^2 - k_a}\right) + (l-1)\pi\right],\ l = 1,2,\ldots. \tag{1.3}$$

Here, the counter l is called the *branch number*. For a given ω, the delay parameter repeats indefinitely on so-called *branches*, because $\mathrm{e}^{-\tau\omega\mathrm{i}}$ is a periodic function. When the control

parameters are tuned according to (1.3), the absorber exhibits a *resonant* mode at frequency ω. If these pair of resonant characteristic roots, $s = \pm\omega i$, are the *dominant* roots (i.e., right-most in the complex plane), this sub-structure should absorb all vibration at this frequency from a primary structure it is attached to. However if the roots $s = \pm\omega i$ are not dominant, and other characteristic roots in the right-half complex plane exist, the absorber would be unstable and the operation would fail. This concern necessitates a systematic stability analysis, which is discussed next.

The loci of (τ, g) points for an example DR setup are depicted in Figure 1.2. Here, the control parameters are presented in normalized form to point out some typical characteristics.

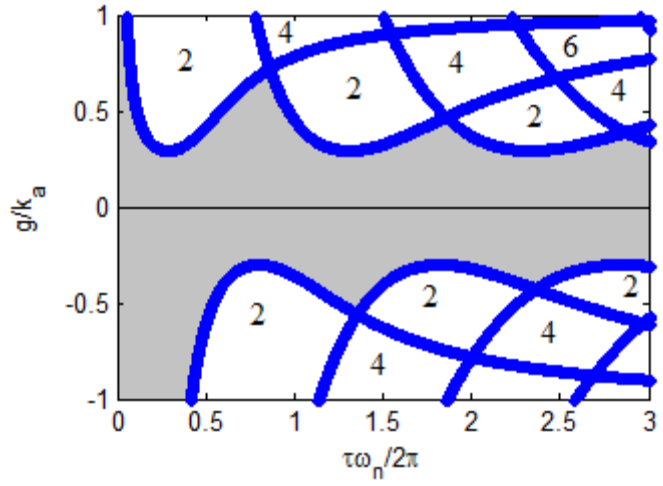

Figure 1.2. Normalized delay and gain parameters for delayed resonator tuning (m_a = 1 kg, c_a = 12 Ns/m, k_a = 1600 N/m). Stable region shaded. Number of unstable roots marked.

This figure conveys some important information regarding the stability of the DR substructure. At the origin (τ, g) = (0, 0) and over the g = 0 line, the actuator force equals to zero. The absorber reduces to a simple mass-spring-damper setup, which is asymptotically stable in nature. It has two characteristic roots in the left-half complex plane ($\mathbf{C}^-$). However, for parameter compositions with $\tau > 0$, $g > 0$, the DR becomes an active time-delayed system, and

consequently the stability analysis becomes more involved. As mentioned earlier, the characteristic equation is a quasi-polynomial with an infinite spectrum. In order to ensure asymptotic stability, all the infinitely many characteristic roots have to lie in $\mathbf{C}^{-}$. On the other hand, the root continuity theorem (Kolmanovskiĭ and Nosov, 1986) dictates that these roots move in a continuous manner in the complex plane if parameters (τ, g) are perturbed. Then one can recognize that the system's stability can change if and only if a set of characteristic roots cross from the left to the right-half plane ($\mathbf{C}^{+}$) through the imaginary axis. The (τ, g) compositions obtained as in (1.3) (and depicted in Figure 1.2) correspond to the specific instances where such root crossings occur. Only for points on these unique (τ, g) loci, the system has a set of purely imaginary characteristic roots $s = \pm\omega\mathrm{i}$. Taking the stable origin as a reference starting point, the number of right-hand (i.e., unstable) characteristic roots corresponding to an arbitrary point in the (τ, g) space can be deduced (also demonstrated on Figure 1.2). This method is also known as the D-subdivision concept in time-delayed systems literature (Kolmanovskiĭ and Nosov, 1986; Filipovic and Olgac, 2002).

The above discussion concerns resonance conditions and stability in the DR absorber structure only. A more important aspect is the assurance of stable operation when the absorber is mounted on a primary structure, as depicted in Figure 1.3. The coupled absorber-primary system has different dynamics that depend on a variety of factors such as the degrees-of-freedom in the primary structure or the type of sensors used. Thus the control parameters (τ, g) used to make the absorber resonant could potentially induce instability in the combined system dynamics. Without loss of generality, the combined system's characteristic equation can be represented as

$$A(s) + B(s)g\,\mathrm{e}^{-\tau s} = 0 \tag{1.4}$$

where $A(s)$ and $B(s)$ are polynomials and their exact form depends on the specifics of the system under consideration (Olgac & Holm-Hansen, 1995).

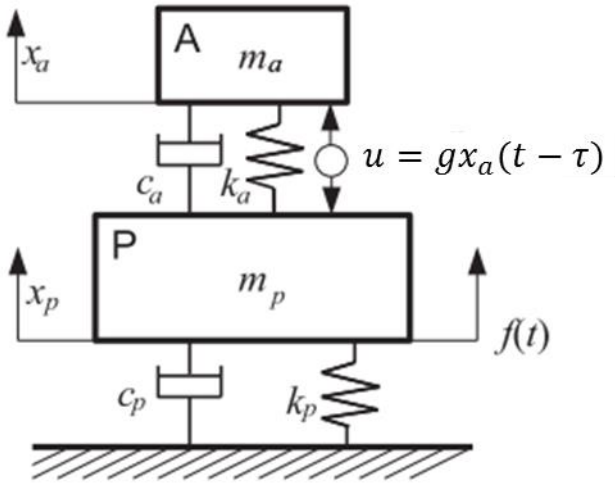

Figure 1.3. Delayed resonator vibration absorber mounted on a primary structure that is subject to external forcing.

The characteristic equation in (1.4) represents a single-delayed dynamics without commensurate effects (e.g., $e^{-2\tau s}$, $e^{-3\tau s}$, …), which is essentially the simplest possible construct among time delayed systems. Similar to the DR tuning conditions, the stability boundaries of this dynamics can be derived by substituting $s = \omega i$ in (1.4) and evaluating the magnitude and phase conditions. From this,

$$g_{cs} = (-1)^{l-1}\left|\frac{A(\omega)}{B(\omega)}\right|, \quad \tau_{cs} = \frac{1}{\omega}\left[\angle B(\omega) - \angle A(\omega) + l\pi\right], \quad l = 1,2,... \tag{1.5}$$

arise as the parametric expressions for the boundaries of the combined system's stability. Once these parametrically-defined potential stability boundaries are determined, one can use the D-

subdivision method to construct parametric stability maps in (τ, g) space for the combined system.

The two stability maps of the DR absorber and the combined system are typically presented together in superimposed form; enabling the user to identify the existing options for (τ, g) parameters so that the DR substructure operates at marginal stability, while the combined system is asymptotically stable. A sample stability map is depicted in Figure 1.4. This offers a very convenient and practicable method to identify the DR control parameter compositions. We also wish to stress that the control parameters seen in (1.3) are functions of the excitation frequency ω only. As a result, the combined system stability imposes some frequency constraints within which a particular DR can operate.

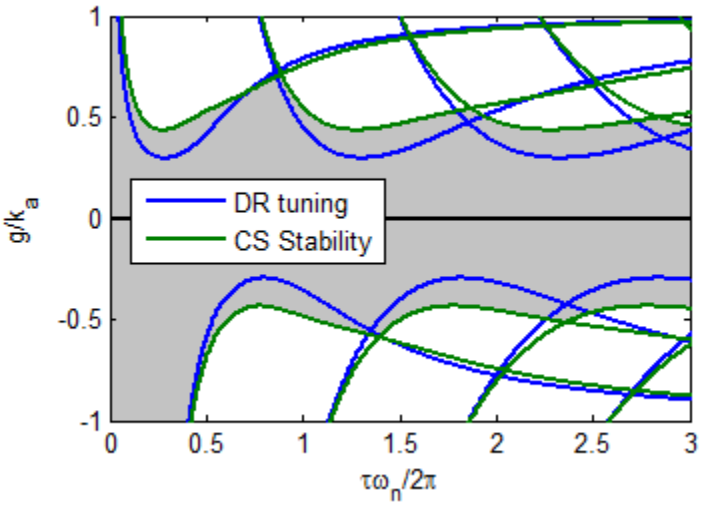

Figure 1.4. Normalized delay and gain parameters for delayed resonator tuning and combined system (CS) stability margins (m_a = 1 kg, c_a = 12 Ns/m, k_a = 1600 N/m, m_p = 10 kg, c_p = 240 Ns/m, k_p = 9000 N/m). Shaded region depicts (τ, g) compositions where CS is stable.

1.4.Delayed Feedback Vibration Absorbers

Delayed Feedback Vibration Absorbers (DFVA) can be regarded as an extension of the delayed resonator concept. In essence, the basic components and structure are identical to a DR, and the control law is again a delayed proportional feedback. In this case, the control parameters (τ, g) are not tuned to exert complete resonance, as opposed to DR tuning. In other words, the (τ, g) composition is chosen within the shaded region in Figure 1.2, instead of the blue curves. The choice of control preserves asymptotic stability in the absorber substructure; however the dynamics are altered to provide a certain objective in vibration control. Jalili and Olgac (2000) demonstrated that the frequency response of a primary system can be significantly reduced over a frequency range by implementing a DFVA tuning approach. The control parameter synthesis in this case was achieved by an optimization routine. Jalili and Esmailzadeh (2000) later extended the same principle to active vehicle suspensions.

1.5.Advances on the Stability of Time Delayed Systems

The discussions in previous sections regarding stability encompass a rather limited sub-class of time delayed systems (TDS). Notice that the DR and DFVA concepts only involve a single user-injected feedback delay. Hence the characteristic equation can be represented in the form as in (1.4), rendering a relatively uncomplicated stability assessment procedure. This is a clear example of a system with single non-commensurate time delay; a special case that constitutes the simplest form among TDS. In many cases however, the system might be subject to more complex forms of time delays in the dynamics. For instance, a single time delay may appear commensurate form (e.g., $e^{-\tau s}$, $e^{-2\tau s}$ …) in the same characteristic equation. Or multiple independent delays may exist in a system, which appear in the characteristic equation in various

forms (e.g., $e^{-\tau_1 s}$, $e^{-\tau_2 s}$, $e^{-(\tau_1+\tau_2)s}$) (Niculescu, 2002; Olgac et al., 2014). In such cases, the stability analysis problem becomes significantly more involved as the characteristic equation cannot be separated as in (1.4). As a result, determining delay compositions at which imaginary root crossings may occur is a challenging problem.

Many different approaches have been proposed to study general TDS and stability problems. Richard (2003) presents a comprehensive overview on TDS literature that is available up to the early 2000s. In this section we shall mention a more recent development on this topic, the Cluster Treatment of Characteristic Roots (CTCR) paradigm (Olgac and Sipahi, 2002; Sipahi and Olgac, 2006). This is a unique methodology in the sense that it is completely analytical and can be applied to linear time invariant (LTI) TDS as a whole. It has been developed by the same research group that first proposed the delayed resonator concept. Delay-dependent stability assessment based on the CTCR paradigm generally consists of two key steps:

1- The exhaustive detection of all delay compositions (*hypercurves* in the delay space) that render an imaginary root in the characteristic equation (i.e., potential root crossing).

2- The processing and organization of these hypercurves to construct a stability tableau which enables a systematic and efficient delay-dependent stability analysis.

The first step, the detection of hypercurves in delay space, is crucial, however not sufficient in itself. Notice that any delay value that renders an imaginary characteristic root will repeat indefinitely due to the periodicity of the delay-induced exponential terms in the characteristic equation. This means that there is an infinite number of such hypercurves. The CTCR paradigm recognizes certain unique features of TDS and brings discipline to this chaotic picture.

Regarding the exhaustive detection of stability switching hypercurves (SSH), literature on CTCR has proposed several alternative methods. A first sub-step within this process is the conversion of the quasi-polynomial characteristic equation to a multinomial, using an exact substitution. For instance, Rekasius substitution (Rekasius, 1980) is used by Sipahi and Olgac (2006), while tangent half-angle substitutions are used by Cepeda-Gomez and Olgac (2013). These substitutions introduce new agent parameters that have one-to-one correspondence with the delay values. The second sub-step is to apply elimination methods in order to convert the multinomial into an implicit function in terms of the agent parameters only. Because $s = \omega$i is substituted in the characteristic equation, it is a multinomial in terms of ω and the agent parameters. If ω is eliminated, the agent parameters can be solved from the remaining equation. One approach is to use the Routh array (Sipahi and Olgac, 2006), while other possible methods include Sylvester's resultant matrix (Cepeda-Gomez and Olgac, 2013) or Dixon's resultant matrix (Gao and Olgac, 2015). Another alternative method to exhaustively determine the SSH is to use Kronecker summation (Ergenc et al., 2007).

Once the SSH are determined exhaustively, the CTCR paradigm is applied to facilitate an efficient and effective stability assessment procedure. This is achieved through two key propositions of CTCR (Olgac and Sipahi, 2002; Sipahi and Olgac, 2006).

Proposition 1: defines the concept of *kernel* hypercurves and proves that they exist in finite numbers. Kernel hypercurves are all delay compositions that satisfy $\tau\omega < 2\pi$, where ω is the frequency of the associated imaginary root crossing ($s = \omega$i). It is proven in the cited documents that although infinitely many hypercurves exist, they are all spawned from these finite number of kernel hypercurves. These secondary hypercurves are called *offspring* and they

can be obtained by simple offsets in the delay space as $\tau + 2\pi l/\omega$ ($l = 1, 2\ldots$). This discovery is remarkable as it brings considerable discipline to the infinite number of SSH.

Proposition 2: dictates that the root tendency (RT)—the tendency of a delay-induced imaginary characteristic root to move to the right or left-hand complex plane as the delay is increased—remains invariant among kernel and offspring hypercurves. The root tendency is an analytical way to determine whether the delay-induced imaginary root will make a de-stabilizing (right-hand) or stabilizing (left-hand) movement as the delay value is infinitesimally increased. This is crucial to determine whether crossing over a SSH in delay space will increase or decrease the number of unstable (right-hand) characteristic roots and ensures the creation of an accurate stability tableau. The invariance between kernel and offspring hypercurves is an important and useful property that eliminates the redundancy of re-calculating RT on offspring hypercurves. Once the RT on the kernel curve is known, it can be automatically deduced on the offspring.

The revelations made available by the CTCR paradigm, in conjunction with the methods developed to exhaustively determine SSH are invaluable tools for a delay-dependent stability analysis. They have been applied to many different problems involving delays such as chatter stability in simultaneous machining (Olgac and Sipahi, 2005), stability of consensus protocols (Cepeda-Gomez and Olgac, 2013) and thermo-acoustic instabilities (Olgac et al., 2014) among others.

Chapter 2. Energy Harvesting from Resonators and the Effects of Delayed Feedback

2.1.Introduction

2.1.1. Review on energy harvesting research

In recent decades, mankind has come to realize that energy resources are limited and current reserves cannot be taken as granted. Concurrently, the negative environmental effects of existing energy generation methods are also becoming a public concern. Modern industrialized economies heavily rely on earth's fossil fuels, which are not only limited but also cause significant pollution and contribute to global warming. As a result; engineers, scientists and politicians are joining efforts to develop more sustainable sources of energy. These efforts are striving on many different fronts. Increasing the efficiency of energy generation methods, improving solar and wind energy generation are some of the prominent countermeasures that are being developed.

A more futuristic take on the energy problem has been the idea of *energy harvesting*. Generally speaking, this concept attempts to take advantage of systems and processes which produce waste energy during their functionalities. The natural temptation is to *harvest* the wasted energy instead of dissipating it. This idea is not new and numerous clever pathways have already been developed as described in Harb (2011). One of the actively studied topics is the harvesting of energy from mechanical vibrations and motion; for instance from automobile suspensions (Gupta et al., 2006; Zuo et al., 2010), from civic structures and buildings (Tang and Zuo, 2012), from ocean waves (Taylor et al., 2001), and even from human motion (Saha et al., 2008). The

power levels in most energy harvesting applications are considerably low and as a result, microsystems and wireless electronics are also becoming increasingly popular scientific explorations (Paradiso and Starner, 2005; Beeby et al., 2006). For more comprehensive reviews on the subject, the reader is directed to work such as Mitcheson et al. (2008), Zuo and Tang (2013).

Systems that harvest energy from vibrations have been proposed in various forms. The main feature that all applications share is the introduction of some transducers that can convert kinetic energy into electrical energy. They act analogous to mechanical dampers, except that they produce electricity instead of waste heat. In some applications they are even used in lieu of conventional shock absorbers (Li et al., 2013). The most commonly used transducers are either of piezoelectric or electromagnetic type (Khaligh et al., 2010; Karami and Inman, 2011, Iliuk et al., 2014). The former is popular in microsystems and small scale applications (Sodano et al., 2005; Litak et al., 2010) because very few or no moving parts are involved. Electromagnetic devices on the other hand, are more suitable in large scale systems (Zuo and Tang, 2013). In both cases, it is also possible to use the transducer as an actuator; a feature which has been utilized in some studies (Nakano et al., 2003).

2.1.2. Premise of the study

This study proposes a new concept to enhance the energy harvesting capacity from mechanical vibrations using a delayed feedback tuning mechanism (Kammer and Olgac, 2016). The idea stems from the Delayed Resonator (DR) and Delayed Feedback Vibration Absorber (DFVA) concepts discussed under Chapter 1. These devices are capable of absorbing vibrations from a primary structure over a range of frequencies while the center frequency of excitation

varies in time. This is achieved by inducing resonance (or near-resonance) in the absorber substructure through the introduction of a delayed feedback force. The main premise is that by inviting resonance, the kinetic energy available for harvesting in this substructure could be significantly increased. This is an interesting proposition which leads to several critical arguments. First of all, the proposed scheme requires a control operation and actuation effort to exert a delayed feedback force. This means that the resulting construct becomes an *active* system which needs a careful assessment for dynamic stability, as discussed earlier under Chapter 1. Secondly, the most natural question is whether the potential increase in harvested energy would be high enough to outweigh the control/actuation energy. Although it appears to be a daring proposition, there are example cases in practice where similar strategies have been implemented with great success. For instance, consider *superchargers* in internal combustion engines. These devices consume a certain percentage of the engine's power. In return, they boost the power production to such levels that the net output is effectively increased (Heywood, 1988). A vital step in this work is then to investigate whether this same principle would hold in a possible DR-harvester combination. In other words, could this construct be more advantageous compared to passive systems where no external energy input is needed? In what follows, we conduct an analytical and numerical analysis of this proposed idea in an attempt to answer these questions. The main results are first derived on a seismic mass resonator setup, where the absorber is subject to steady harmonic movement as the base excitation. The findings are then extended to cases where the absorber is mounted on a primary structure, as in typical tuned-mass damper applications. The developed concepts are then demonstrated on a case study with the critical evaluations of feasibility.

2.2.Energy Harvesting from Seismic Mass Type Resonators

In order to discuss the underlying theory, let us consider a delayed resonator mounted on a moving base, as depicted in Figure 2.1. This configuration is referred to as the "seismic mass type absorber" in the remainder of the text. A delayed acceleration feedback is applied through an actuator for the active tuning of the device. Notice that the lumped damping constant *c* is associated with a *transducer* element, instead of a mechanical viscous damper. This way, the energy which would traditionally be dissipated through heat, is instead converted into electrical energy. For the preliminary analysis, we neglect specifics such as the efficiency of energy transduction, and treat all the dissipated energy as potentially harvestable.

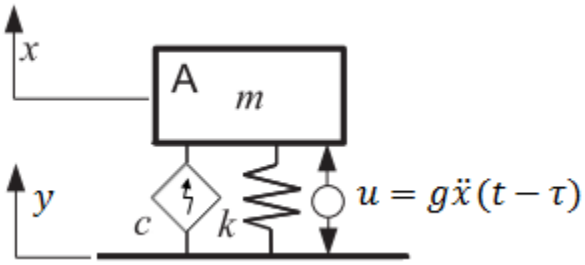

Figure 2.1. Energy harvesting from a seismic mass type setup.

A delayed acceleration feedback is applied through an actuator for the active tuning of the device. Notice that the lumped damping constant *c* is associated with a *transducer* element, instead of a mechanical viscous damper. This way, the energy which would traditionally be dissipated through heat, is instead converted into electrical energy. For the preliminary analysis, we neglect specifics such as the efficiency of energy transduction, and treat all the dissipated energy as potentially harvestable.

The governing equation for the system in Figure 2.1 is

$$m\ddot{x} + c\dot{x} + kx = c\dot{y} + ky + g\ddot{x}(t-\tau). \tag{2.1}$$

Applying Laplace transformation, the transfer function between base motion and the absorber displacement becomes

$$\frac{X(s)}{Y(s)} = H(s) = \frac{cs + k}{ms^2 + cs + k - s^2 g\,\mathrm{e}^{-\tau s}}. \tag{2.2}$$

Here, the denominator is the characteristic equation of this system. For the desired DR operation, the feedback gain g and the delay τ are selected such that the characteristic equation exhibits a pair of roots at $\pm\omega$i. By substituting $s = \omega$i in the characteristic equation, one can solve the necessary control parameters as

$$g = \frac{1}{\omega^2}\sqrt{(c\omega)^2 + (m\omega^2 - k)^2},$$

$$\tau = \frac{1}{\omega}\left[\tan^{-1}\left(\frac{c\omega}{m\omega^2 - k}\right) + 2(l-1)\pi\right], \quad l = 1,2,\ldots. \tag{2.3}$$

Let us first investigate the possibility of harvesting energy from seismic mass type systems (Figure 2.1). The DR-tuned absorber is mounted on a *primary* structure, of which the motion is unaffected by the absorber (also known as impedance mismatch). The absorber is then tuned to resonate at a targeted frequency to completely absorb the corresponding tonal vibration of the primary structure. In this abstraction however, the primary structure is considered to be very large compared to the absorber, and the seismic mass is simply subject to tonal harmonic base excitation. In such a case, the ideal tuning of the resonator is in fact undesirable since the base motion is unaffected from the absorber and remains harmonic. It would theoretically result in infinitely-growing absorber strokes and the system would not reach a steady state solution.

Based on the above discussion, it is apparent that tuning the absorber to DR conditions is infeasible. For this reason, the approach we purse falls under the category of DFVA tuning. That is, the (τ, g) selection should be such that the absorber substructure remains asymptotically stable, yet close to marginal stability so that it is *sensitized* rather than *resonant*. As mention earlier under Chapter 1, DFVA tuning does not impose strict conditions on control parameters (τ, g). On the contrary, any parameter composition in the DR's stable region is available for control synthesis. In order to have a systematically parameterized control law, we propose to tune the gain and delay parameters corresponding to an artificially decreased damping coefficient. The DFVA structure without active control is essentially a mass-spring-damper, which has a set of complex conjugate characteristic roots. For a lightly damped structure, these eigenvalues are very closely positioned to the imaginary axis, requiring less control effort to de-stabilize. Thus if the DFVA is tuned properly, it can be made *near-resonant*. Let us define the following set of control parameters to achieve this objective.

$$g_1 = \frac{1}{\omega^2}\sqrt{(c_1\omega)^2 + (m\omega^2 - k)^2}\,,$$

$$\tau_1 = \frac{1}{\omega}\left[\tan^{-1}\left(\frac{c_1\omega}{m\omega^2 - k}\right) + 2(l-1)\pi\right], \quad l = 1,2,... \tag{2.4}$$

These are identical to the actual (τ, g) compositions rendering marginal stability, with the exception that a *reduced* damping coefficient $c_1 = \alpha c$ is utilized. Here, $0 < \alpha < 1$ is called the *resonance proximity factor* (RPF) which dictates the amount of deviation from DR tuning conditions. A sample case for an RPF value of $\alpha = 0.8$ is depicted in Figure 2.2 (i.e., the damping constant is taken as 80% of the ideal value). It can be shown for such dynamics, that the (artificial) stability curves obtained using the reduced damping (shown in green), always lie

below the original stability curves (blue). Thus the new control law with $\alpha < 1$ always renders a stable operation of the DFVA.

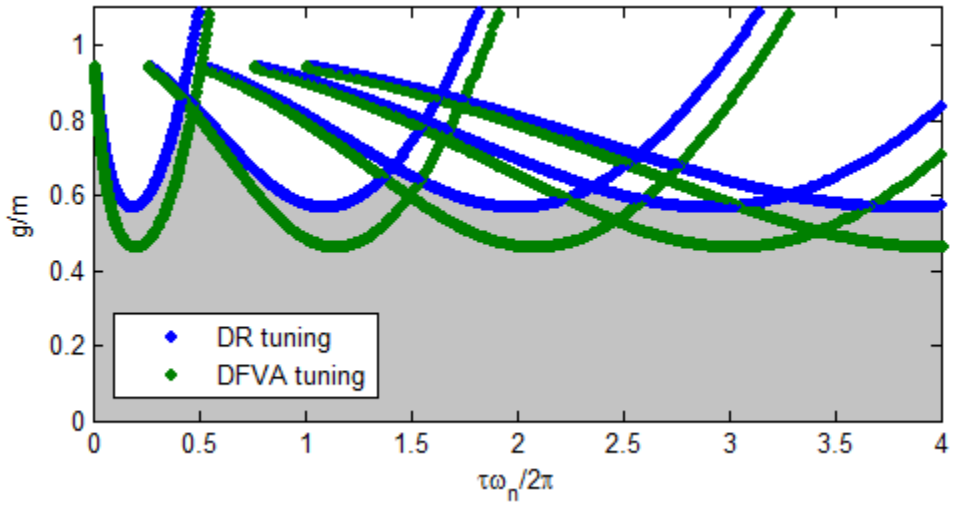

Figure 2.2. Normalized gain vs. delay parameters for DR and DFVA (near-resonant) tuning with RPF $\alpha = 0.8$ ($m = 1$ kg, $c = 18$ Ns/m, $k = 900$ N/m). Stable region shaded.

2.3.Energy Balance of DFVA Harvester

The most critical feature of the setup shown in Figure 2.1 is that the active control action consumes energy. Thus one needs to assess the energy inventory of the proposed scheme very carefully. This procedure is performed next, by evaluating the flow of energy in and out of the system. The analysis here follows a parallel approach to the work by Stephen (2006), except that we also take active tuning into account, in addition to the passive systems.

Let us start with a pure harmonic base motion of frequency ω.

$$y = y(t) = \bar{Y}\sin(\omega t) \tag{2.5}$$

The frequency response of the absorber mass would also be harmonic, with a different amplitude and phase.

$$x = x(t) = \overline{X}\sin(\omega t + \phi) \tag{2.6}$$

The amplitude and phase relations are obtained from the transfer function $H(s)$ given in (2.2).

$$\overline{X} = \overline{X}(\omega) = \left|H(\omega \mathrm{i})\right|\overline{Y}, \quad \phi = \phi(\omega) = \angle H(\omega \mathrm{i}) \tag{2.7}$$

Let us define the relative motion between the mass and base displacements as $z = x - y$. Using the Laplace domain relations in (2.2), we obtain

$$Z(s) = X(s) - Y(s) = G(s)Y(s), \quad G(s) = \left[H(s) - 1\right]. \tag{2.8}$$

Then for $z = z(t) = \overline{Z}\sin(\omega t + \psi)$, the steady state amplitude and phase are calculated similarly to (2.7).

$$\overline{Z} = \overline{Z}(\omega) = \left|G(\omega \mathrm{i})\right|\overline{Y}, \quad \psi = \psi(\omega) = \angle G(\omega \mathrm{i}) \tag{2.9}$$

Power produced by the transducer: The instantaneous power generated by the transducer element (assuming it is all harvestable) is

$$P_{gen} = c\dot{z}^2 = c\omega^2 \overline{Z}^2 \cos^2(\omega t + \psi) \tag{2.10}$$

and the corresponding energy generated per cycle is

$$E_{gen}^{T} = c\omega^2 \overline{Z}^2 \int_0^T \cos^2(\omega t + \psi)dt = c\omega \overline{Z}^2 \pi \tag{2.11}$$

where $T = 2\pi / \omega$ denotes the period of oscillation. The average power generated over one period is

$$P_{gen}^{av} = \frac{E_{gen}^{T}}{T} = \frac{c\omega^2 \overline{Z}^2}{2}. \tag{2.12}$$

Power required for the active control action: The instantaneous power consumed by the force actuator is

$$P_{act} = u\dot{z} = g\ddot{x}(t-\tau)\dot{z}(t)$$

$$= -g\omega^3 \overline{X} \sin(\omega t + \phi - \omega\tau)\overline{Z}\cos(\omega t + \psi). \tag{2.13}$$

The corresponding energy consumed per cycle is

$$E_{act}^{T} = -g\omega^3 \overline{X}\,\overline{Z}\int_0^T \sin(\omega t + \phi - \omega\tau)\cos(\omega t + \psi)dt$$

$$= g\omega^2 \overline{X}\,\overline{Z}\pi \sin(\omega\tau + \psi - \phi) \tag{2.14}$$

and the average power consumption per period is

$$P_{act}^{av} = \frac{E_{act}^{T}}{T} = \frac{g\omega^3 \overline{X}\,\overline{Z}\sin(\omega\tau + \psi - \phi)}{2}. \tag{2.15}$$

It is worth noting that, the average power generation as defined in (2.12) depends on the frequency and vibration amplitudes. In the power consumption of the actuator as seen in (2.15) however, the phase difference also plays an important role. The *harvested* (or *net*) average power can now be defined as the difference of generated and consumed average powers as follows.

$$P_{harv}^{av} = P_{gen}^{av} - P_{act}^{av} = \frac{\omega^2 \overline{Z}}{2}\left[c\overline{Z} - g\omega\overline{X}\sin(\omega\tau + \psi - \phi)\right] \tag{2.16}$$

Figure 2.3 depicts the variation of the average power quantities with respect to normalized base excitation frequency for a sample setup. It is observed that potentially harvested energy increases monotonically as frequency increases.

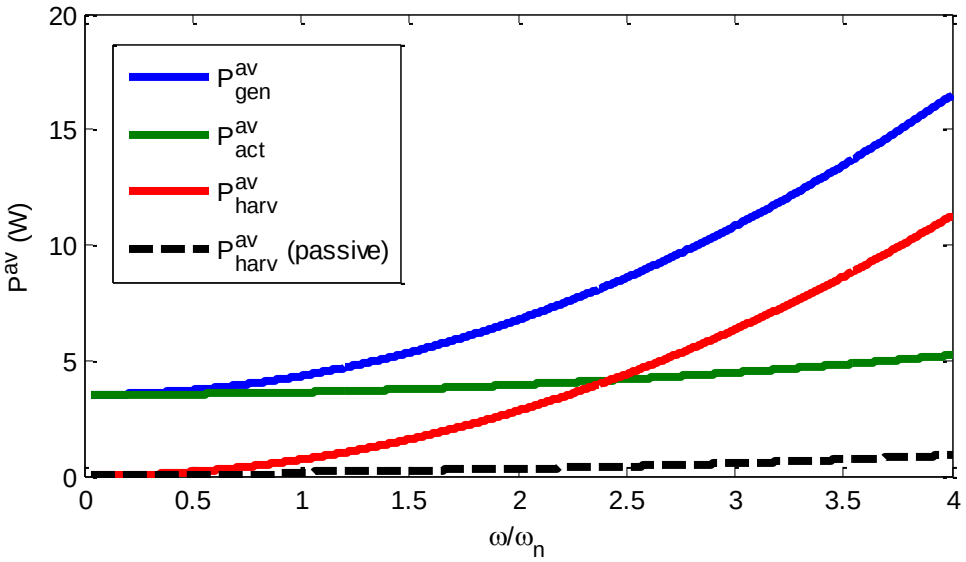

Figure 2.3. P^{av} quantities vs. frequency for DFVA harvester and comparison with passive case.

m = 1 kg, c = 18 Ns/m, k = 900 N/m, RPF α = 0.8, $\overline{Y} = 2.5$ mm.

In order to assess the feasibility of an active DFVA-harvester setup, a comparison with a passive harvester is also presented on Figure 2.3. For the passive case we simply set $g = 0$ in (2.2) and repeat the calculations to obtain P_{gen}^{av}. Average power harvested per cycle is then equal to the generated power, as no energy consuming element exists. As seen in Figure 2.3, the increase in energy harvesting capacity is substantial with the DFVA scheme, especially at higher operating frequencies.

The effects of some parameters on system performance are investigated next. Figure 2.4 depicts the variations of P_{harv}^{av} and $\overline{Z}/\overline{Y}$ (both in base-10 logarithm) with respect to excitation frequency (ω) and the RPF (α). A significant increase of harvestable energy is observed for large α values. On the other hand, it should be noted that high α also results in an exaggerated relative motion, $\overline{Z}/\overline{Y}$. These characteristics are expected, because the system approaches DR tuning conditions as $\alpha \to 1$. As mentioned earlier, imposing pure resonance at the excitation frequency is not desirable in practical systems. Theoretically, it results in unbounded growth of absorber displacement, which is not tolerable. This fact is also apparent in Figure 2.4, where a rapid increase in vibration amplitude is observed as the RPF approaches 1. From this perspective, α must be chosen as high as possible, but still below a certain limiting value so that the energy harvesting capacity could be maximized while the relative motion amplitude is kept below a certain level.

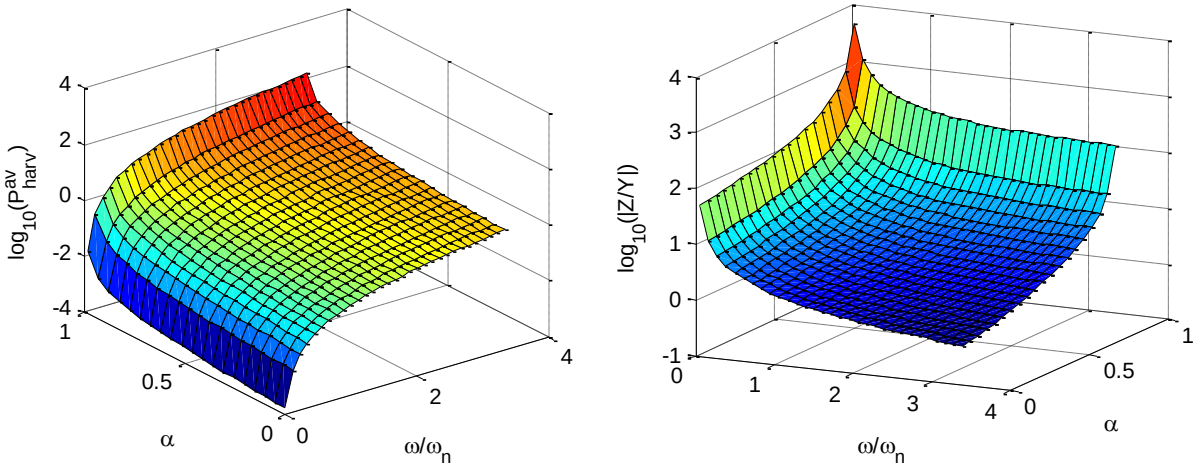

Figure 2.4. Variation of $\log_{10}(P_{harv}^{av})$ and $\log_{10}(\overline{Z}/\overline{Y})$ with respect to RPF (α) and frequency.

m = 1 kg, c = 18 Ns/m, k = 900 N/m, $\overline{Y} = 2.5$ mm.

The preceding analysis is repeated to investigate the effect of damping as well. The variations of P_{harv}^{av} and $\overline{Z}/\overline{Y}$ (again in base-10 logarithm) with respect to excitation frequency (ω) and the damping ratio (ζ) are shown in Figure 2.5. A noticeable feature of these plots is that they are highly similar to those in Figure 2.4. In fact, comparing the two, it is apparent that the RPF and damping ratio influence the system in opposite manner. That is, increasing α yields identical effects as reducing ζ, and vice versa. This feature can again be attributed to the absorber exhibiting pure resonance. However this time it is not imposed by the delayed feedback control; but it is a result of the structure's own lack of damping (i.e., $\zeta = 0$).

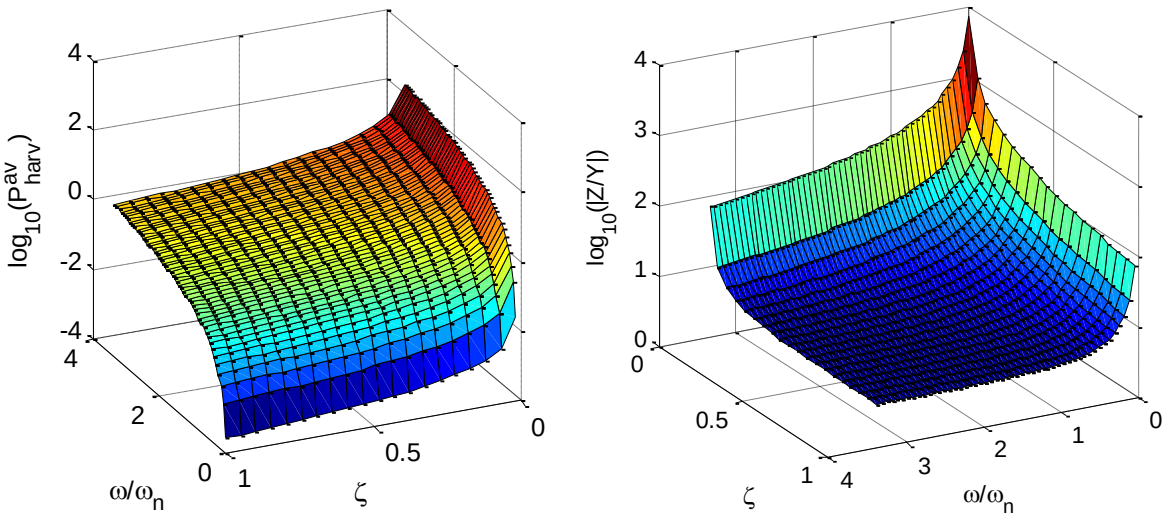

Figure 2.5. Variation of $\log_{10}(P_{harv}^{av})$ and $\log_{10}(\overline{Z}/\overline{Y})$ with respect to damping ratio and frequency. m = 1 kg, k = 900 N/m, RPF α = 0.8, $\overline{Y} = 2.5$ mm.

Remark. *Effect of branch number*

Notice how in Figure 2.2, the DFVA tuning parameters (τ_1, g_1) are calculated on different branches l = 1, 2, … due to the periodicity of the delay-induced term $e^{-\tau\omega i}$. As seen in (2.4), for a given frequency ω, the branch number essentially changes the value of the feedback delay by

$2\pi / \omega$ increments, while the gain remains invariant. The question here is how these periodically distributed delay parameters influence the performance. It should be noted that $\overline{X}$ and ϕ remain invariant for all $\tau = \tau + 2\pi l / \omega$, $l = 1, 2, \ldots$ with $s = \omega$i, as seen from (2.7) and (2.2). Then it directly follows from (2.8) and (2.9) that $\overline{Z}$ and ψ remain invariant also. Finally noting the periodicity of $\sin(\tau\omega + \psi - \phi)$ for all $\tau = \tau + 2\pi l / \omega$, $l = 1, 2, \ldots$ in (2.16), it can be concluded that P_{harv}^{av} essentially remains unchanged among the different branches of the (τ_1, g_1) compositions.

Let us now take a closer look at the relation between the control delay, gain and tuning frequency. Figure 2.6 depicts normalized (τ_1, g_1) and (τ_1, ω) plots corresponding to near-resonant DFVA tuning with a RPF of $\alpha = 0.8$. Two important observations are noted here.

1- The marginally stable operating frequency interval (marked with $\Delta\omega_1$, $\Delta\omega_2$, …) continuously narrows as the branch number increases. Notice that, theoretically there is no upper bound for frequency on the first branch. However in practical applications, the highest possible operating frequency would be bounded due to physical limitations associated with the control sampling period and the actuator bandwidth characteristics.

2- The lower bound of $\Delta\omega_1$, $\Delta\omega_2$, … (possible tuning frequencies) increases on higher branch numbers. That is, $\omega_{min1} < \omega_{min2} < \ldots < \omega_{minl}$ while the upper bounds decrease.

As a result it becomes apparent that the first branch offers the largest operable frequency interval and thus should be preferred over the others. The transient characteristics of the system also vary among branches, which will be demonstrated in more detail over a case study later on.

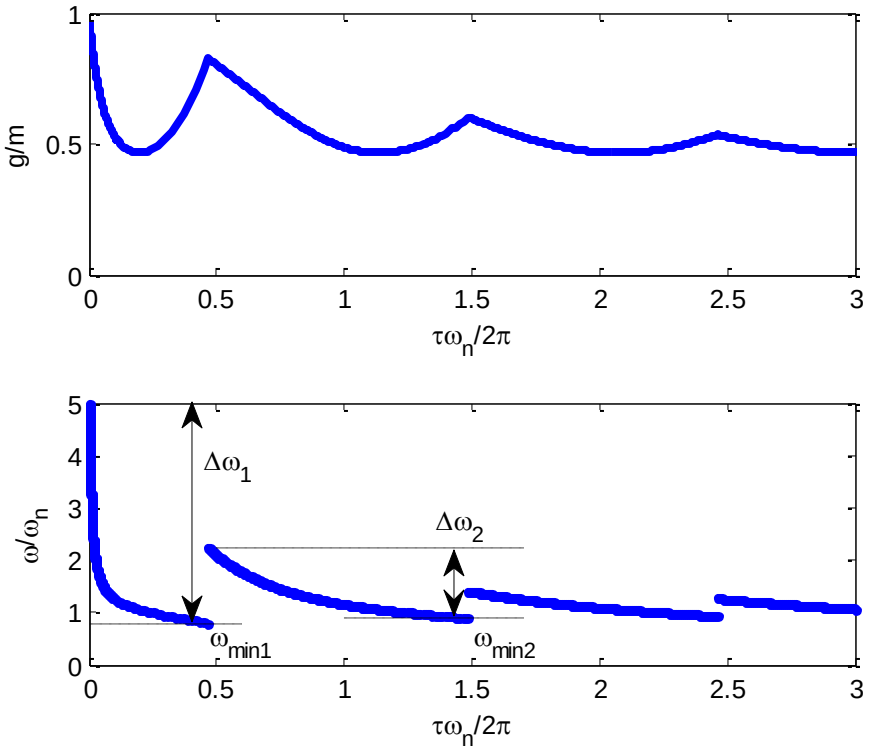

Figure 2.6. Normalized gain and frequency vs. normalized delay for DFVA tuning with RPF α = 0.8. Absorber parameters: m = 1 kg, c = 18 Ns/m, k = 900 N/m.

2.4.DFVA Harvester with a Compliant Primary Structure Coupling

The results up to this point are on the absorber structure alone, where the vibration input is induced through a harmonic base motion. This operation mainly serves as an abstraction for seismic mass type energy harvesters. These are generally micro-scale systems where the main source of excitation is human motion or household devices (Beeby et al., 2006; Mitcheson et al., 2008). Recently, another popular venue for energy harvesting research has been attracting attention: vibration control devices, such as tuned-mass dampers (TMD). TMDs are commonly used, especially in large-scale systems such as buildings and power transmission lines (Inman, 2014), to protect the primary structure from detrimental effects of excessive vibration.

Traditionally, these devices absorb and dissipate energy through some damping elements. Such applications present valuable opportunities for energy harvesting and have been widely studied to date (Tang and Zuo, 2012). Vibration absorption from primary structures is also the main motivation behind the initial development of DRs and DFVAs.

Let us consider the configuration where a DFVA is mounted on a primary structure, as illustrated in Figure 2.7. When tuned according to (1.3), this device operates as a DR and absorbs all vibration occurring at a particular frequency. Under ideal operating conditions, the vibration of the primary structure can be eliminated completely. We note that this principle holds independently from the source of vibration (e.g., base excitation to primary structure, or direct forcing on primary mass with fixed ground).

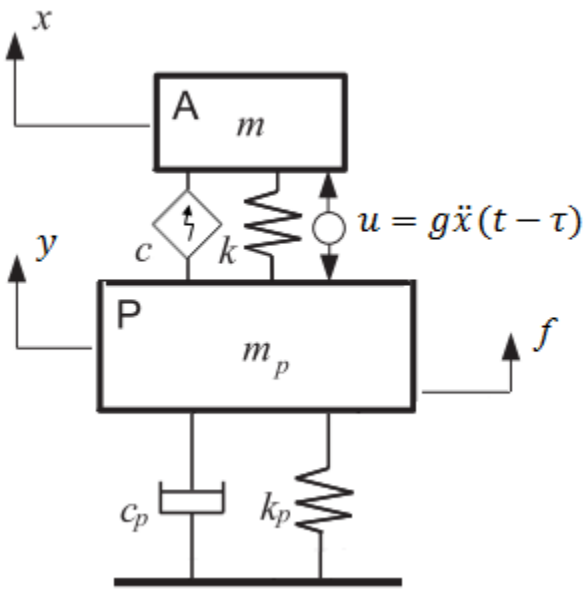

Figure 2.7. DFVA-harvester coupled to a primary structure.

Differently from the previous analysis, increasing energy harvesting capacity is not the sole objective here. The absorber should also serve its main purpose by ensuring that vibration in

the primary structure is abated. Intuitively, one may assume that tuning to DR conditions may be beneficial for energy harvesting as well. Complete sensitization (and the ensuing resonance) in the absorber substructure implies high-amplitude oscillations, which might sound desirable for energy harvesting. In the following analysis we investigate the energy balance in this construct, and show that this is, in fact, not the case.

The equation of motion for the absorber is identical to the previous case as in (2.1), with the exception that *y* now represents the displacement of the primary mass.

$$m\ddot{x} + c\dot{x} + kx = c\dot{y} + ky + u \tag{2.17}$$

Multiplying this equation by $\dot{x}$ and applying some algebraic manipulations, one obtains

$$m\ddot{x}\dot{x} + k(x-y)(\dot{x}-\dot{y}) + c(\dot{x}-\dot{y})^2 - u(\dot{x}-\dot{y}) = u\dot{y} + c(\dot{y}-\dot{x})\dot{y} + k(y-x)\dot{y} \tag{2.18}$$

which can be rewritten as

$$\frac{d}{dt}\left[\frac{m\dot{x}^2}{2} + \frac{k(x-y)^2}{2}\right] + c(\dot{x}-\dot{y})^2 - u(\dot{x}-\dot{y}) = u\dot{y} + c(\dot{y}-\dot{x})\dot{y} + k(y-x)\dot{y}\,. \tag{2.19}$$

This equation serves one purpose: it shows a complete representation of the energy balance in the absorber substructure. The right-hand side denotes the instantaneous power contributed by the motion of the primary mass (i.e., $\dot{y}$ multiplying all forces it works against). The left-hand side consists of the time rate of change of kinetic and potential energies, in addition to the instantaneous power generated by the transducer element and the power consumption of the actuator.

If the absorber is tuned to resonate using the DR parameters as in (1.3), the primary mass completely ceases to move under the tonal excitation *f*. That is, $y = \dot{y} = 0$ while the steady state absorber behavior becomes harmonic at the frequency of the excitation $x = \overline{X}\sin(\omega t + \phi)$. With these, (2.19) reduces to

$$\frac{d}{dt}\left[\frac{m\dot{x}^2}{2} + \frac{kx^2}{2}\right] + c\dot{x}^2 - u\dot{x} = 0\,. \tag{2.20}$$

Integrating this expression over the period of oscillation, the energy exchange during a cycle is

$$\left(\frac{m\dot{x}^2}{2} + \frac{kx^2}{2}\right)\Bigg|_0^{T=2\pi/\omega} + \int_0^{T=2\pi/\omega} c\dot{x}^2 dt - \int_0^{T=2\pi/\omega} u\dot{x} dt = 0\,. \tag{2.21}$$

Since *x* is a pure harmonic function, $\left(m\dot{x}^2 + kx^2\right)/2\Big|_0^{T=2\pi/\omega} = 0$, leaving the two terms as

$$\int_0^{T=2\pi/\omega} c\dot{x}^2 dt = \int_0^{T=2\pi/\omega} u\dot{x} dt\,. \tag{2.22}$$

In other words, all energy generated through the transducer element (left side) equals exactly the energy consumed by the actuator which exerts the tuning force (right side term). As a result, no net energy will be gained. Therefore the tuning to an ideal resonator (i.e., DR) is not a feasible pathway from energy harvesting perspective.

From the preceding analysis we conclude that the DR tuning scheme is infeasible for energy harvesting, echoing the findings for the seismic harvester case. Following similar arguments, the DFVA approach is pursued instead. A significant difference however, is that displacement of the primary mass *y* is not a fixed base excitation for this case. In fact, the steady-state amplitude of *y* strongly depends on the DFVA characteristics.

The equation of motion for the primary structure is

$$m_p\ddot{y} + (c_p + c)\dot{y} + (k_p + k)y = c\dot{x} + kx - g\ddot{x}(t-\tau) + f\ . \tag{2.23}$$

Here, f represents an external force that directly acts on the primary structure. Laplace transformation of (2.23) is

$$[m_p s^2 + (c_p + c)s + (k_p + k)]Y(s) = (cs + k - s^2 g\,\mathrm{e}^{-\tau s})X(s) + F(s)\,. \tag{2.24}$$

Using the primary-to-absorber transfer function (2.2) in the above equation, the transfer function between the f and y is then obtained as follows.

$$\frac{Y(s)}{F(s)} = \frac{ms^2 + cs + k - s^2 g\,\mathrm{e}^{-\tau s}}{[m_p s^2 + (c_p + c)s + (k_p + k)](ms^2 + cs + k - s^2 g\,\mathrm{e}^{-\tau s}) - (cs + k - s^2 g\,\mathrm{e}^{-\tau s})(cs + k)} \tag{2.25}$$

If we consider harmonic excitation for f, with a frequency ω, the control parameters (τ_1, g_1) rendering near-resonant conditions are calculated via (2.4). This implies a RPF close to 1. Substituting these control parameters $\tau = \tau_1$, $g = g_1$ along with $s = \omega\mathrm{i}$ in (2.25), $\overline{Y} = |Y(\omega)|$ is obtained at the steady state for a given force $f = F_0\sin(\omega t)$. With $\overline{Y}$ known as a function of ω, the energy harvesting performance for this configuration can then be assessed using the expressions derived under the previous subsection.

An important issue associated with the DFVA and primary structure coupling is the dynamic stability of the combined system, as discussed previously under Chapter 1. The (τ_1, g_1) composition obtained via (2.4) must not render instability for the coupled dynamics with the compliant primary structure. The combined system's characteristic equation, as seen in (2.25) can be expressed as

$$A(s) + B(s) g\, \mathrm{e}^{-\tau s} = 0\,, \text{ where}$$

$$A(s) = [m_p s^2 + (c_p + c)s + (k_p + k)](ms^2 + cs + k) - (cs + k)^2\,,$$

$$B(s) = -s^2(m_p s^2 + c_p s + k_p) \tag{2.26}$$

in conjunction with the notation defined in (1.4) under Section 1.3. Then the expressions (1.5) can be used to calculate the combined system's stability boundaries.

2.5.Numerical Case Study

For a numerical case study, we consider the setup as seen in Figure 2.7. A DFVA energy harvester is mounted on a primary mass which is under the influence of a harmonic forcing, $f = F_0 \sin(\omega t)$ with $F_0 = 1$ kN. The primary system's parameters are taken as $m_p = 10$ kg, $k_p = 3000$ N/m, $c_p = 500$ Ns/m. The absorber's structural parameters are $m = 1$ kg, $k = 900$ N/m, $c = 18$ Ns/m. As the control law, we apply a near-resonant tuning scheme, with a RPF of $\alpha = 0.8$. The control parameters used for the DFVA tuning, (τ_1, g_1), are calculated directly from (2.4). Notice that in this case, the DR tuning scheme as defined in (1.3) represent the loci of control parameters that yield complete vibration suppression but no energy harvesting capacity. The stability of the combined system, on the other hand, is declared by the characteristic equation in (2.26) and the stability boundaries (τ_{cs}, g_{cs}) are calculated using (1.5). Figure 2.8 displays all relevant parameter loci in the (τ, g) space. The DFVA tuning parameters are shown in green, while the DR tuning parameters are depicted in blue. The combined system's stability boundaries are shown in red. Notice that the DFVA curves (green) are always positioned below the DR curves (blue). This is expected because the DFVA parameters (τ_1, g_1) as defined in (2.4) are

essentially a perturbation from the DR parameters. This feature was also highlighted earlier in Section 2.3 (see Figure 2.2).

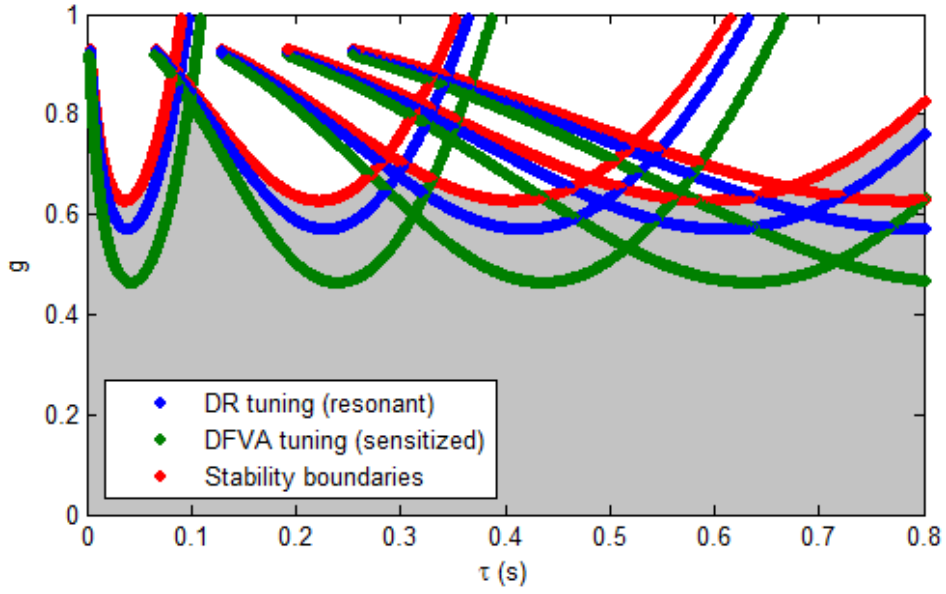

Figure 2.8. Gain vs. delay parameters for: DR tuning (blue), DFVA tuning with RPF α = 0.8 (green) and the combined system's stability (red). Stable region shaded.

A more critical observation from Figure 2.8 is that the DFVA parameters (green) do not violate the combined system's stability limits (red). This fact cannot be taken as granted in general, because the coupled system dynamics is significantly different than that of the absorber alone [see respective characteristic equations (2.26), and the denominator of (2.2)]. For more involved settings, the CTCR paradigm (Olgac and Sipahi, 2002; Sipahi and Olgac, 2006) can be utilized to assess the delay-dependent stability outlook (as in Figure 2.8).

Recalling the earlier discussions on branch numbers, we now focus on the first two branches for further analysis. Figure 2.9 depicts the (τ_1, g_1) loci contributed by l = 1 and 2 (a); with additional plots for (τ_1, ω) (b) and (τ_1, P_{harv}^{av}) variations (c).

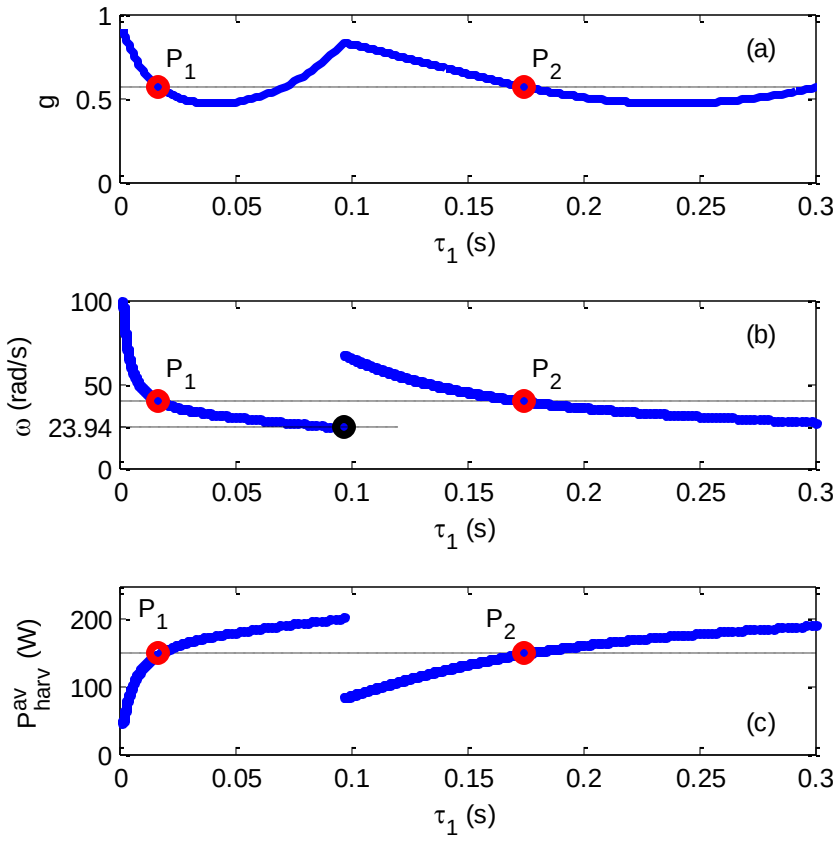

Figure 2.9. DFVA tuning parameters (τ_1, g_1) (a), corresponding (τ_1, ω) (b) and (τ_1, P_{harv}^{av}) (c) plots. ω_{min} marked with black circle in (b). Simulation test points P_1, P_2 marked with red circles.

This layout offers a good understanding of how frequency and energy harvesting performance vary along the DFVA tuning scheme. The lowest possible frequency at which the DFVA can operate is determined to be ω_{min} = 23.94 rad/s on the first branch (marked on Figure 2.9 panel b). When compared to the seismic mass case, we observe a different relation between frequency and harvested energy here. For the former, Figure 2.3 clearly displays that average harvested power, P_{harv}^{av}, increases monotonically as the frequency of base excitation increases. In this case however, a reversed relation between ω and P_{harv}^{av} is observed, as seen in panels (b) and

(c) of Figure 2.9. That is, the smaller the excitation frequency, the higher the average harvestable power. The logical explanation behind this observation is that increasing ω invites higher level of tuning energy compared to the increase in the generated (dissipated) energy. This reversal of energy inventory arises due to the complicated characteristics of the added primary structure, in contrast to the seismic mass case.

As mentioned earlier, in the case of a primary structure, the DFVA energy harvester also needs to function as a TMD. The residual steady state vibration of the primary structure is a point of concern and should be analyzed along with energy harvesting performance. Figure 2.10 displays the frequency response of the primary mass as calculated from (2.25), along with the variation of P_{harv}^{av} with respect to operating frequency (blue lines). The performance of a passive harvester is also depicted on the same figure (green lines), as a benchmark. The passive case is again simulated by substituting $g = 0$ in the governing equations. By doing so the active control element is eliminated and the absorber becomes akin to a conventional TMD. Compared to the passive system, the DFVA scheme offers improved vibration suppression (i.e., overall lower frequency response as seen in Figure 2.10 panel a). The improvement in energy harvesting capacity is even more significant (see Figure 2.10 panel b). Being a single degree-of-freedom damped system, the passive system yields peak performance in the vicinity of its resonant frequency. The DFVA harvester on the other hand, provides considerably higher energy harvesting capacity, and does so in a much wider frequency range. The only limitation of the DFVA harvester is the lower bound on operating frequency, ω_{min} due to system stability. This bound is marked on Figure 2.10 with a vertical dashed line. On the other hand, looking at panel b, we note that the passive harvester does not provide a significant amount of energy for $\omega < \omega_{min}$ either.

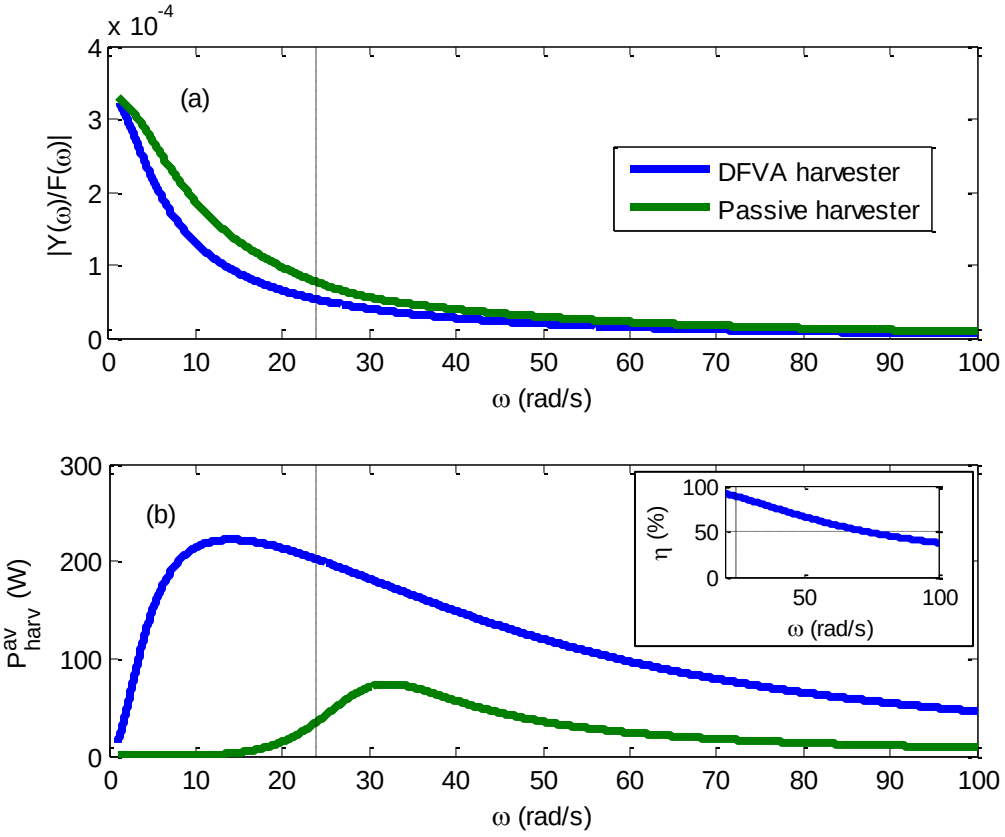

Figure 2.10. Comparison of primary mass frequency responses (a) and energy harvesting performances (b) for DFVA and passive harvesters. ω_{min} marked with vertical dashed line. Feasible efficiency limit for energy harvesting shown in inset.

We consider an exemption to the energy conversion efficiency only in this section. The text up to now assumed that 100% of P_{gen}^{av} is converted to useful energy. In real applications, however, this cannot hold. There is always a loss in the conversion process, and every transducer has a conversion efficiency, say $\mu < 100\%$. Then the quantity defined as the *efficiency limit*, $\eta = P_{act}^{av} / P_{act}^{av}$ [see (2.15) and (2.12), respectively] has to be smaller than μ for the energy harvesting operation to be feasible. In other words, the chosen energy conversion mechanism has to yield better efficiency than this limit ($\mu > \eta$). The variation of η with respect to frequency is

displayed in Figure 2.10 panel b as an inset. We conclude that the permissible efficiency interval widens as frequency increases. At lower frequencies the system requires almost $\mu = 100\%$ conversion efficiency for a feasible operation, while this value drops below 50% at higher frequencies.

The results shown in Figure 2.10 are generated for the sample system with a certain absorber damping ratio ($\zeta = 0.3$) and a fixed RPF of $\alpha = 0.8$. In order to understand how these parameters affect the energy harvesting and vibration suppression performance, a similar analysis as in Section 2.3 is considered. Surface plots for average harvested energy and primary mass vibration amplitude are presented in Figure 2.11. The influence of the RPF is emphasized, while the effect of damping is also shown in insets. It is observed that α and ζ affect the performance in an opposite manner, echoing the results of the seismic harvester case (see Figure 2.4 and Figure 2.5). Some interesting characteristics are revealed here. As the RPF is increased, energy harvesting performance climbs until reaching a peak and sharply drops afterwards. The steep decrease occurs as the RPF approaches to $\alpha = 1$. This is an expected outcome because $\alpha = 1$ corresponds to DR tuning conditions, which were shown to eliminate energy harvesting capacity under Section 2.4. Regarding the primary mass vibration amplitude, it decreases at a slow rate until $\alpha \approx 0.9$ and sharply drops as $\alpha \to 1$. The sudden reduction can also be attributed to DR tuning, which completely eliminates primary mass vibration under ideal circumstances. In contrast, for vibration control purposes, the relation is more straightforward. Increasing RPF yields monotonically decreasing primary mass vibration amplitude. From these two plots we conclude that an *optimal* RPF value can be designated, where energy harvesting capacity exhibits a peak.

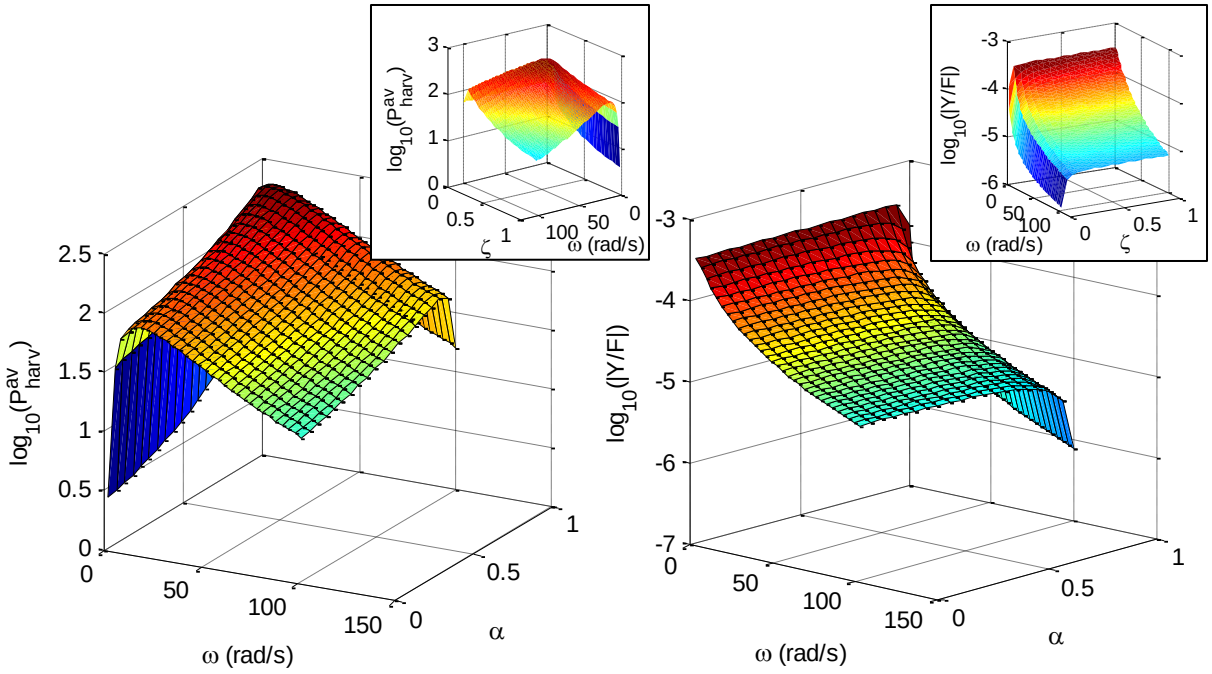

Figure 2.11. Variation of $\log_{10}(P_{harv}^{av})$ and $\log_{10}(\overline{Y}/F_0)$ with respect to RPF (α) and frequency (with $\zeta = 0.3$). Effect of damping shown in inset plots (for $\alpha = 0.8$). m = 1 kg, c = 18 Ns/m, k = 900 N/m, $\overline{Y} = 2.5$ mm.

Let us now take a closer look at the effect of branch number as discussed earlier in the article. For a frequency $\omega = 40$ rad/s, test points P_1, P_2 (corresponding to $l = 1$ and 2, respectively) are marked on Figure 2.9. As these two points share the same frequency, the corresponding gain and P_{harv}^{av} values are also identical. Regarding energy harvesting performance, we note that it depends on steady-state amplitude and phase characteristics of the system; which were shown earlier to remain invariant with respect to branch number l. However the same cannot be said for transient characteristics. Figure 2.12 depicts the characteristic root distribution for the combined dynamics, and time-response of the primary mass. Because the characteristic equation (2.26) is transcendental, the roots cannot be solved analytically. Thus they are numerically calculated within a certain tolerance using a routine called QPmR (Vyhlídal and

Zítek, 2009). Here we observe that, as branch number increases from 1 to 2, the dominant root of the characteristic equation moves considerably closer to the imaginary axis. As a result, it is expected that transient features such as settling time and disturbance rejection capabilities deteriorate. This is corroborated by the time domain simulations. For $l = 1$, the settling time is seen to be $t_s \approx 0.7$ s; while for $l = 2$, it is $t_s \approx 1.9$ s (marked with vertical lines on Figure 2.12). This feature clearly demonstrates that the 1st branch offers optimal performance and should be the first choice while tuning the DFVA.

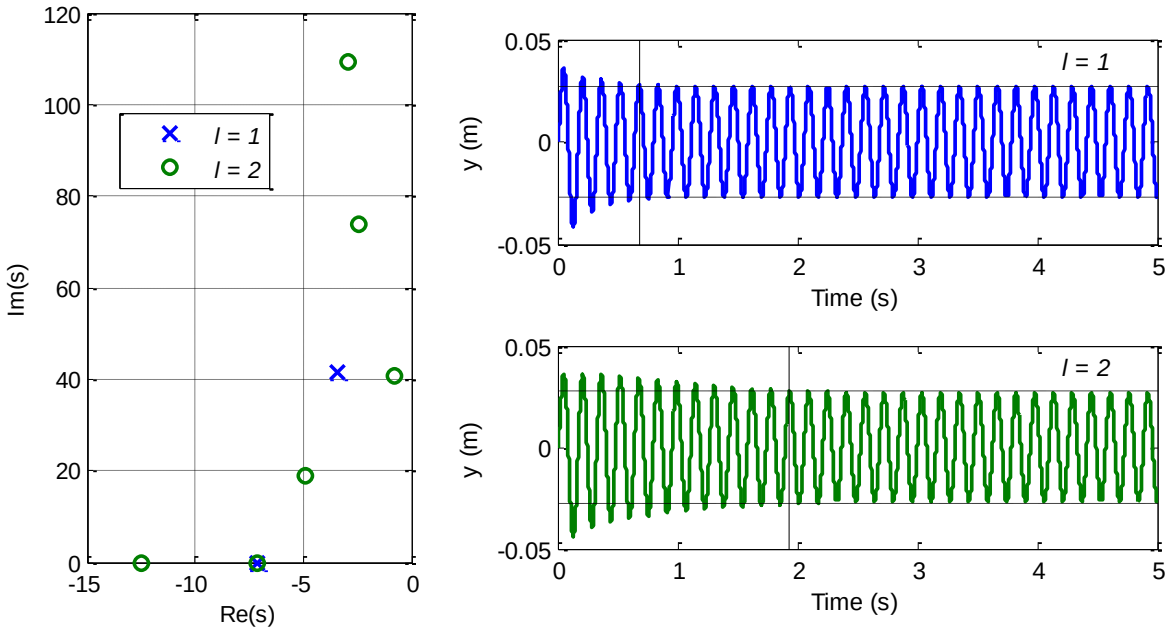

Figure 2.12. Characteristic root distribution and time response of primary mass for different branch numbers ($l = 1$ and 2). Steady state amplitudes and settling times marked by horizontal (dashed) and vertical lines, respectively.

2.6.Summary

The utilization of Delayed Feedback Vibration Absorber concept to enhance energy harvesting capacity is proposed in this chapter. The main results are derived on a stand-alone resonator structure installed on a moving base. This serves as an abstraction for seismic mass type energy harvesters. For this case it is observed that energy harvesting capacity increases monotonically with respect to excitation frequency. These results are further extended to the case where the absorber is attached to a compliant primary structure. In both cases it is revealed that conventional DR tuning (which induces resonance in the absorber) does not allow net harvestable energy. A near-resonant tuning scheme on a DFVA is devised such that the absorber is made sensitive but not completely resonant at target frequencies. Net harvestable energy and the energy required to sensitize the absorber are analyzed. It is demonstrated that the new strategy offers a substantial increase in energy harvesting capacity compared to passive harvesters.

In the case where the harvester is attached to a compliant primary structure, the stability of the system and its frequency response characteristics are also investigated. Differently from the seismic mass harvester, the vibration control aspect becomes a concern. For this purpose, the variation in the primary structure's vibration amplitude is studied. A case study is presented to analyze these features in greater depth and to demonstrate some further details. In the feasible operating frequency range, average power harvested per cycle is found to decrease monotonically as frequency increases. This trend is the opposite for what was observed in the seismic harvester case (see Figure 2.3). It is attributed to the decrease in the primary structure's response amplitude at higher frequencies (see Figure 2.10 panel a).

Another feature, “the branch number”, is also investigated. This property arises due to the periodicity of the delay-induced exponential terms in the characteristic equation. The effect of branch numbers on energy harvesting yields some interesting findings. It is shown that steady state response is invariant among all the branches, while the transient performance is significantly affected. On higher branches, the dominant characteristic roots migrate closer to the imaginary axis. As a result, settling time and disturbance rejection capabilities deteriorate as branch number increases. This effect is verified in the simulation results (see Figure 2.12).

It should be noted that the present work is a concept study, which declares a viable sensitization method within the absorber in order to increase the harvestable energy. It is assumed that all energy outflow through the dissipative element (i.e., lumped damping) is potentially harvestable. In practical systems, however, the damping elements consist of two main components: equivalent viscous damping and parasitic effects within the energy extraction mechanisms. Through investigations on the equivalent damping and the efficiency associated with energy conversion, more realistic assessments for energy harvesting performance could be achieved.

Chapter 3. Vibration Control and Energy Harvesting using Delayed Feedback in Piezoelectric Networks

3.1.Review on Vibration Control using Piezoelectricity

Piezoelectric materials started emerging for vibration control purposes in the 80s (Forward, 1979; Bailey and Ubbard, 1985; Crawley and DeLuis, 1987). Piezoelectric materials exhibit a unique characteristic by developing stress/strain in response to an applied electrical field. Similarly, if the material is subjected to mechanical stress/strain, an electrical field is generated across its electrodes. The most commonly used type are lead-zirconate-titanate (PZT) ceramics. The inherent electro-mechanical coupling becomes attractive for engineering purposes, such as sensing, actuation and control. Hagood and von Flotow (1991) introduces the concept of utilizing passive shunt circuits for structural vibration damping. The piezoelectric element acts as a capacitor (see Figure 3.1), and when connected to a resistor (R) and inductor (L) in series, it can be used to form a damped resonant circuit.

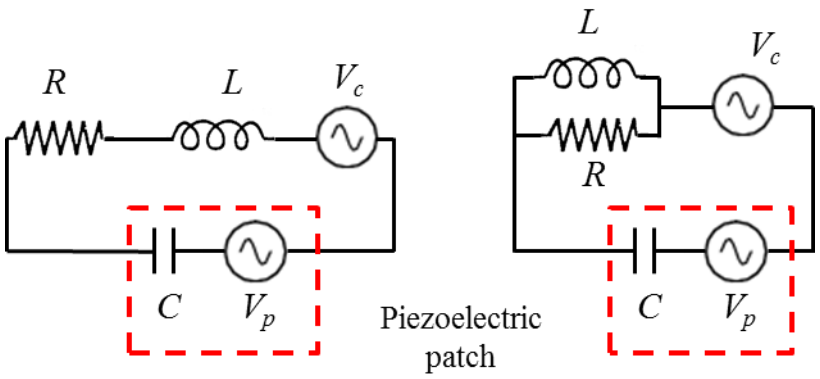

Figure 3.1. Series (left) and parallel (right) piezoelectric network configurations. C: piezoelectric element capacitance, L: inductance, R: resistance, V_c: control voltage, V_p: piezoelectric voltage

As a result of the electro-mechanical coupling introduced by the piezoelectric element, the differential equations for the electrical circuit and the mechanical host structure become coupled. This produces a dynamics analogous to adding a mechanical vibration absorber as illustrated in Figure 3.2. By adjusting the *R-L* parameters according to certain criteria, considerable vibration suppression can be achieved.

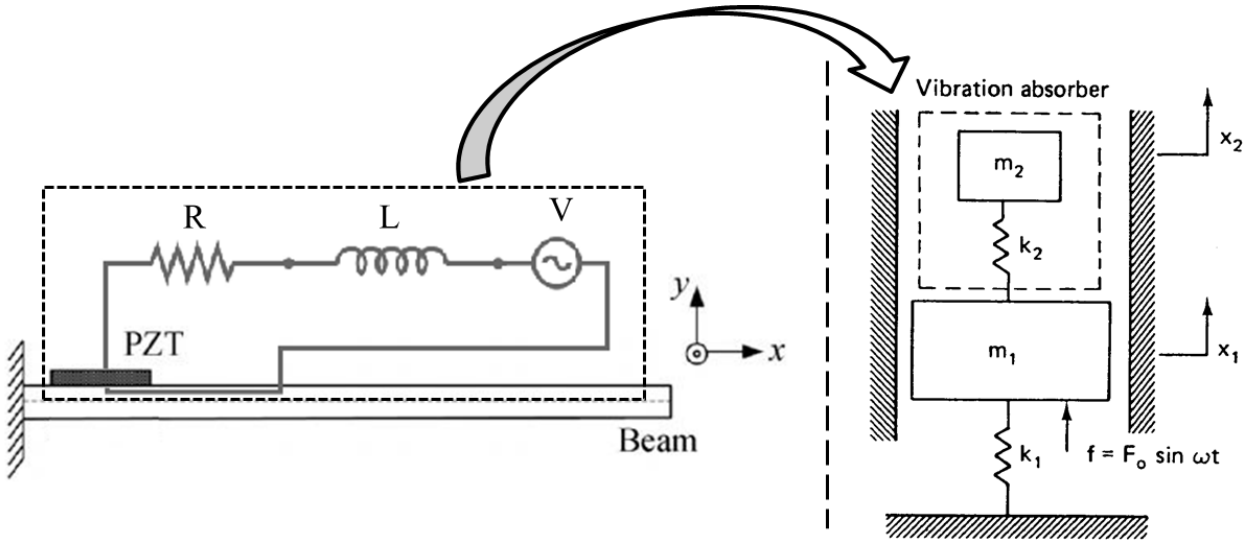

Figure 3.2. Vibration absorber effect of shunt circuit in a piezoelectric network.

In further research, alternative circuit configurations were investigated. For instance, Wu (1996) consider cases where the *R-L* elements are shunted in parallel (see Figure 3.1), showing that similar vibration damping performance can be delivered. Tang and Wang (2001) conduct a detailed study on the comparison of series and parallel *R-L* circuits. They derive non-dimensional transfer functions and show that by proper tuning of the *R-L* elements, both configurations can yield significant passive vibration damping. They also consider the effects of the *R-L* configurations on active control authority in two different scenarios: voltage driving and current driving. It is demonstrated that both voltage and current inputs can be amplified at the circuit's resonant frequency. In the same article the authors discuss the importance of the electro-

mechanical coupling in the piezoelectric materials. They demonstrate that higher coupling coefficients yield improved vibration damping performance. This is an expected outcome because a larger electro-mechanical coupling enables more vibration energy to be converted to electrical energy, which in turn can then be stored or dissipated in the electrical circuit. Behrens et al. (2003) propose a passive control method to suppress multiple vibratory modes in structures. Their shunt circuit essentially consists of multiple parallel *R-L-C* branches, each targeting a specific mode of vibration. Each branch contains a so-called *current flowing L-C* component that acts as a band-pass filter tuned to the frequency of a certain vibratory mode. This is then followed by a shunting branch which consists of *R-L* elements as in the earlier discussed cases. This way, each branch is tuned according to a certain mode of vibration and only reacts to that particular mode.

Active, semi-active and active-passive hybrid piezoelectric network configurations have also been explored. Hagood et al. (1990) develop a rigorous state-space model for the case where piezoelectric patches are used as actuators in a simple feedback control loop to reduce cantilever beam tip displacement. They experimentally verify their model and show that even a basic compensator loop can provide significant reduction in beam tip vibration. Wang et al. (1996) propose a semi-active control method, where variable inductance and resistance parameters are used as control inputs. They show that the system's response can be minimized for a variety of disturbance scenarios, such as non-periodic and time-varying loads. Tsai and Wang (1999) study more involved active-passive configurations, where two separate piezoelectric elements are connected to different shunts circuits (one active and one passive). Lee and Elliott (2001) consider trajectory tracking, rather than vibration suppression, in a cantilever beam using piezoelectric actuators and measuring tip displacement. They develop a conventional PID

controller and an Internal Model Controller (IMC). They test both control laws using experiments and compare the two control methodologies. Vasques and Rodrigues (2006) study a variety of feedback control laws on a cantilever beam with a pair of piezoelectric patches attached to opposite sides of the root. They consider classical state feedback control, linear quadratic regulator (LQR) and linear quadratic Gaussian (LQC) control laws. They conduct experiments and discuss results in detail, highlighting the advantages of each control method. Further details and comparisons regarding active/passive piezoelectric network configurations are available in Lesieutre (1998) and Tang and Wang (2001).

3.2.Dynamics of a Cantilever Beam and Piezoelectric Network Combination

In this work, a cantilever beam is considered as the host (primary) structure for the theoretical development. Two piezoelectric patches are bonded symmetrically to the beam, as depicted in Figure 3.3. Patch I is shunted to the circuit for control purposes and the other, patch II, is used to introduce external excitation. The configuration described here is a typical benchmark setup and has been studied in relevant literature (Hagood and von Flotow, 1991; Agnes, 1995).

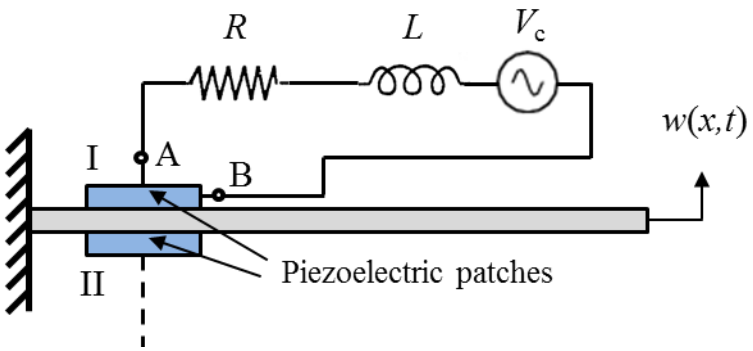

Figure 3.3. Cantilever beam with bonded piezoelectric patches and shunt circuit.

The coupled beam and circuit dynamics is analyzed by adopting a modeling approach from Tang and Wang (2001). The equations of motion for the system are derived by considering an assumed mode truncation for the beam. The transverse displacement for the first mode along the beam is taken as

$$w(x,t) = \phi_1(x)u_1(t) \tag{3.1}$$

where ϕ_1 is the shape function representing the beam's first bending mode and u_1 denotes temporal dynamics (generalized displacement). The assumed mode method and piezoelectric constitutive relations are then used in conjunction with Hamilton's principle to obtain the governing equations as follows.

$$m_{11}\ddot{u}_1 + c_{11}\dot{u}_1 + k_{11}u_1 + k_{em1}Q = F_m$$

$$L\ddot{Q} + R\dot{Q} + k_{ic}Q + k_{em1}u = V_c \tag{3.2}$$

Applying Laplace transformation on (3.2) yields

$$(m_{11}s^2 + c_{11}s + k_{11})u_1(s) + k_{em1}Q(s) = F_{m1}(s)$$

$$(Ls^2 + Rs + k_{ic})Q(s) + k_{em1}u_1(s) = V_c(s). \tag{3.3}$$

Here, m_{11}, c_{11}, k_{11} are the modal mass, damping and stiffness properties associated with the beam's first transverse vibration mode. Q denotes the electrical charge in the shunt circuit. k_{em1}, k_{ic} are the electro-mechanical coupling and inverse capacitance coefficients for the piezoelectric patch, respectively. Notice that these parameters are functions of the mode shape and are thus representative of the first mode dynamics only (see Appendix A for detailed expressions). R, L

are lumped resistance and inductance values of the circuit as depicted in Figure 3.3. F_{m1} denotes the equivalent modal forcing on the beam and V_c is the voltage source in the circuit.

From the equations of motion (3.2), it is apparent how the mechanical beam dynamics and the electrical circuit are coupled through the piezoelectric patch. In fact, the cross-coupling coefficient k_{em1} acts akin to a *spring* element, which is hypothetically positioned between a conventional passive vibration absorber and the primary structure. In this case, the absorber is an electrical circuit.

3.3.Delayed Resonator Application in the Shunt Circuit

A delayed feedback actuation is proposed to implement DR-like tuning in the absorber sub-structure, as discussed earlier in Chapter 1. In the case of the shunt circuit here, the voltage source V_c is used to exert the control law. The feedback sensing can be provided through a variety of sources. An important concern in the selection is to assure clear, consistent signals. An electrical current sensor may not yield satisfactory precision, because the current in the shunt circuit could be as low as micro-ampere levels and contaminated with noise. The voltage drop across the ohmic resistance R or the inductive element L can be measured, however, to obtain measurements proportional to $\dot{Q}$ and $\ddot{Q}$, respectively, both of which typically provide clean signals. In this work we opt for the former, the voltage drop across the resistor element, as the feedback measurement. This voltage drop across the resistor $V_R = R\dot{Q}$ is used in a time-delayed proportional feedback control law as

$$V_c(t) = gR\dot{Q}(t-\tau), \quad V_c(s) = gRs\,\mathrm{e}^{-\tau s}\,Q(s). \tag{3.4}$$

Substituting (3.4) in (3.3), the transfer function between the circuit's electric charge and the beam displacement becomes

$$\frac{Q(s)}{u_1(s)} = \frac{-k_{em1}}{Ls^2 + Rs + k_{ic} - gRs\,\mathrm{e}^{-\tau s}} \tag{3.5}$$

while the dynamics for beam displacement is

$$\frac{u_1(s)}{F_m(s)} = \frac{Ls^2 + Rs + k_{ic} - gRs\,\mathrm{e}^{-\tau s}}{(m_{11}s^2 + c_{11}s + k_{11})(Ls^2 + Rs + k_{ic} - gRs\,\mathrm{e}^{-\tau s}) - k_{em1}^2}\,. \tag{3.6}$$

The denominator of (3.5) is the characteristic equation for the shunt circuit sub-structure. Notice that it also appears identically in the numerator of (3.6). These observations provide insight to the principles of DR theory. When feedback gain g and delay τ are tuned correctly, the circuit sub-structure is brought to resonance at a certain frequency ω. That is,

$$Ls^2 + Rs + k_{ic} - gRs\,\mathrm{e}^{-\tau s}\Big|_{s=\omega \mathrm{i}} = 0\,. \tag{3.7}$$

The actively-tuned electrical circuit now acts as an ideal dynamic absorber. This consequently should result in a complete suppression of the tonal response of the beam, as it is apparent from (3.6). As discussed under Chapter 1, the necessary DR tuning parameters g and τ are obtained by solving the amplitude and phase conditions of (3.7), respectively.

$$g(\omega) = \frac{(-1)^{l-1}}{R\omega}\sqrt{(R\omega)^2 + (k_{ic} - L\omega^2)^2}\,,$$

$$\tau(\omega) = \frac{1}{\omega}\left[\tan^{-1}\left(\frac{k_{ic} - L\omega^2}{R\omega}\right) + (l-1)\pi\right],\ \ l = 1,2,\ldots. \tag{3.8}$$

As expressed earlier, in such DR applications, the asymptotic stability of the combined system is of paramount concern. The DR absorber substructure (in this case the piezoelectric network) is marginally stable (i.e., resonant) by the very definition of 'tuning'. At the same time the combined system (beam coupled with piezoelectric network) has to remain asymptotically stable. Clearly the characteristic equation representing the coupled dynamics [i.e., the denominator of (3.6)] is different than the circuit's characteristic equation (3.7). The stability of this dynamics needs to be assessed and taken into consideration during the synthesis of the control. In other words, the selected feedback parameters g and τ as in (3.8) must not invite instability for the coupled system. In accordance with the notation defined in (1.4) under Section 1.3, the combined system's characteristic equation can be expressed from (3.6) as

$$A(s) + B(s) g\, \mathrm{e}^{-\tau s} = 0\,, \text{ with}$$

$$A(s) = (m_{11}s^2 + c_{11}s + k_{11})(Ls^2 + Rs + k_{ic}) - k_{em1}^2\,, \quad B(s) = -Rs(m_{11}s^2 + c_{11}s + k_{11}) \qquad (3.9)$$

The expressions derived as in (1.5) can then be used to calculate the combined system's stability boundaries. The first mode assumption for the cantilever beam is kept in mind when discussing the stability of the combined system. As noted by an anonymous referee, this modal truncation causes some loss of accuracy in determining the stability bounds. In general, however, taking only the first mode into account provides sufficient accuracy when generating stability boundaries. In order to increase confidence in this conviction a dual-mode model was examined in comparison to a single-mode one during numerical case studies. The stability boundaries obtained for the two cases are nearly identical (discussed further during the numerical case study), fortifying the assumption that the stability characteristics are captured with sufficient fidelity using the single-mode approach.

3.4.Energy Harvesting Capacity and Delayed Feedback

An analytical framework to implement a DR-based feedback control has readily been developed in the previous section. The findings under Chapter 2, namely the effects of delayed feedback on energy harvesting capacity can be directly applied on this construct. The theory developed earlier is on a mechanical vibration absorber, where it is assumed that the damper element is replaced by a transducer that can extract energy, while the force actuator consumes energy. The piezoelectric network is a direct analogy. The resistor in the shunt circuit is assumed to be a *resistive load* that enables energy harvesting, while the voltage source used for the feedback control consumes energy (see Figure 3.4). In general, energy harvesting circuits are quite complex and feature many components such as bridge rectifiers (for AC to DC conversion), flyback converters, DC-DC step-down converters, field-effect transistors (FETs) and pulse width modulation (PWM) controls (Sodano et al., 2004). In fact, optimization of energy harvesting circuitry is an active research topic on its own (Ottman et al., 2002; Lefeuvre, 2005; Kong et al., 2010) and it is out of the scope of this research.

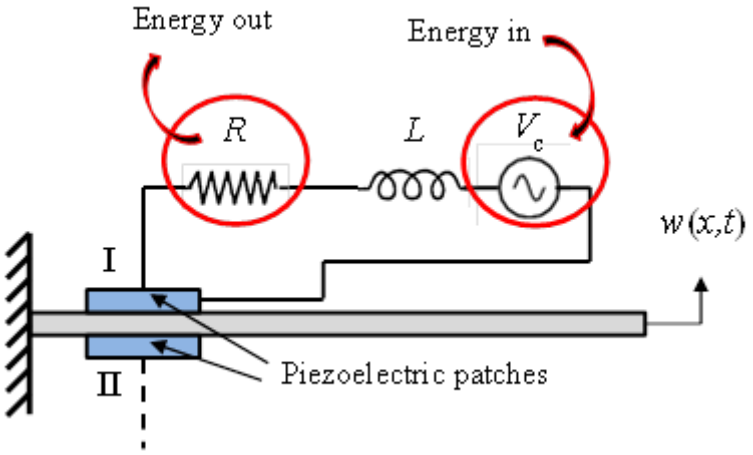

Figure 3.4. Energy flow in the piezoelectric network with control input.

Assessing energy harvesting capacity using a resistive load provides an accurate measure for several reasons. First of all, some specialized energy harvesting circuits are specifically designed to have resistive impedance. For instance Kong et al. (2010) mention that maximum power transfer from a fixed AC source is achieved if the load impedance is the complex conjugate of the source impedance (Dorf and Svoboda, 2010). However they argue that direct impedance matching is usually not practical due to high inductance requirements. Instead they propose the use of resistive loads that match the source impedance. Researchers that study more advanced energy harvesting circuit topologies such as Ottman et al. (2002) also use resistive loads as an initial measure of available power for harvesting. Furthermore, they use the values obtained by resistive loads as a baseline for assessing power conversion losses of their specialized circuits. Roundy and Wright (2004) provide a detailed study on the design of a piezoelectric vibration based generator for wireless electronics. They use a resistive load as the first assessment of the energy harvesting capacity of their system. We follow a similar approach in this work and assume that the resistor in the shunt circuit is a resistive load in order to estimate how much power can be delivered to an electrical load.

Let us now study the expressions for energy that is available from the resistive load and the amount that is required for active tuning. The approach follows closely the development under Section 2.4. Power generated from the resistive load is

$$P_{gen} = Ri^2 . \tag{3.10}$$

Under harmonic excitation, assume $i(t) = i_0 \sin(\omega t)$, which yields

$$P_{gen} = Ri_0^{\,2} \sin^2(\omega t) . \tag{3.11}$$

For one oscillation period $T = 2\pi/\omega$, energy generated per cycle is expressed as

$$E_{gen}^{T} = Ri_0^{\,2}\int_0^T \sin^2(\omega t)dt = \frac{Ri_0^{\,2}\pi}{\omega}. \tag{3.12}$$

Then average power generated over a period becomes

$$P_{gen}^{av} = \frac{E_{gen}^{T}}{T} = \frac{Ri_0^{\,2}}{2}. \tag{3.13}$$

Instantaneous power consumed by the voltage source for the feedback control can be obtained by multiplying the control voltage and the current in the circuit.

$$P_{ctrl} = V_c i = gRi(t-\tau)i(t) = gRi_0^2 \sin(\omega t - \omega\tau)\sin(\omega t) \tag{3.14}$$

The energy consumed per cycle is

$$E_{ctrl}^{T} = gRi_0^{\,2}\int_0^T \sin(\omega t + \theta - \omega\tau)\sin(\omega t + \theta)dt = \frac{gRi_0^{\,2}\pi\cos(\omega\tau)}{\omega} \tag{3.15}$$

and average power consumed over a period becomes

$$P_{ctrl}^{av} = \frac{E_{ctrl}^{T}}{T} = \frac{gRi_0^{\,2}\cos(\omega\tau)}{2}. \tag{3.16}$$

Now that relations for generated and consumed power are derived, the net harvestable energy can be defined as the difference. Subtracting (3.16) from (3.13), we obtain

$$P_{harv}^{av} = P_{gen}^{av} - P_{ctrl}^{av} = \frac{Ri_0^{\,2}}{2}[1 - g\cos(\omega\tau)]. \tag{3.17}$$

Note that the current in the circuit is the time derivative of charge. That is,

$$i(t) = \dot{Q}(t) \quad \text{and} \quad i(s) = sQ(s) \tag{3.18}$$

and the transfer function between circuit current and external mechanical forcing can be expressed as

$$\frac{i(s)}{F_m(s)} = \frac{-sk_{em1}}{(m_{11}s^2 + c_{11}s + k_{11})(Ls^2 + Rs + k_{ic} - gRs\,\mathrm{e}^{-\tau s}) - k_{em1}^2} \tag{3.19}$$

using the transfer functions (3.5) and (3.6). Then for a given excitation frequency ω, external forcing F_{m} and control parameters (τ, g), the current amplitude i_0 can easily be obtained from the frequency response function by substituting $s = \omega\mathrm{i}$ in (3.19).

3.5.Numerical Case Study

A numerical case study is presented in this section in order to demonstrate the results developed in this chapter. We consider a cantilever beam with bonded piezoelectric plates, one of which is shunted to a circuit, as depicted in Figure 3.3. This is a common setup used in analytical and experimental research. As such, many studies exist in literature where this construct is studied. We adopt the system parameters from a sample research work that involves experiments, in order to provide a realistic case. We first demonstrate a DR application where the shunt circuit is tuned with a feedback control and brought to resonance at the excitation frequency. Simulations are presented to show the vibration absorption performance. On the same construct, we also consider a different control tuning scheme in order to enhance energy harvesting capacity.

For the case study here we consider the system parameters corresponding to the experimental setup used in Tang and Wang (2001). The main structure is an aluminum cantilever

beam of 0.3 m length, and a pair of PZT 5A type piezoelectric patches are attached to its root on the opposite beam surfaces. Using the physical parameters provided under Table 1 in the cited document in conjuncture with the expressions for modal parameters given in Appendix A, the system characteristics corresponding to the notation in (3.2) are obtained as: $m_{11} = 0.0981$ kg, $c_{11} = 0.0393$ Ns/m, $k_{11} = 3929.4$ N/m, $k_{em1} = -20665$, $k_{ic} = 9.8693 \times 10^6$ F^{-1}. The parameters associated with the PZT patches are further corrected by measurements and reported as $k_{em1} = -23233$, $k_{ic} = 10.087 \times 10^6$ F^{-1}. For the synthesis of the shunt circuit parameters, inductance (L) and resistance (R), the authors implement an approach based on passive vibration absorber design by Den Hartog (1956). Following this method, the circuit parameters are calculated as $L = 246$ H and $R = 7.3166$ kΩ, although the authors report that through experimental observations, a slightly changed inductance value of $L = 249.5$ H yields more optimal results. All system parameters associated with the open loop system as defined in (3.2) are now identified.

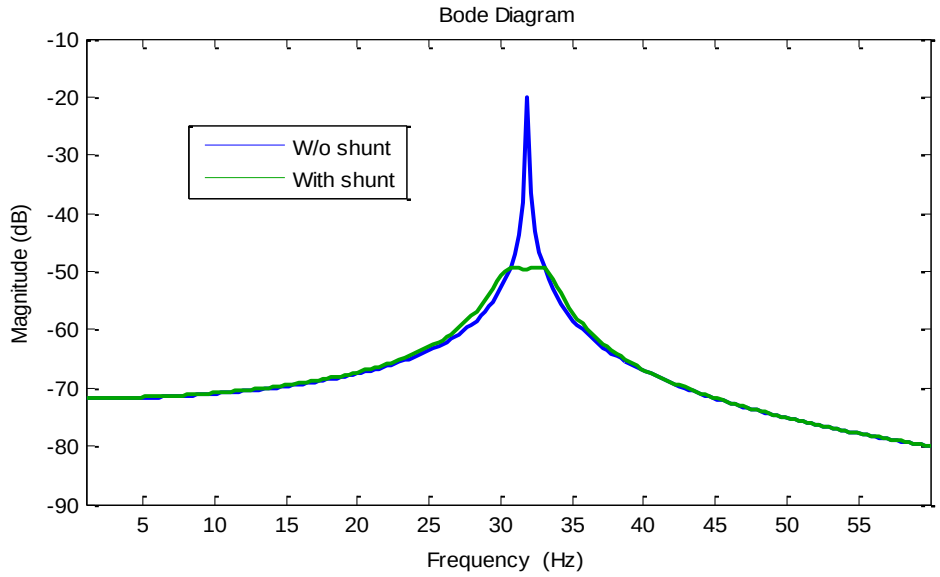

Figure 3.5. Frequency response of beam displacement with and without the shunt circuit.

The frequency response of the beam's general displacement versus mechanical forcing, $u_1(s)/F_{m1}(s)$, is depicted in Figure 3.5 with and without the shunt circuit. This figure clearly shows the passive vibration damping performance of the shunt circuit, as the peak response magnitude is reduced by about 30 dB. On this construct, we now deploy the DR strategy with the aim of completely eliminating vibration against harmonic excitation. As mentioned under Section 3.3, we consider a feedback control as in (3.4), where the voltage across the resistor is the measurement signal and the control action is applied to the circuit using a voltage source. Then the control gain g and delay τ required for DR tuning as defined in (3.8), can now be calculated for this case. The combined system's stability boundaries are also calculated, from the expressions in (3.9) and (1.5). The control parameters and the stability boundaries are presented together in Figure 3.6, where frequency is incorporated in the Z-axis (not visible due to 2-D top-view). A zoomed view to the first negative branch is also included in this figure.

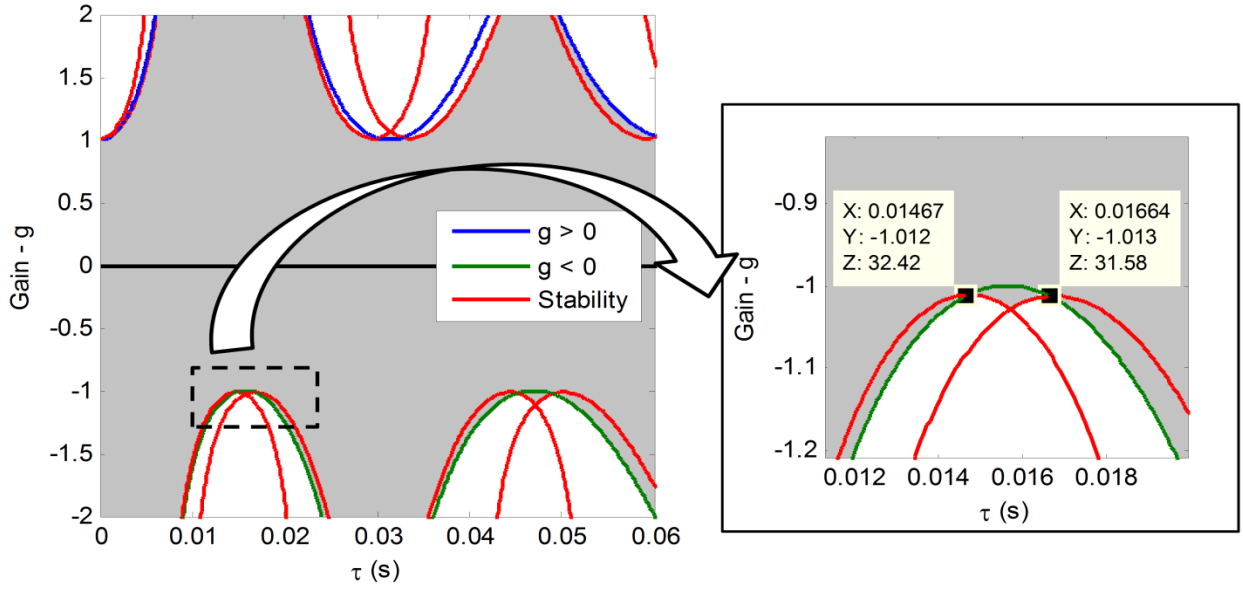

Figure 3.6. DR tuning parameters and combined system stability boundaries. Stable region shaded.

What is immediately apparent from Figure 3.6 is the limited range of frequency at which the DR tuning can operate. The combined system stability boundaries (in red) are severely restricting the choice of control parameters, and rather small sections of the control parameter loci (blue and green curves) fall in the gray-shaded stable zone. In the zoomed pane, the frequency limits for the first negative (τ, g) branch are shown to be $\omega_{min} = 31.58$ Hz and $\omega_{max} = 32.42$ Hz. In order to demonstrate DR operation, let us consider a simulation where the beam is subject to a modal mechanical forcing with 10^{-3} N amplitude and a frequency of 32 Hz. This frequency falls in the feasible interval as declared earlier. For this frequency, the DR tuning parameters are calculated on the first negative branch as $g = -1$ and $\tau = 0.0156$ s. Simulation results for the beam's generalized displacement and the shunt circuit current are presented in Figure 3.7.

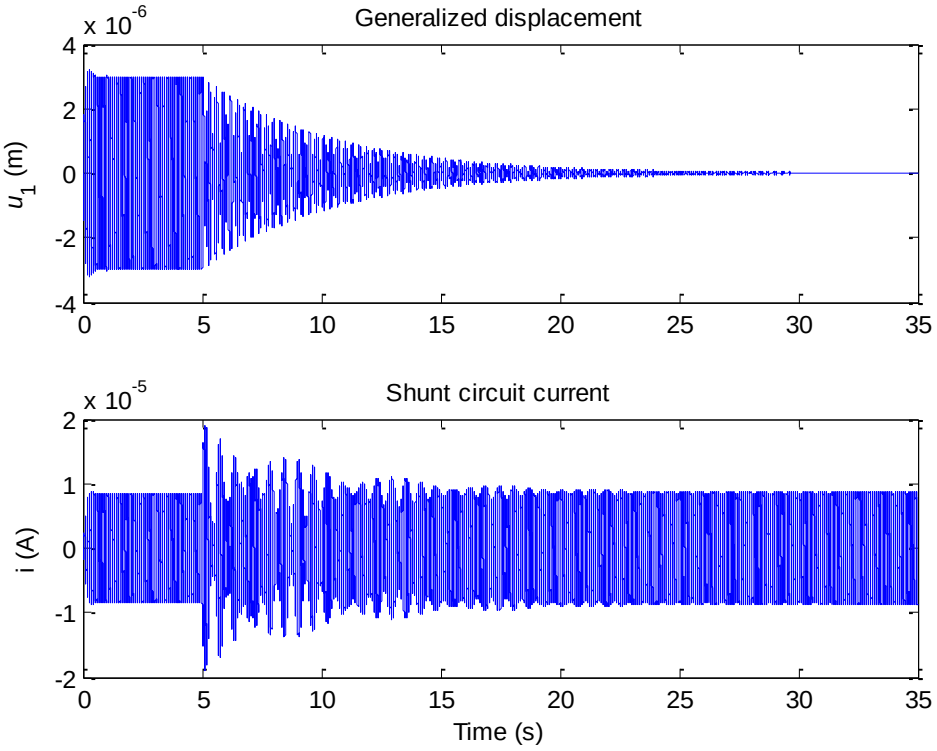

Figure 3.7. Simulation results for sample DR operation. Control turned on at $t = 5$ s.

Here, the control is inactive until $t = 5$ s, and it is turned on afterwards. Notice how the beam displacement ultimately completely ceases, however after a long settling time. The transient behavior can be explained by nature of the system's stability tableau as depicted in Figure 3.6. As it was mentioned earlier, the DR tuning parameters are quite close to the combined system's stability boundary. A (τ, g) composition *on* any these (combined system) stability boundaries would render a marginally stable system with a pair of purely imaginary characteristic roots. Because the DR tuning parameters are close to the stability boundaries, the dominant characteristic roots of the combined system dynamics will be close to the imaginary axis, with small real components. Now let us further note that in the zoomed section of Figure 3.6 it is quite apparent that *two* system stability curves intersect. Each of these curves corresponds to a purely imaginary characteristic root pair, as mentioned before. As a result, at (τ, g) compositions where these corves are in *close vicinity*, it is expected to see *two* dominant complex conjugate roots. At the (τ, g) point where these two curves *intersect*, one should expect to see *two* purely imaginary characteristic roots. The existence of two dominant conjugate root pairs is also apparent from the time-domain simulation. A closer look at Figure 3.7 shows a *beating* phenomenon; a typical characteristic of two comparable frequencies.

One method to further supplement these remarks and observations is to look at the system's dominant characteristic roots themselves. Unfortunately the combined system's characteristic equation is an infinite-dimensional quasi-polynomial, as seen in (3.9). For this reason it is impossible to solve the roots analytically. However this task can be accomplished through certain numerical routines. One such method is the Quasi-Polynomial Mapping based Root finder (QPmR), developed by Vyhlídal and Zitek (2009), used earlier under Section 2.5. Utilizing this routine, the dominant characteristic roots of the system are numerically calculated

and depicted in Figure 3.8. First of all, notice the real part of the dominant root, $\mathrm{Re}[s_{dom}] = -0.1748\ \mathrm{s}^{-1}$. This corresponds to a 2% settling time of approximately 22 second, which is agreement with the time-domain results seen in Figure 3.7. Another important observation is the similarity of the imaginary parts of the two conjugate pairs. They are seen in Figure 3.8 as 189.9 rad/s and 210.8 rad/s, or 30.2 Hz and 33.5 Hz, respectively. As the imaginary parts of the dominant roots dictate the frequencies of transient oscillations, this explains the beating phenomenon in time-domain, as mentioned earlier.

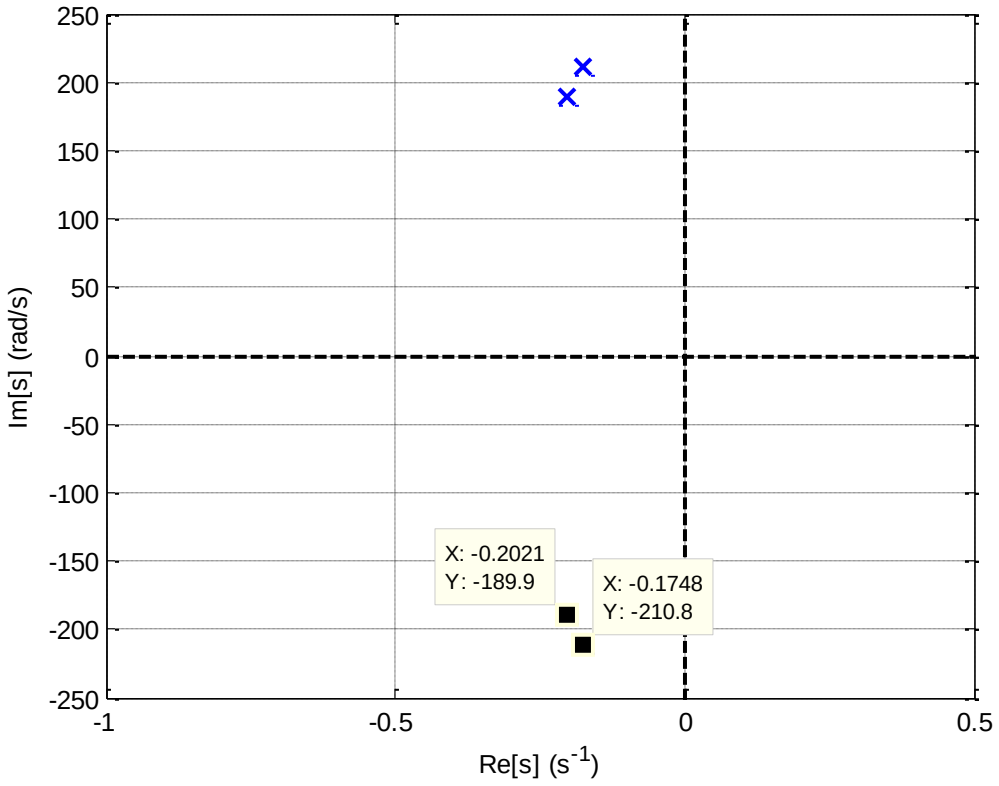

Figure 3.8. Dominant characteristic roots of the system for $g = -1$ and $\tau = 0.0156$ s.

Now that vibration suppression using DR tuning in a piezoelectric network is demonstrated numerically, let us consider the energy harvesting aspect. On the same sample

system, we now adjust the feedback law such that the shunt circuit is tuned to near-resonance. The control parameters are tuned according to the DFVA approach discussed under Section 2.3.

$$g_1(\omega) = \frac{(-1)^{l-1}}{R\omega}\sqrt{(\alpha R\omega)^2 + (k_{ic} - L\omega^2)^2}\,,$$

$$\tau_1(\omega) = \frac{1}{\omega}\left[\tan^{-1}\left(\frac{k_{ic} - L\omega^2}{\alpha R\omega}\right) + (l-1)\pi\right],\ \ l = 1,2,\ldots. \tag{3.20}$$

Notice that the equations were originally devised for a mechanical vibration absorber structure, and they are here adapted to the electrical shunt circuit. Accordingly, the RPF α is applied to the resistor which serves as the *damper* in the electrical structure. Here we consider a sample case where α = 0.7, and the near-resonant tuning parameters seen in (3.20) are calculated accordingly. They are presented along with the DR parameters and the combined system stability in Figure 3.9. As in the case of Figure 3.6, we focus on the first negative branch. Notice from Figure 3.9 that near-resonant tuning parameters are always in the stable zone. As such, the operating frequency limitation encountered during DR operation is not as strict here. Although the shunt circuit can be tuned over a wider frequency range, doing so does not guarantee favorable operation by itself. One must also consider the passive energy harvesting performance and compare it with the actively tuned case in order to assess feasibility. As in the case of the DR simulation, we assume that the beam is subject to a harmonic modal mechanical forcing with 10^{-3} N amplitude. This time we keep the excitation frequency ω as an independent parameter such that energy harvesting performance with respect to frequency can be analyzed.

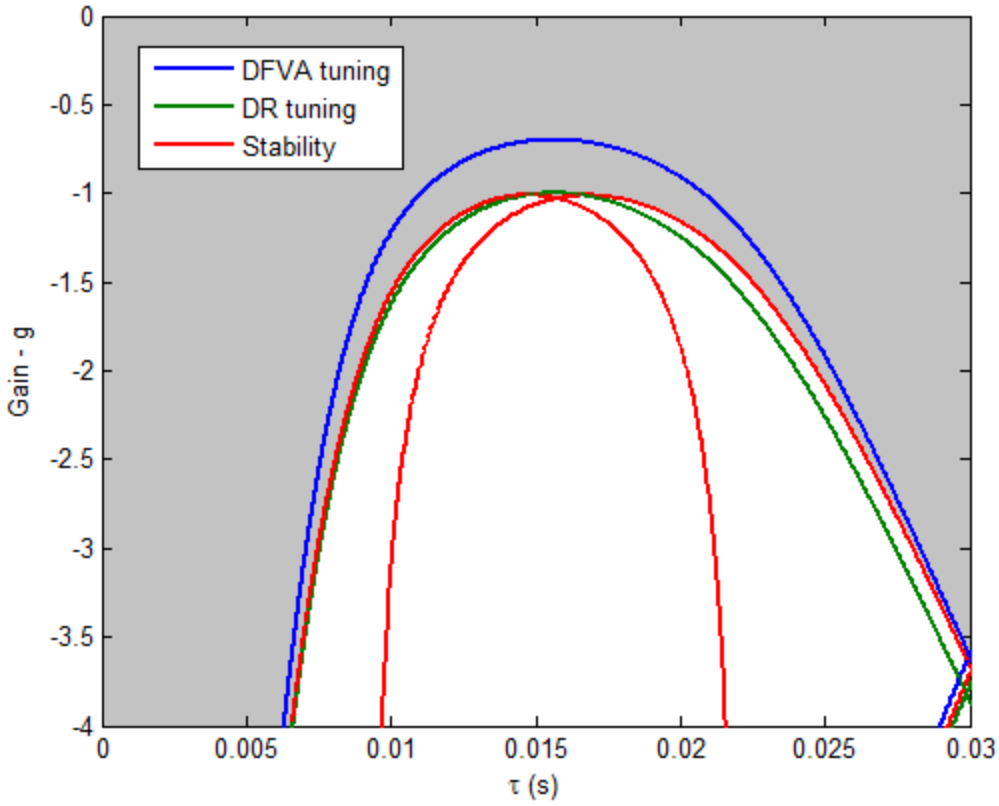

Figure 3.9. Control parameters for near-resonant tuning with $\alpha = 0.7$. DR parameters and combined system stability boundaries also shown. Stable zone shaded.

Using the near-resonant tuning parameters as in (3.20), we calculate the shunt circuit current from the transfer function (3.19) for various values of α. The energy harvesting performance can then be assessed using the relations in (3.13), (3.16) and (3.17). The passive case is also considered for comparison. To calculate passive energy harvesting performance, $g = 0$ is substituted in all relevant equations, and the process is repeated. These results are presented in Figure 3.10, where relative increase in energy harvesting capacity is also shown in percentiles. This quantity, percent increase (*PI*) in energy harvesting, is calculated as

$$PI = \frac{(P_{harv}^{av})_{active} - (P_{harv}^{av})_{passive}}{(P_{harv}^{av})_{passive}} \times 100\,. \tag{3.21}$$

That is, the difference between active and passive energy harvesting capacity, divided by the passive quantity and multipled by 100 to express as percentage.

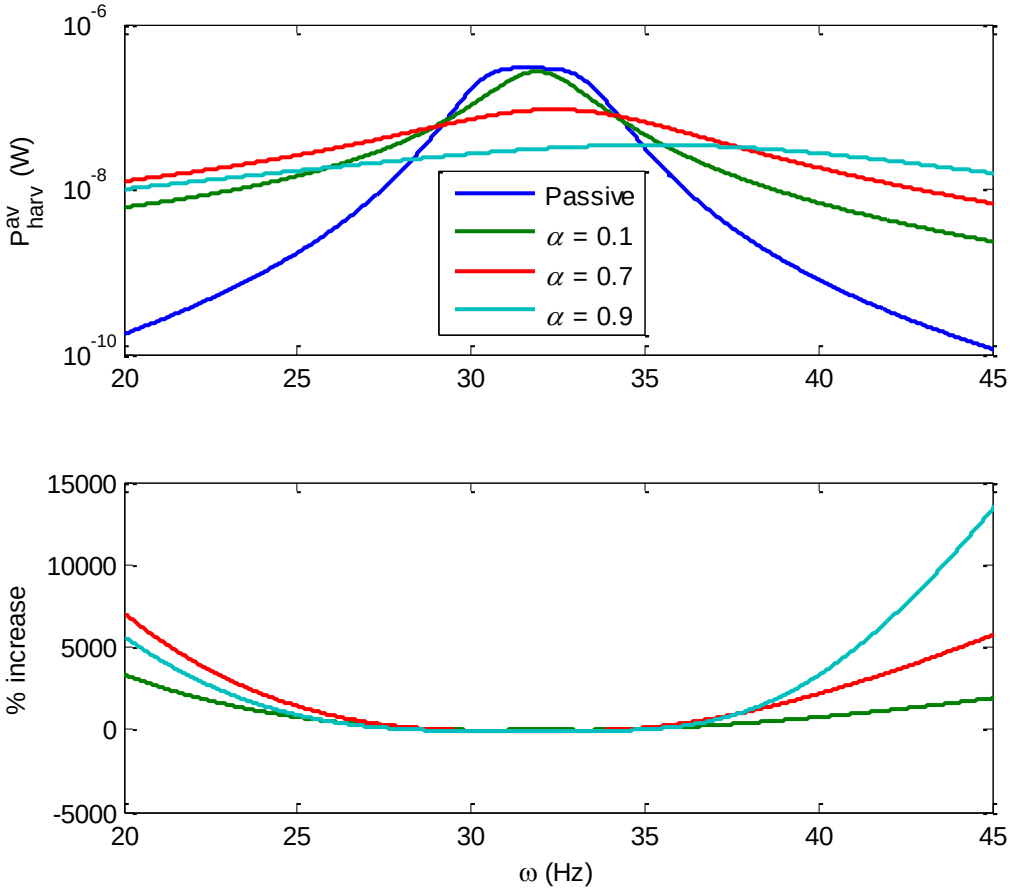

Figure 3.10. Energy harvesting capacity with respect to frequency for various values of α and passive system. Relative increase in energy harvesting capacity also shown.

An important revelation from Figure 3.10 is that the active DFVA tuning scheme does not perform better than the passive system for certain frequencies. It is observed that in a roughly 5 Hz band centered at the natural frequency, the passive system offers higher energy harvesting

capacity. However when the operating frequency is moved away from the vicinity of resonance, the active tuning scheme enables significant increases in energy harvesting capacity. Regarding the effect of the RPF, it is noted that higher α decreases energy harvesting performance close to the resonant frequency, but results in higher energy harvesting elsewhere. On the contrary, small α values seem to act similar to the passive case; a peaking energy harvesting capacity close to the resonant frequency, and decreasing performance as frequencies move away from resonance. However even a relatively small value of $\alpha = 0.1$ seems to yield a significant increase in energy harvesting capacity compared to the passive case, except a narrow frequency band in the vicinity of the system's resonance.

3.6.Detailed Aspects and Discussion

In this section some detailed analysis are presented, which were left out from earlier parts of the text in order not to disrupt the flow. Under Section 3.3, the stability of the combined beam and circuit dynamics was discussed. It was noted that the beam is in reality a distributed system and has infinite dimensional dynamics. However for the purposes of this study, the first bending mode was assumed to be sufficiently representative. This assumption is further scrutinized here in order to provide more comfort in the modeling approach. We study a dual mode model for the beam and compare how the number of assumed modes influences the combined stability outcome. As a sample system, the same construct that is considered under the case study is used. Details on the dual mode modeling approach, including the combined system's characteristic equation are available later within this text, under Chapter 4. Using the data from Tang and Wang (2001) and Table 1 wherein, the mathematical model with dual mode beam is derived and the characteristic equation obtained. The stability boundaries for the enhanced model are calculated using (1.5), as the characteristic equation can again be represented in the form of

(1.4). The stability boundaries are then presented in superimposed form on the stability tableau in Figure 3.6; more specifically on the zoomed section so that differences in the boundaries can be observed clearer. The result is presented in Figure 3.11. As seen here, the increase in model complexity from single mode to dual mode only results in a marginal change in the combined stability boundaries. As such, we conclude that the single mode beam model provides sufficient accuracy for stability assessment purposes.

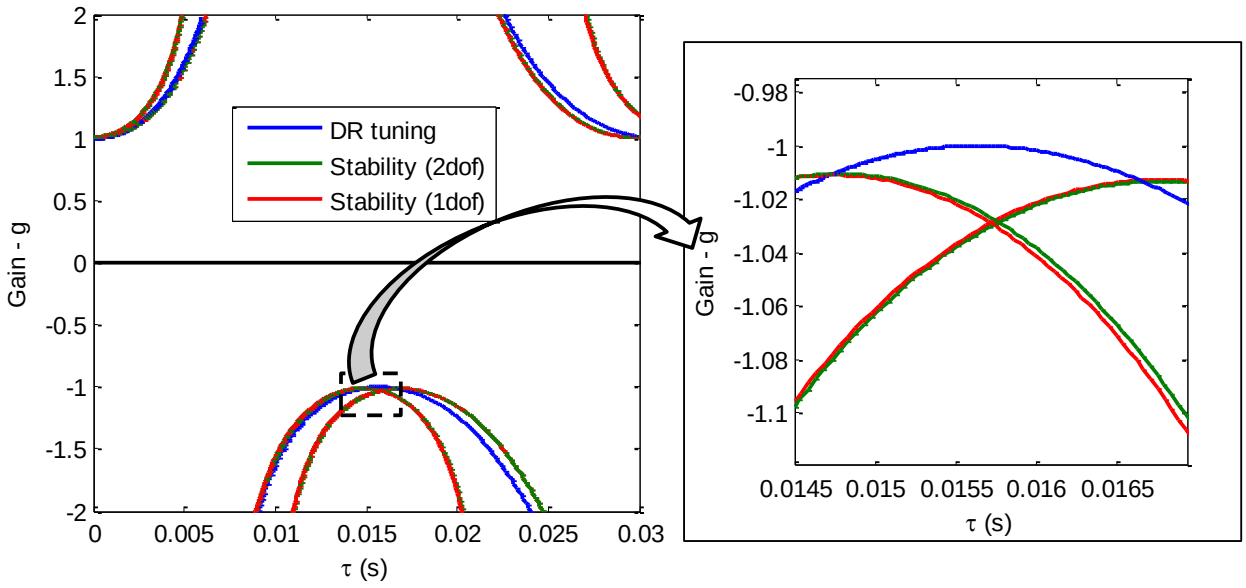

Figure 3.11. DR tuning parameters and combined system stability boundaries with single (1 DOF) and dual mode (2 DOF) beam models.

The second aspect that is investigated in depth is the position of the combined system stability boundaries relative to the DR tuning parameters, and the resulting limitation on operating frequencies. During the case study under Section 3.5, a benchmark piezoelectric shunt network was used as a basis for DR implementation. The shunt circuit parameters, namely inductance L and resistance R were designed for passive vibration absorption. Although the circuit provides satisfactory passive performance (see Figure 3.5), during DR implementation it

was observed that the operating frequency range was severely restricted between ω_{min} = 31.58 Hz and ω_{max} = 32.42 Hz. We shall now investigate whether some system parameters can be adjusted to provide a wider operating frequency range. The primary structure, in this case the cantilever beam, is considered off-limits for design purposes. Instead, the absorber structure, in this case the shunt circuit parameters are available as design selections. Notice that the capacitance in the circuit is due to the PZT patch and as a result, it cannot be altered either. Then the remaining parameters to study are *R*-*L* components.

Regarding inductance, the design methodology used by Tang and Wang (2001) dictates *L* needs to be adjusted such that the circuit's natural frequency matches that of the beam. During numerical investigations it was observed that altering the inductance does not provide a wider operating frequency range, but rather *shifts* the operating frequency interval. For instance, altering the inductance to L = 224.6 H instead of the original value of 249.5 H changes the frequency range to ω_{min} = 33 Hz and ω_{max} = 34 Hz. However, this change also comes with a decrease in passive vibration damping performance, as seen in Figure 3.12. The influence of variations in resistance *R* in the shunt circuit is also considered. It is observed that increasing *R* provides a wider range of operating frequency, but again results in reduced passive vibration absorption performance. For instance, increasing original resistance value of 7.3166 kΩ by three-fold to R = 21.9498 kΩ only results in a marginal increase in operating frequency range with ω_{min} = 31.21 Hz and ω_{max} = 32.71 Hz, as shown in Figure 3.13.

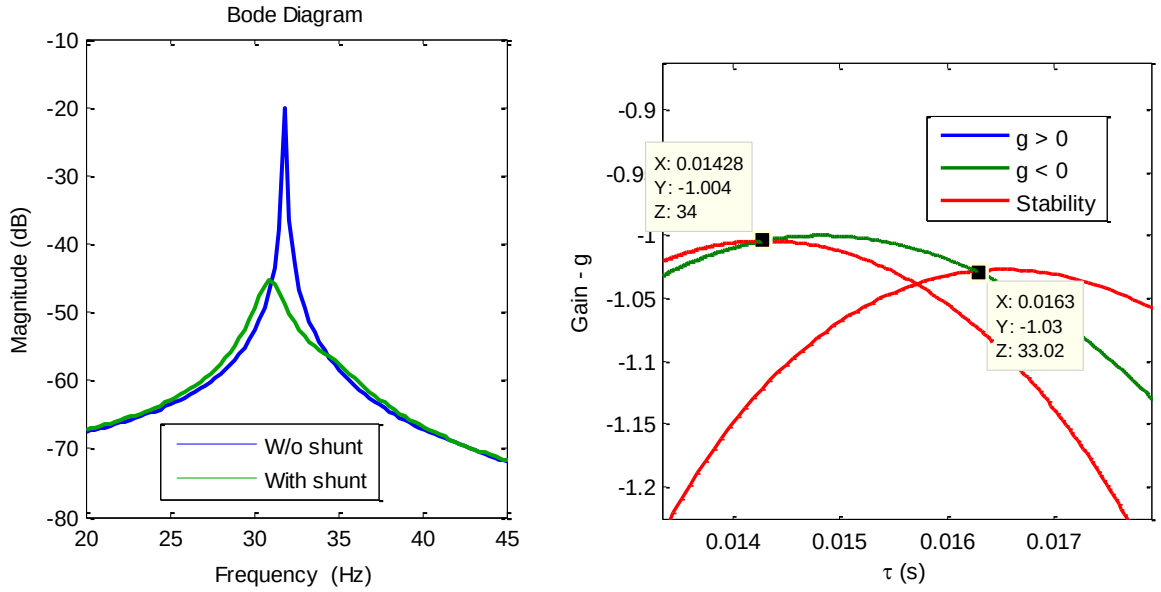

Figure 3.12. Passive shunt damping performance (left) and stability tableau (right) for the case where inductance is decreased to L = 224.6 H.

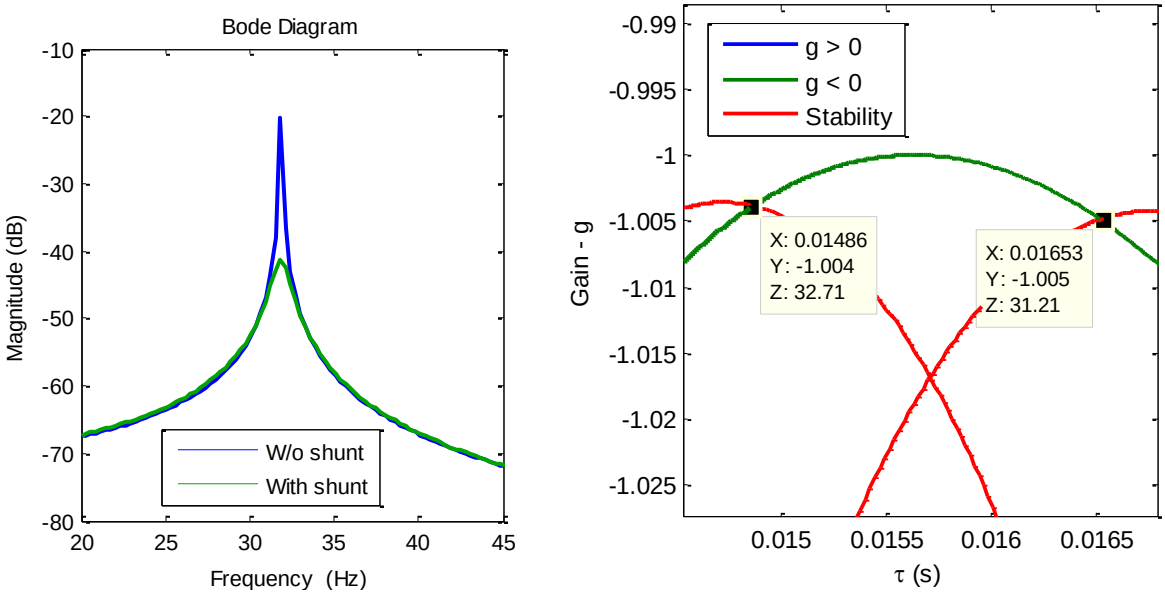

Figure 3.13. Passive shunt damping performance (left) and stability tableau (right) for the case where resistance is increased to R = 21.9498 kΩ.

The findings presented here indicate that the design of the shunt circuit components, namely the inductance and resistance only has limited influence on the DR tuning frequency range. The most likely reason for this is that the primary structure, in this case a cantilever beam, is very lightly damped and exhibits a sharp peak as its frequency response. In other words, the primary structure vibrates very significantly at a relatively narrow frequency band, centered on its natural frequency. At frequencies away from this peak, the response is rather weak and insignificant. For this reason an effective tuning only becomes possible at this narrow frequency range where the primary structure actually exhibits measurable and observable levels of vibration. If the primary structure of concern has a wider (i.e., more spread-out) frequency response, tuning the DR over a larger ranges of frequencies would be possible and in fact necessary.

To supplement this conjecture, let us present one final numerical example. Here, we alter the damping characteristic of the primary structure. By increasing the damping ratio, the structure's frequency response should widen, instead of having a sharp peak. In the case study we considered so far, Tang and Wang (2001) report the damping ratio as $\zeta = 0.001$ (and corresponding $c_{11} = 0.0393$ Ns/m). For the sake of demonstrating our point, we increase the damping five-fold, to $\zeta = 0.005$ ($c_{11} = 0.1965$ Ns/m) and repeat the previous analyses. The results are presented in Figure 3.14. Notice how the frequency range has increased to $\omega_{min} = 30.97$ Hz and $\omega_{max} = 33.14$ Hz, which is the widest among the cases tested so far. As a result, it is fair to declare that the feasible operating frequency interval for DR tuning is mostly dependent on the damping characteristics of the primary structure.

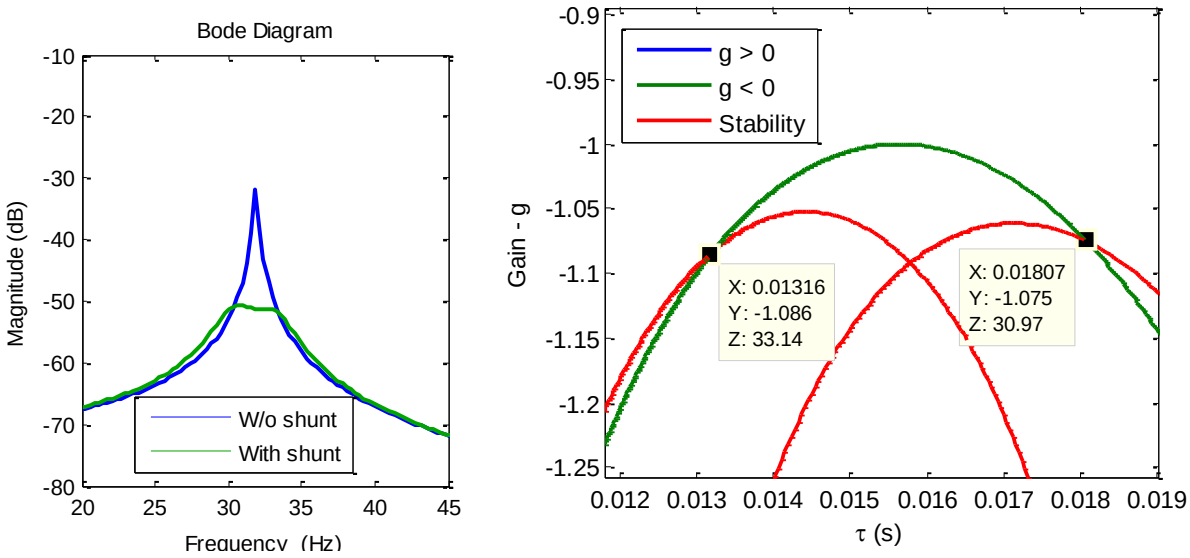

Figure 3.14. Passive shunt damping performance (left) and stability tableau (right) for the case where damping of primary structure is increased to $\zeta = 0.005$ ($c_{11} = 0.1965$ Ns/m).

3.7.Summary

Piezoelectric networks are discussed in this chapter as an application platform for vibration control and energy harvesting using delayed feedback control. Piezoelectric materials are used in a wide variety of transducers such as stack actuators/sensors and bender type plate actuators/sensors. In this work we focus on bender-type elements, which are essentially PZT plates that can be attached on structures such as beams and membranes. We consider a cantilever beam as the primary structure. The PZT elements generate electrical charge in reaction to the beam's bending-induced strain. When connected to an *R-L* circuit, the beam and circuit dynamics become coupled differential equations, yielding an analogous system to traditional mechanical vibration absorbers. We propose a feedback control system in the shunt circuit. The voltage across a lumped resistor is measured and used as the feedback signal. By using a delayed proportional control, we implement the delayed resonator control tuning approach, rendering

complete resonance in the circuit at certain target frequencies. When the circuit is tuned properly, it is able to absorb all vibration in the beam coming from a harmonic excitation. We deploy the proposed methodology on a sample system adopted from literature. It is demonstrated that the combined system's stability boundaries introduce strict limitations on the frequency range within this method can be utilized. A time-domain simulation is presented to demonstrate vibration suppression performance. In addition to vibration control, we also extend our findings on energy harvesting to piezoelectric networks. It is shown that certain control tuning approaches may provide significant increase in energy harvesting capacity.

Chapter 4. Experimental Studies and Application of the Theory

4.1.Experiments on Delayed Resonator Implementation in Piezoelectric Networks

4.1.1. Description of experimental setup

A laboratory setup was built to serve as a test bed for the developed theory. A diagram of the experiment is shown in Figure 4.1 and the main components are depicted in Figure 4.2. A steel beam (0.279 m length, 3 mm × 25 mm profile) is clamped from one end in a cantilever configuration. The anchor which supports the beam is hosted on a Kinetic Systems Vibraplane pneumatic table. This assures that the experiment is isolated from ambient disturbances. As described earlier, two lead zirconate titanate (PZT) piezoelectric patches (Steiner & Martins SM410) are attached symmetrically on either side of the beam, close to the clamped end. The patches are bonded to the beam surface using 3M Scotch-Weld DP100 two-part epoxy adhesive. One of the patches is used to generate the external excitation, driven by the signal from an AVC 790 series power amplifier connected to a B&K Precision 4017A function generator. The other patch is connected to the shunt circuit, constructed on an E&L Instruments Elite 3 Circuit Design Test System, to form the piezoelectric network. A PHILTEC D63-H1 high-precision fiber-optic displacement sensor is positioned close to the beam tip to monitor its motion. The voltage drop across the resistor is measured using a Texas Instruments INA117 differential amplifier. This voltage difference measurement is the main feedback signal and it is fed to a dSPACE DS1103 MicroAutoBox digital control unit, along with the displacement sensor output. The control loop is constructed in Simulink, and downloaded automatically on the digital controller through dSPACE Real-Time Interface. The control actuation signal is fed to another AVC 790 series

power amplifier which is connected to the shunt circuit, to close the loop. dSPACE ControlDesk software is used to monitor and regulate the control action (Figure 4.3).

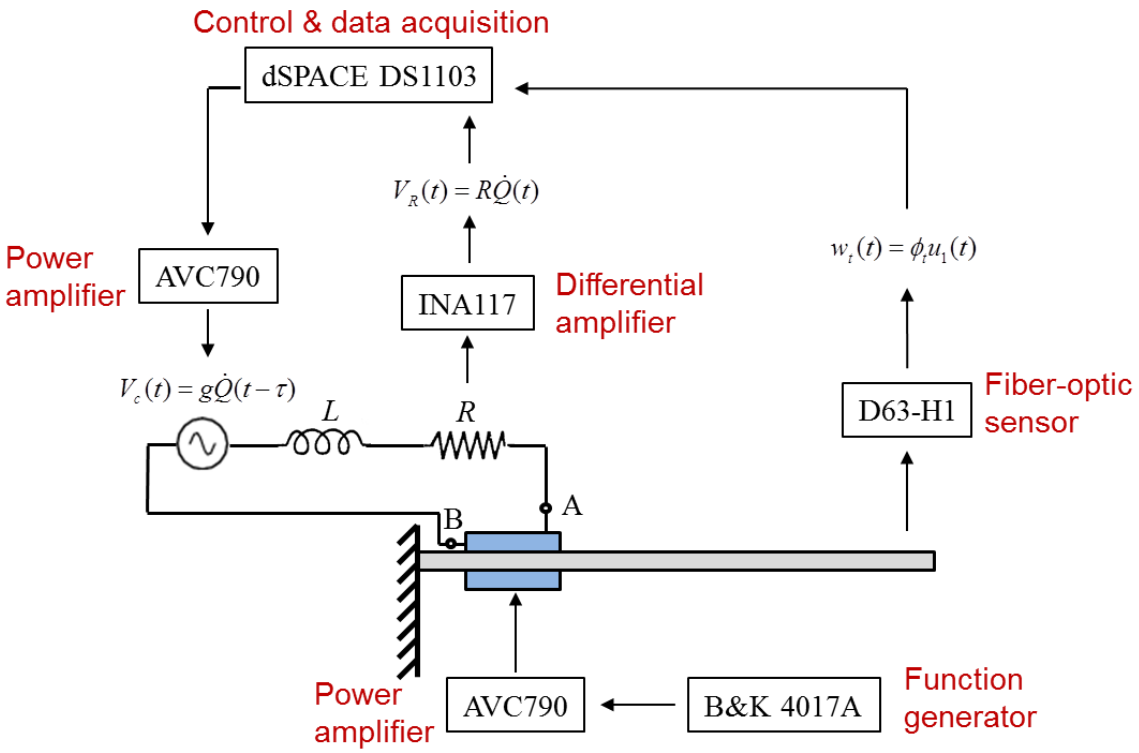

Figure 4.1. Diagram of the experimental setup.

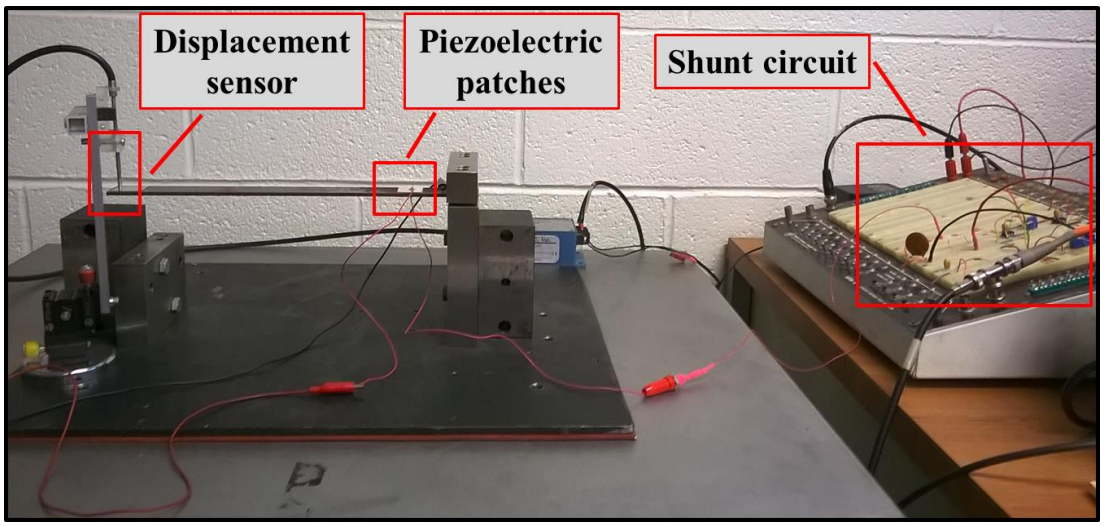

Figure 4.2. Cantilever beam with bonded piezoelectric patches and shunt circuit.

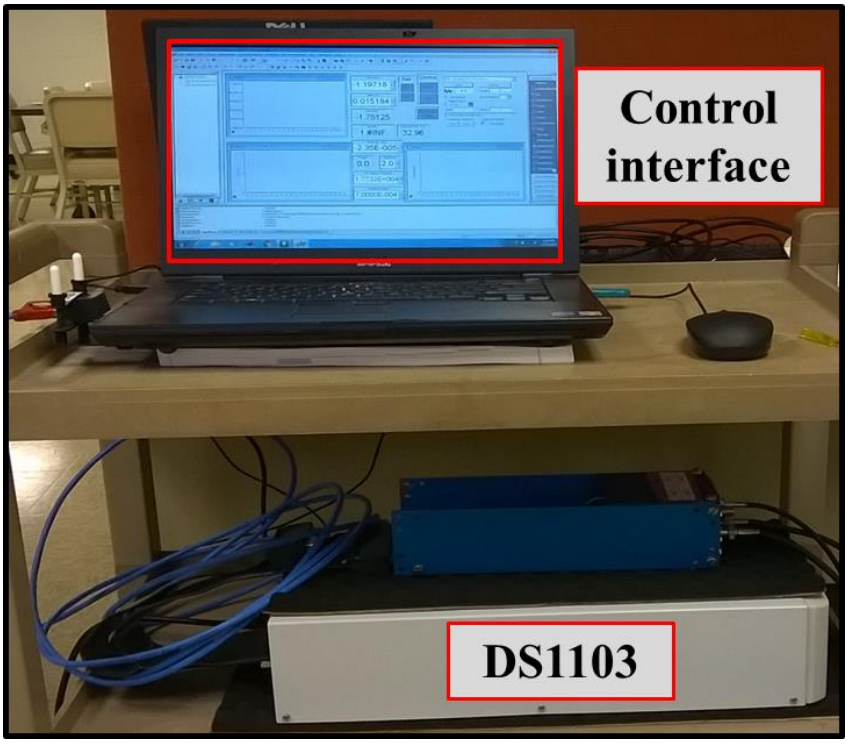

Figure 4.3. Digital control unit and software interface.

Details of the physical parameters associated with the beam and the piezoelectric patches are provided in Appendix B. Substituting the numerical values in the corresponding expressions (presented in Appendix A), the modal parameters for the mechanical system are obtained as $m_{11} = 0.1622$ kg, $k_{11} = 7205$ N/m. The modal damping ratio is calculated as $\zeta = 0.006$, using impact hammer tests. Accordingly, the damping coefficient is $c_{11} = 0.4136$ Ns/m.

The parameters k_{em1}, k_{ic}, associated with the piezoelectric patches, can be calculated using the analytical expressions under Appendix A. However a common (and more reliable) practice is to use experimentally measured values. This is mainly done to avoid inconsistencies in piezoelectric material properties, as well as the occurrence of imperfect bonding between the patches and the beam. The cross-coupling coefficient k_{em1} is determined by measuring the variation in the beam's natural frequency when the PZT electrodes are shorted (Tang and Wang,

2001). The inverse capacitive coefficient k_{ic} is obtained by simply measuring the capacitance of the PZT patch with a multi-meter. For the present experiment, these parameters are determined as $k_{em1} = 74342$ and $k_{ic} = 1.211\times10^{8}\ \mathrm{F}^{-1}$.

4.1.2. The shunt circuit and associated issues

The shunt circuit components play a vital role for a successful DR implementation. In the parametric design stage, it was observed that an arbitrary selection of resistor (R) and inductor (L) values yields not-so-desirable DR operation. For instance, the DR control parameters as calculated in (3.8) could be very close to the combined system's stability bounds [as in (1.5) with (3.9)]. That is, tuning the shunt circuit for resonance may also force the combined dynamics to be at the verge of instability. The problem described here is associated to a disparity in natural frequencies of the two coupled structures (the beam and shunt circuit). Let us define $\omega_b = \sqrt{k_{11}/m_{11}}$ and $\omega_c = \sqrt{k_{ic}/L}$ as the beam's and circuit's undamped natural frequencies, respectively. When the circuit frequency, ω_c, is not within proximity of ω_b, an excessive control action is required to bring the circuit to resonate at ω_c. Such aggressive control effort, in turn, may render instability in the combined system dynamics. However if $\omega_c \approx \omega_b$, the circuit can be tuned with DR parameters, while the coupled dynamics remains stable with a safe margin. This observation, in fact, agrees with earlier findings in shunt damping literature. For instance Tang and Wang (2001) derive the following R-L values for passive shunt circuits, using an analogous approach to Den Hartog's (1956) vibration absorber design guidelines.

$$L = \frac{k_{ic}}{\omega_b^2}, \qquad R = \frac{k_{em1}}{\omega_b}\sqrt{\frac{2k_{ic}}{k_{11}}} \tag{4.1}$$

As seen from (4.1), this approach also requires that the circuit and beam have matching natural frequencies. In the present setup, the beam's natural frequency is $\omega_b = 33.54$ Hz. Then for the circuit frequency to match that, an inductance value of $L = 2726$ H is required. This is, by any measure, an excessive amount, noting that 10 H inductance is typically considered as a high value for currently available off-the-shelf passive inductors. This difficulty is a well-known problem and has been widely reported in the literature. For instance, Hagood and von Flotow (1991) mention a solution that, an unusually bulky and costly passive inductor was used in their experiments. Alternatively, synthetic inductor circuits can also be used to remedy the problem, as in Hagood and Crawley (1991) or Agnes (1995). The use of negative capacitance circuits has also been proven effective in such cases (Tang and Wang, 2001; De Marneffe and Preumont, 2008).

For the experiment in the present work, we apply a method proposed by Fleming et al. (2003) to reduce the inductance requirement. The idea is rather simple in nature; to add a passive capacitor parallel to the piezoelectric patch between points A and B in Figure 3.3. This configuration is depicted in Figure 4.4, along with a simpler equivalent representation. Here, C_P and C_{ad} are the piezoelectric and added capacitance, respectively. $C_T = C_P + C_{ad}$ and $\beta = C_P / C_T < 1$. $V_P = k_{em} u_1$ is the voltage generated by the piezoelectric effect which remains fixed for the same strain level. Then noting that $k_{ic} = 1 / C_P$, the voltage across A-B becomes

$$V_{AB} = \beta k_{em1} u_1 + \beta k_{ic} Q . \tag{4.2}$$

As a result, the effect of parameters k_{em1} and k_{ic} in the circuit appear as βk_{em1} and βk_{ic}. Then, as per (4.1), the inductance requirement is reduced proportionally for the same frequency ω_b. The effect of the added capacitor should also be taken into account in the remainder of the system

model. For instance in (3.8) and (3.9), the parameters k_{em1} and k_{ic} should be replaced with βk_{em1} and βk_{ic}.

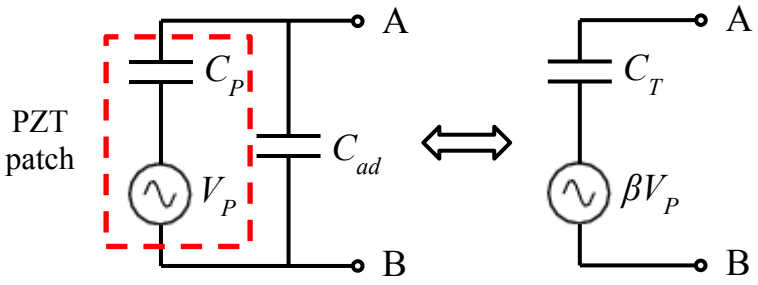

Figure 4.4. Addition of a capacitor in parallel to the piezoelectric element (A and B correspond to the same nodes seen in Figure 3.3).

The piezoelectric capacitance used in these experiments is C_P = 8.9 nF. Adding a C_{ad} = 9.8 nF capacitor in parallel, β = 0.48 makes it possible to use a smaller inductor of 1297 H instead of the initially required 2726 H. To achieve this inductance (which is still high), a synthetic inductor circuit with four operational amplifiers is employed (Agnes, 1995; Chen, 1986). Using (4.1), one obtains the new resistance requirement as R = 21.51 kΩ as opposed to the initial R = 64.67 kΩ. In the experiment, an existing 27 kΩ resistor is used, producing a satisfactory performance.

Another challenge is the presence of a parasitic resistance in addition to the lumped resistor element in the circuit. This is most likely induced by the synthetic inductor circuit, which is an ensemble of four op-amps, six resistors and two capacitors. Agnes (1995) uses the same op-amp circuit, and reports that the leakage in capacitors causes some additional resistive behavior. Accordingly, in Figure 3.3, we define $R = R_1 + R_p$, where R_1 is the passive resistor element and R_p is the parasitic resistance. Using open-loop measurements, it is determined that during steady-state conditions, $R_p \approx 4.67$ kΩ, yielding R = 31.67 kΩ. This parasitic resistance effect has to be

taken into account for accurately calculating the control parameters. Notice that the voltage drop across the lumped resistor element is used for the delayed feedback control. The presence of this parasitic resistance, however, directly affects the feedback gain as per (3.8). The corrected gain selection should be expressed as

$$g(\omega) = \frac{(-1)^{l-1}}{R_1 \omega} \sqrt{(R\omega)^2 + (k_{ic} - L\omega^2)^2} \tag{4.3}$$

The combined system's stability boundaries g_{cs} and τ_{cs} are also influenced by this phenomenon. Hence $B(s)$ in (3.9) should be corrected as

$$B(s) = -R_1 s(m_{11}s^2 + c_{11}s + k_{11}) \tag{4.4}$$

4.1.3. Control parameter correction scheme

The experimental setup involves numerous uncertainties; more pronounced ones being among the circuit parameters, as expressed earlier. These uncertainties are mainly due to the measuring instruments themselves. Consider the inverse capacitance coefficient k_{ic}, for instance. It is obtained by simply inverting the capacitance measurement of the piezoelectric plate bonded on the beam. This capacitance, in turn, is currently measured with a precision of two decimal points and is in the order of nanofarads. When inverted, it results in large variations in the value of k_{ic}, which gravely affects the much needed accuracy in the control parameters (τ, g). On the other hand, successful DR implementation is highly dependent on the precision of these parameters. One should remember that the control law aims to induce pure resonance in the shunt circuit and any deviation from this condition results in inadequate vibration suppression performance. Similar uncertainties exist in the inductance L. The passive resistor and capacitor elements used in the synthetic inductor circuit involve a certain tolerance within their fixed

values. Similarly, the op-amps introduce several deficiencies, such as non-zero input current and finite input impedance. Furthermore, it is also observed that these uncertainties are not fixed and they vary during the operation, most probably as a result of changes in operating temperature.

In order to insure consistent accuracy in control parameters, an output measurement-based correction scheme is developed following similar adaptation methods, proposed earlier in DR literature such as Renzulli et al. (1999) and Hosek and Olgac (2002). An important distinction here is that the controller parameters are updated using open-loop measurements (i.e., when control action is turned off), as we explain next.

The DR tuning parameters g and τ as in (3.8) are essentially derived by solving the magnitude and phase conditions of (3.7). That is

$$g(\omega) = (-1)^{l-1}\left|\frac{k_{ic} - L\omega^2 + R\omega \mathrm{i}}{R_1 \omega \mathrm{i}}\right|,$$

$$\tau(\omega) = \frac{1}{\omega}\left[-\arg\left(\frac{k_{ic} - L\omega^2 + R\omega \mathrm{i}}{R_1 \omega \mathrm{i}}\right) + (l-1)\pi\right], \quad l = 1, 2, \ldots \tag{4.5}$$

Notice that the beam tip displacement w_t and voltage across the lumped resistor V_{R1} are both monitored in real time through the available sensors (fiber-optic displacement sensor and differential amplifier, respectively). For the uncontrolled system (g = 0), consider the transfer function between these two signals, derived from (3.5), as follows.

$$\frac{w_t(s)}{V_{R1}(s)} = \frac{\phi_t u_1(s)}{R_1 s Q(s)} = \frac{\phi_t (Ls^2 + Rs + k_{ic})}{-k_{em1} R_1 s} \tag{4.6}$$

Here, $\phi_t = \phi_1(x_t)$ is the value of the first-mode shape function at the beam tip $x = x_t$ where the displacement sensor is positioned. Defining

$$\kappa = k_{em1} / \phi_t \tag{4.7}$$

and substituting $s = \omega \mathrm{i}$ in (4.6), the frequency response function (FRF) becomes

$$\frac{w_t(\omega)}{V_{R1}(\omega)} = H(\omega) = \frac{k_{ic} - L\omega^2 + R\omega \mathrm{i}}{-\kappa R_1 \omega \mathrm{i}} \tag{4.8}$$

For the uncontrolled system, using a snapshot of time traces of $w_t(t)$ and $V_{R1}(t)$ generated by the appropriate sensors, this FRF at a particular frequency ω_0 can be obtained. It is typically a complex number, and its detection can be repeated periodically as explained later on. Let us denote the measured complex quantity as

$$H^*(\omega_0) = w_t(\omega_0) / V_{R1}(\omega_0) . \tag{4.9}$$

The parameter κ in (4.7) is produced with sufficient accuracy, because k_{em1} is obtained from reliable experimental measurements and the well-known shape function $\phi_1(x_t)$ is analytically available (see Appendix A). The characteristics associated with the piezoelectric material (e.g., k_{em1}) are assumed invariant over time, in contrast to the circuit parameters. With κ known, and $H^*(\omega)$ measured as in (4.9), equation (4.8) can now be used to solve

$$\left. \frac{k_{ic} - L\omega^2 + R\omega \mathrm{i}}{R_1 \omega \mathrm{i}} \right|_{\omega=\omega_0} \cong -\kappa H^*(\omega_0) . \tag{4.10}$$

Notice that the left-hand side of this equation (4.10) appears identically in (4.5). Its substitution will render

$$g = (-1)^{l-1}\kappa\left|H^*(\omega_0)\right|, \quad \tau = \frac{1}{\omega_0}\left[-\angle H^*(\omega_0) + (l-1)\pi\right], \quad l = 1,2,... \tag{4.11}$$

Now the main sources of uncertainties are all contained within the actually measured FRF value, $H^*(\omega_0)$, instead of the components L and R. By calculating the control gain and delay with this FRF measurement as in (4.11), the uncertainties are automatically accounted for and need not be determined individually. Notice that this adaptation procedure is an intermittent operation, because it needs the measurements over the uncontrolled system. Therefore the conceived real time control is interrupted just to achieve the parameter adaptation updates at appropriately selected periods. The next subsection contains an example of this for clarity.

4.1.4. Analysis of sample test run

For the dynamic model at hand, we display the DR tuning parameters as expressed in (4.5) and the corresponding combined system stability boundaries [(1.5) with (3.9)], both on Figure 4.5. Here, blue and green curves are used to distinguish positive and negative control gains, respectively; while red curves are the combined system's stability boundaries. Stable operating zones are shaded in gray. The zoomed window shows the minimum and maximum frequencies on the particular branch for stable deployment of the DR tuning. The limits of the operating frequency range for this experiment are obtained as $\omega_{min} = 31.89$ Hz and $\omega_{max} = 35.49$ Hz. They are located where DR tuning parameters intersect the combined system stability boundaries. A test is conducted on the experimental setup, to verify these findings. The beam is excited through the secondary piezoelectric patch with a 33 Hz single harmonic signal. The DR tuning parameters corresponding to this frequency are calculated from equation (4.5) on the first negative-gain branch as $g = -1.174$ and $\tau = 0.0151$ s (marked on the zoomed-in window in Figure 4.5).

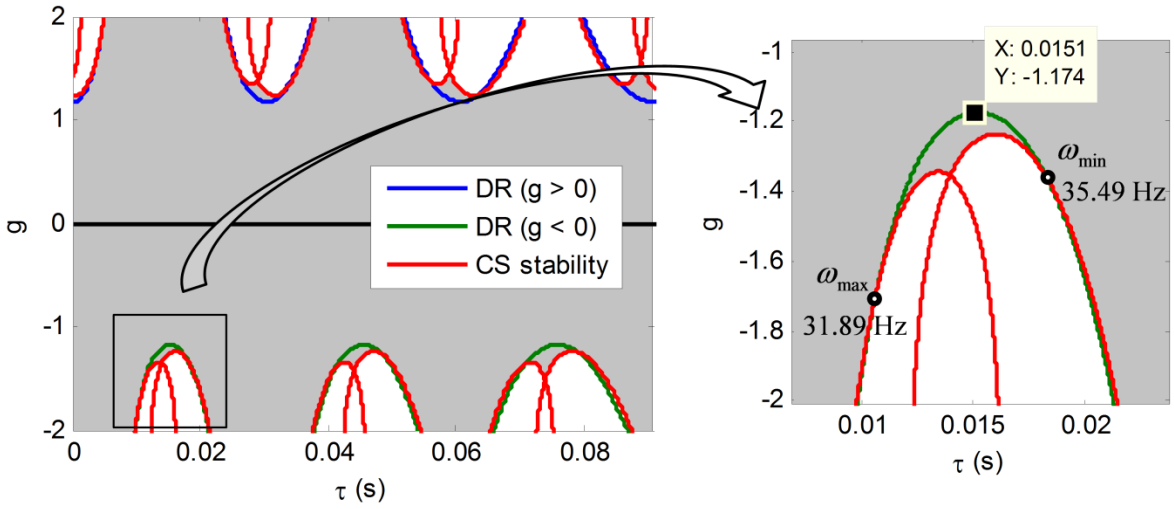

Figure 4.5. DR tuning parameters and combined system (CS) stability boundaries in (τ, g) space. Zoomed view of operating branch and frequency limits are also depicted.

The digital control unit (dSPACE DS1103) is set at a sampling rate of 4000 Hz. The data acquisition and feedback control actions are executed at this primary sampling frequency. The control parameter correction scheme of (4.11) runs at a slower secondary rate, with a period of 4 seconds. For this scheme, the frequency domain data of the beam tip displacement $w_t(\omega_0)$, and the resistor voltage $V_{R1}(\omega_0)$ are required. Their time domain signals $w_t(t)$ and $V_{R1}(t)$ are stored during 4 second blocks. Then a Fast Fourier Transform (FFT) is applied and the buffered signals are converted to frequency domain. The dominant frequency content is automatically sensed as ω_0, which is the excitation frequency. The complex frequency domain values [$w_t(\omega_0)$ and $V_{R1}(\omega_0)$] corresponding to ω_0 are extracted and $H^*(\omega_0)$ is calculated as defined in (4.9). With ω_0 and $H^*(\omega_0)$ known, the feedback control parameters, the gain and the delay are updated as per (4.11).

Time traces from a test run are presented in Figure 4.6. The experiment starts with no excitation on the beam. At the time instant t_1, the harmonic forcing is turned on and the beam

starts to oscillate. At this point the feedback control is not yet activated. Because of the piezoelectric coupling, the shunt circuit performs some passive vibration absorption, also seen from the voltage fluctuation across the resistor. During this phase, the parameter correction scheme is executed, yielding the updated feedback parameters $g = -1.154$, $\tau = 0.0153$ s as per (4.11). At t_2, the controller is turned on and decay is observed approximately until t_3. After t_3, residual oscillations are measured with noise contamination.

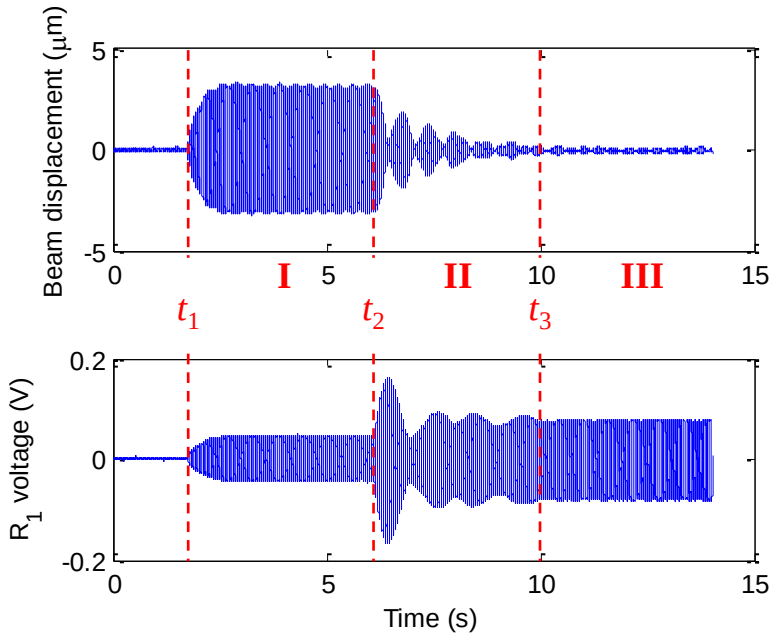

Figure 4.6. Time traces of beam tip deflection $w_t(t)$ and voltage across lumped resistor $V_{R1}(t)$ during test run.

The three distinct phases; steady excitation, closed-loop transient and steady-state residual oscillations are marked on Figure 4.6 with intervals I, II and III, respectively. The length-normalized amplitude spectra of the beam response during these intervals are presented in Figure 4.7. FFTs during each interval are calculated and scaled using the signal length that produced them.

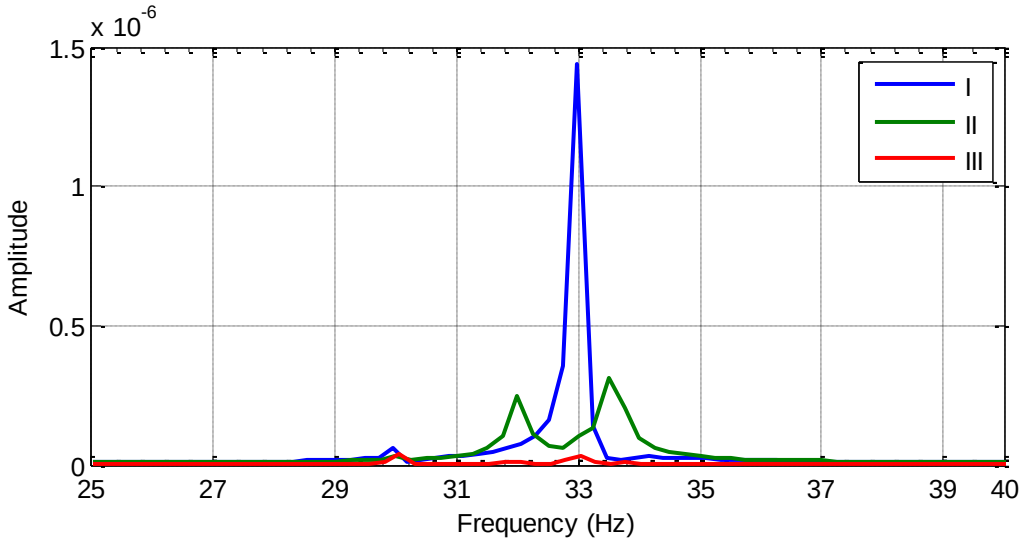

Figure 4.7. Amplitude spectra of beam tip displacement during intervals I, II and III as designated on Figure 4.6.

We next examine the system response during these three intervals in greater detail.

i) During interval I, the beam is oscillating steadily under the external excitation at a frequency of 33 Hz, which is clearly pronounced in the spectrum of the signal (blue in Figure 4.7).

ii) In the transient phase (II), a *beating* phenomenon is observed during the decay. This implies that the coupled dynamics exhibit two pairs of dominant roots with similar imaginary parts (i.e., frequency). This is corroborated by the amplitude spectrum. Notice how the control action cancels the dominant frequency and splits it into approximately 32 and 34 Hz components (green in Figure 4.7). The resulting two frequencies are in close vicinity and are thus responsible for the beating observed in time domain (Figure 4.6). Another observation is that the settling time is relatively long (about 4 seconds). This can be explained by noting that the control parameters are close to the combined system stability boundary (see

Figure 4.5). As a result, the dominant characteristic roots are expected to be close to the imaginary axis, with small negative real parts.

iii) During interval III, vibration in the beam is eliminated almost completely. In time domain (Figure 4.6), the residual oscillation level is slightly higher than inherent/ambient noise in displacement measurement (prior to interval I). Accordingly, in frequency domain the amplitude of the signal (red in Figure 4.7) is dwarfed compared to the previous two intervals. Also note that the electrical current in the circuit increases, as it is brought to resonance and is now absorbing almost all of the vibration.

The experimental observations regarding the system's transient behavior can also be compared to numerical results derived from the mathematical model. For this, the roots of the combined system's characteristic equation (3.9) are solved within a certain tolerance using a computational routine, called Quasi-Polynomial mapping based Rootfinder (QPmR) (Vyhlídal and Zitek, 2009). Substituting the control parameter values into the characteristic equation, the roots within a finite region in the complex plane are calculated. For the present configuration, a set of two dominant conjugate roots among the infinite spectrum of the quasi-polynomial (3.9) appear, as depicted in Figure 4.8. The imaginary parts of these roots correspond to free oscillations at frequencies of 32 Hz and 34.5 Hz. These frequencies are similar to the ones seen in the amplitude spectrum (Figure 4.7), albeit with slight deviations. The 5% settling times for these two modes are approximately 7.6 and 4.9 seconds, respectively. Although it is difficult to assess settling time from Figure 4.6 due to the residual oscillations, it is comparable to the numerically predicted values.

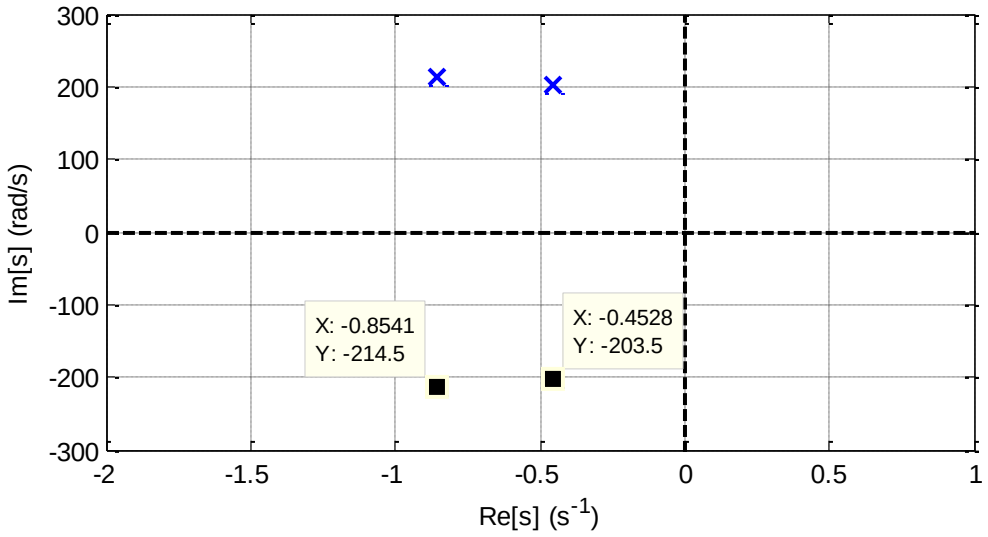

Figure 4.8. Approximate dominant characteristic roots of the combined system when feedback control is activated.

4.2. Experiments on Energy Harvesting Capacity in Piezoelectric Networks

4.2.1. Modifications to experimental setup

The experimental setup was modified in order to provide a more suitable environment for energy harvesting focused studies. The main difference is the beam and the PZT patches attached to it. During the numerical case study under Section 3.5, it was observed that energy harvesting capacity in the piezoelectric shunt circuit was significantly enhanced at frequencies away from the system's resonant peak. This means that tests need to be conducted at such frequencies in order to obtain meaningful results. However the steel beam used during DR experiments has very high stiffness and reacts minimally to frequencies that are not close enough to its resonant modes. As a result, it becomes difficult to monitor displacement and current in the circuit as these quantities are very small at non-resonant frequencies. As a remedy, a different beam structure with higher compliance (i.e., less stiffness) should be used for energy harvesting related

experiments. A general increase in system response amplitude, both in the beam displacement and the shunt circuit current, is crucial to obtain clear measurements and meaningful experimental data.

The steel beam used in the DR experiments (0.279 m length, 3 mm × 25 mm profile) is replaced with a considerably thinner and more flexible aluminum beam (0.2 m length, 0.75 mm × 20 mm profile). The PZT patches to be used with the new beam are also thinner and made of a different material (Steiner & Martins SM311). This new construct, depicted in Figure 4.9, offers several advantages.

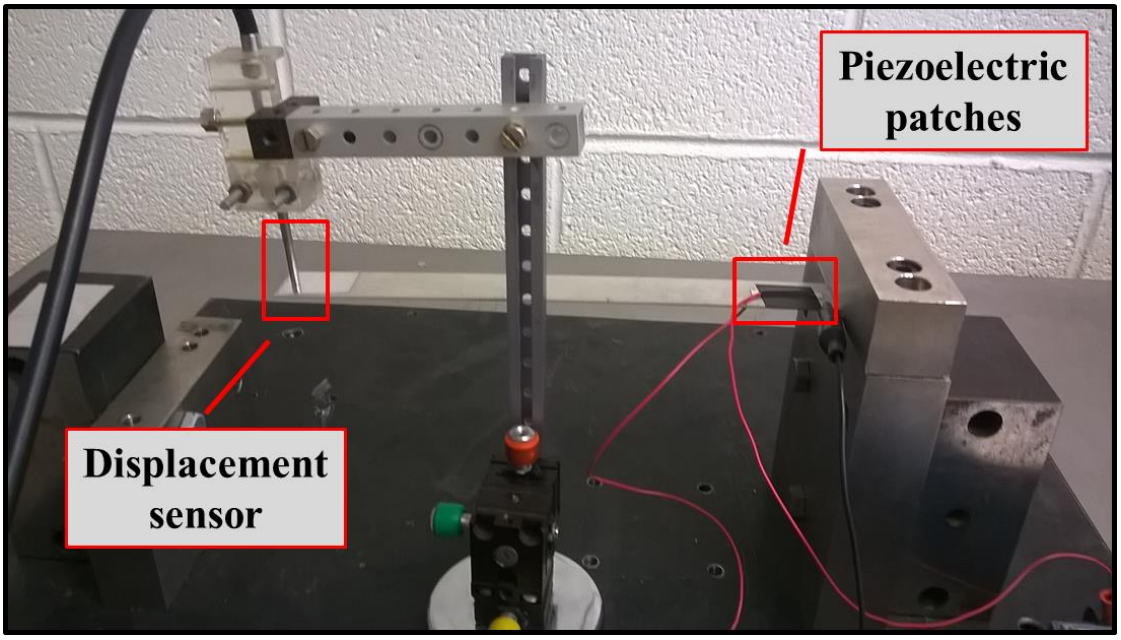

Figure 4.9. Aluminium beam with thin profile and new PZT patches.

First of all, the increased flexibility and compliance in the beam results in higher displacement, especially at frequencies away from resonant modes. Another important feature is that this new setup is designed such that the first two resonant modes are available within the $10 - 100$ Hz frequency range. More specifically, the second resonant mode carries an analytically calculated

frequency of about 98 Hz and is chosen to be the main resonant peak to work around. That is, the operating frequencies for experimental tests are chosen within the neighborhood of this second mode and accordingly, the shunt circuit is designed around it. The fact that the shunt circuit is tuned to a mode at higher frequency offers the important benefit of reducing the required inductance, as seen from (4.1).

The experimental work conducted on energy harvesting capacity differs from DR-based vibration suppression efforts in certain ways. For ideal and correct vibration absorption performance, the main requirement is to bring the shunt circuit sub-structure to resonance at the frequency of harmonic excitation. As long as this is achieved, deficiencies in modeling of the beam structure and its response do not affect the outcome. This fact is apparent from (3.6), where the numerator is set to zero if the circuit is exhibiting resonance, regardless from the beam's own dynamics. For this reason, the level of rigor in modeling beam dynamics does not directly affect DR-based vibration suppression performance, but it rather influences other important concerns, such as combined system stability (discussed under Section 3.6). Regarding energy harvesting capacity, the beam dynamics play a more important role in assessing performance. The amplitude of the shunt circuit current is of vital importance, as seen in equations (3.13) and (3.16); the current amplitude, in turn, is directly affected by the beam dynamics as seen from the denominator of (3.19). As a result, increasing the fidelity in beam modeling will yield more accurate results during the investigation of energy harvesting performance.

4.2.2. System dynamics with dual mode beam model

Following the remarks on the importance of beam modeling and the fact that experiments with the new structure are to be conducted around the second mode, it becomes apparent that a

dual mode model for the beam is required. So far, the first mode was considered only [see (3.1)], which resulted in satisfactory performance for vibration control purposes. For the work involving this modified setup, we shall use the following modal truncation for the beam's dynamics.

$$w(x,t) = \phi_1(x)u_1(t) + \phi_2(x)u_2(t) \tag{4.12}$$

Here, where ϕ again represent the shape functions corresponding to the beam's transverse vibratory modes, and u denote the corresponding temporal dynamics. Hamilton's principle can again be used to obtain governing differential equations in a similar form to (3.2).

$$m_{11}\ddot{u}_1 + c_{11}\dot{u}_1 + k_{11}u_1 + c_{12}\dot{u}_2 + k_{12}u_2 + k_{em1}Q_s = F_{m1}$$

$$m_{22}\ddot{u}_2 + c_{22}\dot{u}_2 + k_{22}u_2 + c_{12}\dot{u}_1 + k_{12}u_1 + k_{em2}Q_s = F_{m2}$$

$$L\ddot{Q}_s + R\dot{Q}_s + k_{ic}Q_s + k_{em1}u_1 + k_{em2}u_2 = V_c \tag{4.13}$$

Here, m_{11} and m_{22} are modal masses; c_{11} and c_{22} are modal damping coefficients; k_{11} and k_{22} are modal stiffness coefficients; k_{em1} and k_{em2} are electro-mechanical coupling coefficients; F_{m1} and F_{m2} are modal mechanical forces; associated with the first and second modes, respectively. Note that the beam modes are coupled through damping c_{12} and stiffness k_{12}. Q_s, V_c are the electrical charge and control voltage in the shunt circuit, while k_{ic} denotes the inverse capacitance coefficient as defined earlier under Section 3.2. Detailed expressions for these parameters are presented under Appendix A.

The relations in (4.13) are for the general case where the beam is subject to mechanical forcing and there is no control action in the shunt circuit. In order to obtain an accurate input-output relationship, the exact nature of the external disturbance mechanism needs to be included

in the model. Notice that in these experiments, the external forcing/disturbance is implemented using one of the two symmetrical PZT patches, which is driven by a voltage source. There is no separate mechanical forcing on the beam, hence $F_{m1} = F_{m2} = 0$. Instead, let us define Q_{ex} as the electrical charge going through the PZT patch which is used to excite the beam. As the two PZT patches are identical and mounted symmetrically on opposite faces of the beam, the electro-mechanical coupling and inverse capacitance coefficients are assumed to be the same. That is, for the driving PZT, these coefficients are also taken as k_{em1}, k_{em2} and k_{ic}. Then the modal governing equations for the beam can be revised as follows.

$$m_{11}\ddot{u}_1 + c_{11}\dot{u}_1 + k_{11}u_1 + c_{12}\dot{u}_2 + k_{12}u_2 + k_{em1}Q_s + k_{em1}Q_{ex} = 0$$

$$m_{22}\ddot{u}_2 + c_{22}\dot{u}_2 + k_{22}u_2 + c_{12}\dot{u}_1 + k_{12}u_1 + k_{em2}Q_s + k_{em2}Q_{ex} = 0 \qquad (4.14)$$

Now notice that the circuit driving the forcing PZT patch does not contain any *R*-*L* elements. Instead, it simply consists of a voltage source (power amplifier) connected to the PZT patch. Then the governing equation for the driving circuit can be expressed as follows.

$$k_{ic}Q_{ex} + k_{em1}u_1 + k_{em2}u_2 = V_{ex} \qquad (4.15)$$

Here, V_{ex} is the excitation voltage used to drive the PZT. Because this is a scalar equation, the excitation charge can simply be solved as

$$Q_{ex} = \frac{V_{ex}}{k_{ic}} - \frac{k_{em1}}{k_{ic}}u_1 - \frac{k_{em2}}{k_{ic}}u_2 . \qquad (4.16)$$

Then substituting (4.16) in (4.14) and incorporating the feedback control logic $V_c = gR_1\dot{Q}_s(t-\tau)$ [see (3.4)], the governing equations are re-written as follows.

$$m_{11}\ddot{u}_1 + c_{11}\dot{u}_1 + (k_{11} - k_{em1}^2 / k_{ic})u_1 + c_{12}\dot{u}_2 + (k_{12} - k_{em1}k_{em2} / k_{ic})u_2 + k_{em1}Q_s = -\frac{k_{em1}}{k_{ic}}V_{ex}$$

$$m_{22}\ddot{u}_2 + c_{22}\dot{u}_2 + (k_{22} - k_{em2}^2 / k_{ic})u_2 + c_{12}\dot{u}_1 + (k_{12} - k_{em1}k_{em2} / k_{ic})u_1 + k_{em2}Q_s = -\frac{k_{em2}}{k_{ic}}V_{ex}$$

$$L\ddot{Q}_s + R\dot{Q}_s + k_{ic}Q_s + k_{em1}u_1 + k_{em2}u_2 - gR_1\dot{Q}_s(t-\tau) = 0 \tag{4.17}$$

The system dynamics seen in (4.17) are re-cast into a state-space form next. This offers a systematic and convenient representation for the analyses that follow. Let us define the state vector as follows.

$$\mathbf{x}(t) = \begin{bmatrix} u_1(t) & u_2(t) & \dot{u}_1(t) & \dot{u}_2(t) & Q_s(t) & \dot{Q}_s(t) \end{bmatrix}^T \tag{4.18}$$

The input to the system is defined as the excitation voltage:

$$v(t) = V_{ex}(t) \tag{4.19}$$

The output vector consists of the beam tip displacement w_t and shunt circuit current $i_s = \dot{Q}_s$

$$\mathbf{y}(t) = \begin{pmatrix} w_t(t) \\ i_s(t) \end{pmatrix} \tag{4.20}$$

where the beam tip displacement is expressed as

$$w_t(t) = \phi_1(x_t)u_1(t) + \phi_2(x_t)u_2(t) \tag{4.21}$$

and x_t is the coordinate along the beam axis where the displacement sensor is located.

Then the governing equations can be represented in state-space form as

$$\dot{\mathbf{x}}(t) = \mathbf{A_1}\mathbf{x}(t) + \mathbf{A_2}\mathbf{x}(t-\tau) + \mathbf{B}v(t), \qquad \mathbf{y}(t) = \mathbf{C}\mathbf{x}(t) \tag{4.22}$$

where

$$\mathbf{A_1} = \begin{bmatrix} 0 & 0 & 1 & 0 & 0 & 0 \\ 0 & 0 & 0 & 1 & 0 & 0 \\ (k_{em1}^2 / k_{ic} - k_{11})/m_{11} & (k_{em1}k_{em2}/k_{ic} - k_{12})/m_{11} & -c_{11}/m_{11} & -c_{12}/m_{11} & -k_{em1}/m_{11} & 0 \\ (k_{em1}k_{em2}/k_{ic} - k_{12})/m_{22} & (k_{em2}^2/k_{ic} - k_{22})/m_{22} & -c_{12}/m_{22} & -c_{22}/m_{22} & -k_{em2}/m_{22} & 0 \\ 0 & 0 & 0 & 0 & 0 & 1 \\ -k_{em1}/L & -k_{em2}/L & 0 & 0 & -k_{ic}/L & -R/L \end{bmatrix}$$

$$\mathbf{A}_2 = \begin{bmatrix} 0 & 0 & 0 & 0 & 0 & 0 \\ 0 & 0 & 0 & 0 & 0 & 0 \\ 0 & 0 & 0 & 0 & 0 & 0 \\ 0 & 0 & 0 & 0 & 0 & 0 \\ 0 & 0 & 0 & 0 & 0 & 0 \\ 0 & 0 & 0 & 0 & 0 & gR_1/L \end{bmatrix}, \qquad \mathbf{B} = \begin{bmatrix} 0 \\ 0 \\ -k_{em1}/(k_{ic}m_{11}) \\ -k_{em2}/(k_{ic}m_{22}) \\ 0 \\ 0 \end{bmatrix},$$

$$\mathbf{C} = \begin{bmatrix} \phi_1(x_t) & \phi_2(x_t) & 0 & 0 & 0 & 0 \\ 0 & 0 & 0 & 0 & 0 & 1 \end{bmatrix} \tag{4.23}$$

Applying Laplace transformation on (4.22), the input-output relation can be described as follows.

$$\mathbf{Y}(s) = \mathbf{C}(s\mathbf{I} - \mathbf{A_1} - \mathbf{A_2}\,\mathrm{e}^{-\tau s})^{-1}\mathbf{B}V(s) \tag{4.24}$$

The transfer matrix containing transfer function for both outputs is also apparent from this form, and it is defined as follows.

$$\mathbf{G}(s) = \begin{pmatrix} \dfrac{w_t(s)}{V_{ex}(s)} \\ \\ \dfrac{i_s(s)}{V_{ex}(s)} \end{pmatrix} = \mathbf{C}(s\mathbf{I} - \mathbf{A_1} - \mathbf{A_2}\,\mathrm{e}^{-\tau s})^{-1}\mathbf{B} \tag{4.25}$$

The transfer matrix seen in (4.25) can be constructed by using symbolic matrix algebra in MATLAB. This way the transfer functions describing both the beam tip displacement and shunt circuit current with respect to input excitation voltage can be obtained conveniently. Also notice that the combined system's characteristic equation is easy to derive from the state space representation:

$$CE_{cs}(s,\tau,g) = \det\left|s\mathbf{I} - \mathbf{A_1} - \mathbf{A_2}\,\mathrm{e}^{-\tau s}\right| = 0 \tag{4.26}$$

As seen from (4.23), rank($\mathbf{A}_2$) = 1, and as a result the characteristic equation (4.26) only contains one instance of the delay-induced exponential term. Hence, the characteristic equation can again be represented in the form of (1.4) and the expressions in (1.5) can be used to calculate the combined system stability boundaries.

4.2.3. Analytical and experimental work on the setup

The physical properties of the experimental setup are provided under Appendix B. Substituting this data in the expressions under Appendix A, the modal parameters corresponding to this configuration are obtained. As mentioned earlier, the inductance and resistance of the shunt circuit are designed according to the second resonant mode of the beam which is around 98 Hz. The shunt circuit parameters corresponding to this configuration are calculated using the relations in (4.1), and are obtained as R_1 = 12 kΩ, L = 167 H. Notice that the inductance value is much smaller compared to the required amount for the previous setup. However this value is still too high for off-the-shelf passive inductors and as a result the synthetic inductor circuit is used with modified components to generate the necessary inductance. The parasitic resistance is measured to be R_p = 160 Ω. In order to reduce redundancy, the numerical values of individual

parameters (e.g., m_{11}, k_{11}, c_{12},…) are not listed. Instead, the resulting system description is provided in the form of the state-space matrices defined in (4.23).

$$\mathbf{A_1} = \begin{bmatrix} 0 & 0 & 1 & 0 & 0 & 0 \\ 0 & 0 & 0 & 1 & 0 & 0 \\ -10555 & -6402 & -7322 & 1.644\times10^{-5} & 433550 & 0 \\ -6396 & -387880 & 1.644\times10^{-5} & -7.315 & 1917700 & 0 \\ 0 & 0 & 0 & 0 & 0 & 1 \\ 21.02 & 93.07 & 0 & 0 & -404660 & -72.81 \end{bmatrix},$$

$$\mathbf{A}_2 = \begin{bmatrix} 0 & 0 & 0 & 0 & 0 & 0 \\ 0 & 0 & 0 & 0 & 0 & 0 \\ 0 & 0 & 0 & 0 & 0 & 0 \\ 0 & 0 & 0 & 0 & 0 & 0 \\ 0 & 0 & 0 & 0 & 0 & 0 \\ 0 & 0 & 0 & 0 & 0 & 71.86g \end{bmatrix}, \quad \mathbf{B} = \begin{bmatrix} 0 \\ 0 \\ 6.415\times10^{-3} \\ 2.837\times10^{-2} \\ 0 \\ 0 \end{bmatrix},$$

$$\mathbf{C} = \begin{bmatrix} 1.931 & -1.761 & 0 & 0 & 0 & 0 \\ 0 & 0 & 0 & 0 & 0 & 1 \end{bmatrix} \tag{4.27}$$

Substituting these in (4.25), the transfer functions for the two system outputs, beam tip displacement and shunt circuit current, with respect to the excitation voltage are obtained as follows.

$$\frac{w_t(s)}{V_{ex}(s)} = \frac{\begin{array}{c} 4.033\times10^{61}s^4 + 3.232\times10^{63}s^3 + 1.205\times10^{67}s^2 - 1.931\times10^{68}s \\ -1.737\times10^{72} + g\,\mathrm{e}^{-\tau s}(2.898\times10^{63}s^3 + 2.123\times10^{64}s^2 - 3.085\times10^{68}s) \end{array}}{CE_{cs}(s,\tau,g)},$$

$$\frac{i_s(s)}{V_{ex}(s)} = \frac{1.084\times10^{52}s^3 + 7.935\times10^{52}s^2 + 2.832\times10^{56}s}{CE_{cs}(s,\tau,g)} \tag{4.28}$$

and the system's characteristic equation [i.e., the common denominator of the transfer functions in (4.28)] is

$$\begin{aligned} CE_{cs}(s,\tau,g) &= 3.905\times10^{51}s^6 + 3.415\times10^{53}s^5 + 3.140\times10^{57}s^4 + 1.478\times10^{59}s^3 \\ &+ 6.455\times10^{62}s^2 + 5.755\times10^{63}s + 6.381\times10^{66} - g\,\mathrm{e}^{-\tau s}(2.806\times10^{53}s^5 + 4.107\times10^{54}s^4 \\ &+ 1.118\times10^{59}s^3 + 8.185\times10^{59}s^2 + 1.137\times10^{63}s) = 0 \end{aligned} \qquad (4.29)$$

The system characteristics without any active control action can be obtained by substituting $g = 0$ in (4.28) and (4.29). The resulting open-loop dynamics are depicted in the Bode magnitude plots presented in Figure 4.10.

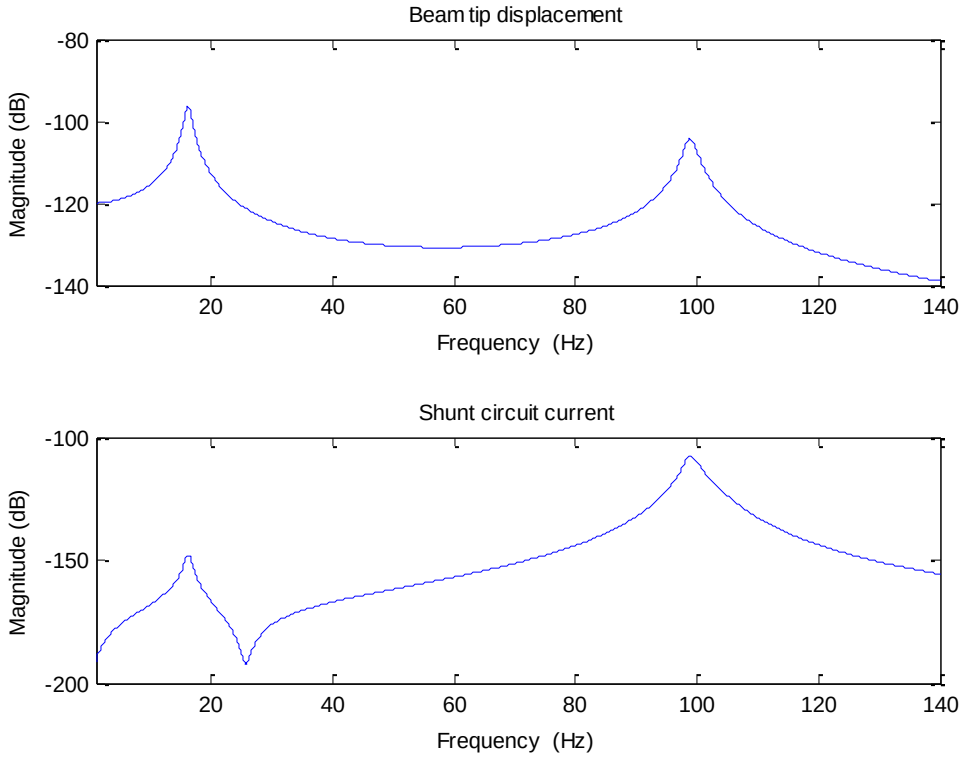

Figure 4.10. Bode magnitude plots for open loop transfer functions of beam tip displacement and shunt circuit current.

The first two resonant modes of the beam are clearly observed here. As it was mentioned under Section 4.2.1, in this setup we focus on the second resonant mode that occurs around 98 Hz. The inductance and resistance of the shunt circuit are designed according to this frequency using the relations in (4.1). This is also apparent from the fact that the second resonant peak of the shunt circuit current has higher amplitude than the first one, as seen from Figure 4.10.

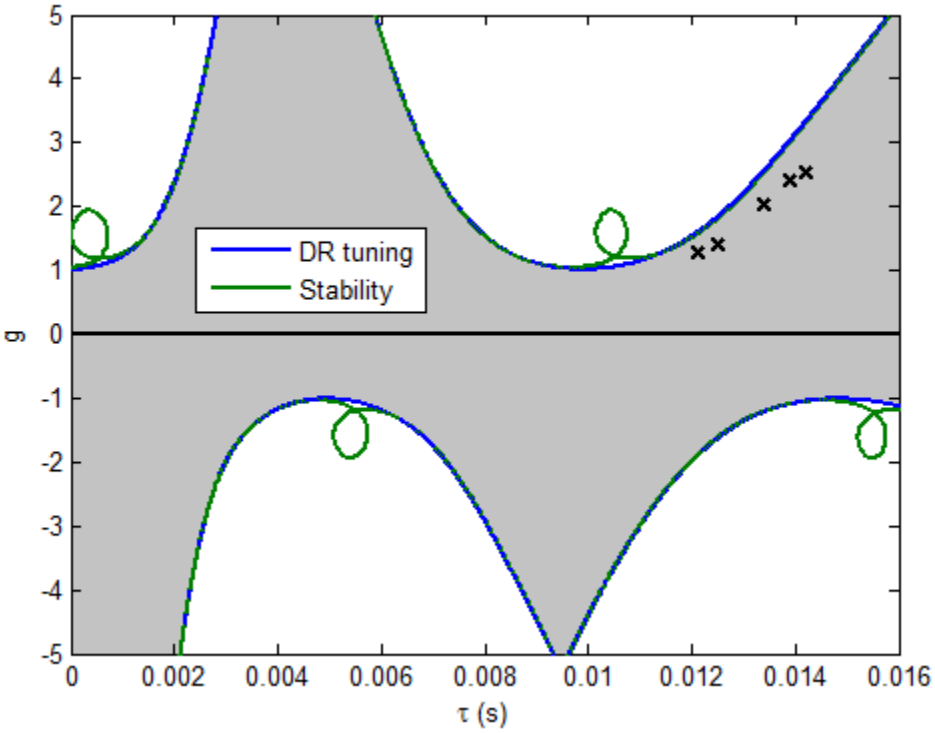

Figure 4.11. Combined system stability boundaries and DR tuning parameters for modified experimental setup. Stable & feasible region shaded and test points marked.

The stability tableau for this case is generated next. The combined system stability boundaries are calculated using the expressions in (1.5), after decomposing the characteristic equation (4.29) in the form of (1.4). The DR tuning parameters are also calculated, via (4.5) and are superimposed with the combined system stability boundaries. These are depicted on

Figure 4.11, where again the stable operating region is shaded in gray. Notice however, that stability is not the sole criteria to be considered here. Although some segments of the DR tuning parameters fall under the stable region, they still cannot be used for energy harvesting purposes, as it was shown under Section 2.4 that DR tuning does not permit the net energy harvesting capacity. Also, differently from the numerical case study under Section 3.5 (specifically Figure 3.9), note that a near-resonant DFVA tuning approach is not pursued here due to practical limitations associated with the experimental structure. It was observed during experiments that prescribed (τ, g) compositions tailored for energy harvesting purposes do not result in the performance predicted by analytical calculations.

4.2.4. Experimental assessment of energy harvesting performance

The experimental comparison and assessment procedure is described next. Several test points are used where the beam is excited at a certain frequency and the control parameters are tuned to associated (τ, g) compositions. Although these test points are not chosen according to a strict formula, the (τ, g) compositions for each frequency are mainly selected to be in the shaded stable zones on the marked locations depicted in Figure 4.11, located in the vicinity of the DR tuning parameters on the second positive branch. At each test run, the beam is excited through one of the PZT patches with a harmonic signal at the designated frequency. Initially the feedback control is turned off and the passive system's response is recorded. Then after several seconds of data is collected, the control is turned on, and the system response with the delayed feedback control is recorded. The recorded data is then transferred to a PC and analyzed in MATLAB.

For energy harvesting-related performance assessment, two signals are recorded using the dSPACE 1103 digital control unit:

1- The shunt circuit current, $i_s(t)$, is obtained by measuring the voltage across the lumped resistor in the shunt circuit, $V_R(t)$ (which also serves as the feedback measurement), and dividing this signal by the resistance value.

2- The control actuation voltage, $V_C(t)$, is directly recorded from the voltage amplifier output port.

Both signals are recorded through the controller's A/D converter and as a result, are subject to identical potential measurement/recording delays. The sampling frequency for these tests is 8000 Hz. Inspecting the control voltage time trace, the instance when the controller is turned on is determined, and the data is split into two parts; passive and active response data. Furthermore, the length of the passive response data is determined and the active response data is trimmed to the same length. This way, both passive and active response data are in identical length. As the next step, any voltage bias in the data is eliminated by calculating the mean values and subtracting them from the harmonic signals. Now the resulting time traces represent oscillations around zero. For each the passive and active system response, two key parameters are calculated:

1- The instantaneous power generated over the resistive load, P_{gen}, is calculated via (3.10), which is essentially the square of the current signal, multiplied with the resistance value.

2- The instantaneous power consumed by the control action, P_{ctrl}, is calculated via (3.14), which is simply the multiplication of the control voltage and the shunt circuit current. Notice that this quantity is zero for the passive system response, as there is no control action and hence $V_C(t) = 0$.

These instantaneous power quantities are then numerically integrated, to obtain potentially generated and consumed energy amounts, E_{gen} and E_{ctrl}, respectively, for the passive and active

responses. Notice that these time domain signals for the passive and active responses are equal in length and share the same frequency. As a result, the integration does not favor one signal over the other. The potentially harvested energy is calculated by subtracting the energy consumed by the control from the energy generated over the resistive load. That is, $E_{harv} = E_{gen} - E_{ctrl}$. This yields two E_{harv} quantities; one for the passive and active case each. In order to assess the feasibility of the active delayed control case, we calculate the percent increase (*PI*) in energy harvesting capacity analogous to the earlier definition in (3.21), as follows.

$$PI_e = \frac{E_{harv}^{active} - E_{harv}^{passive}}{E_{harv}^{passive}} \times 100 \tag{4.30}$$

The subscript *e* denotes that this is an experimentally observed quantity. This concludes the experimental assessment of energy harvesting performance using the delayed feedback control.

4.2.5. Analytical prediction of the energy harvesting performance

In order to understand how well the mathematical model of the system agrees with the experimental results, we analytically calculate the percent increase in energy harvesting capacity corresponding to the system/control parameters of each test run. In order to achieve accurate results this way, three parameters have to be identified as precisely as possible: The operating frequency ω, the control delay τ and control gain g. Although all of these parameters are manually adjusted by the user during the experimental test runs, slight deviations exist between user input and the actual effective values due to uncertainties within the control setup. The identification of these parameters is carried out using frequency domain analysis on the recorded signals. The two processed data segments corresponding to each test run, passive and active system responses, are converted to frequency domain using MATLAB's Fast Fourier Transform

(FFT) routine. Here, the operating frequency is determined by detecting the clearly pronounced peak in the amplitude spectrum. Notice that the resolution in frequency domain is the reciprocal of the signal length in time domain. Although signal length varied between measurements, it was generally kept in the vicinity of 5 seconds per segment. Hence, the overall approximate resolution in frequency domain is 0.2 Hz. Now that the operating frequency is known, the control parameters (τ, g) are determined next. Let us denote the feedback measurement [resistor voltage, $V_R(t)$] and the control output [control voltage, $V_C(t)$] in frequency domain as $V_R(\omega)$ and $V_C(\omega)$, respectively. Note that the time domain relation between these signals, $V_C(t) = gV_R(t - \tau)$, can be expressed in frequency domain as

$$V_C(\omega) = g\,\mathrm{e}^{-\tau\omega\mathrm{i}}\,V_R(\omega)\,. \tag{4.31}$$

Let us denote the experimentally measured operating frequency as ω_0. Then the frequency domain data bins of $V_R(\omega)$ and $V_C(\omega)$ corresponding to this frequency can be used to calculate the control gain and delay via (4.31) as

$$g_0 = \left|\frac{V_C(\omega_0)}{V_R(\omega_0)}\right|, \qquad \tau_0 = \frac{1}{\omega_0}\left(-\angle\frac{V_C(\omega_0)}{V_R(\omega_0)} + 2l\pi\right) \tag{4.32}$$

where l is the branch number used during control synthesis (in this case $l = 2$, as the second positive branch is used).

After the operation parameters ω_0, g_0, τ_0 for each measurement are identified via the procedure described here, they are substituted in (4.28) to analytically calculate the shunt circuit current's frequency response with respect to excitation voltage (in case the passive system response is considered, $g = 0$ is simply substituted in the same transfer function). Then for a unit input voltage, the amplitude of the current i_0 can be calculated. With this information, the

analytical formulae derived for energy harvesting performance can be used to calculate the average harvested power, as defined in (3.17). For each test case, a passive and active harvested power amount is calculated. These are then used to calculate the percent increase in energy harvesting capacity, defined in (3.21). Notice several advantages of using the percent increase as in (3.21) and (4.30) for the energy harvesting assessment. Because the increase is divided by the passive amount, the result is scaled and independent from input voltage amplitude. Another advantage is that the analytically calculated quantity as in (3.21) is in terms of average power over a cycle; whereas the experimentally calculated quantity as in (4.30) is in terms of energy that is obtained by integrating instantaneous power. However because the percent increase is scaled relative to the passive power/energy amount, the expressions (3.21) and (4.30) are equivalent and thus can be used directly to compare the analytical and experimental results. That is, any percent increase in average power harvested over a cycle will be equal to the percent increase in energy harvested over an arbitrary duration of time, as long as the passive and active measurements signals are of identical length.

4.2.6. Demonstration on sample test run and further results

The procedures for experimentally assessing energy harvesting capacity are applied here on a sample test case to clarify and illustrate the methods. For the rest run under consideration here, the excitation voltage signal was set to 85 Hz. Using the stability tableau in Figure 4.11, the control parameters are chosen in the stable shaded region, in the vicinity of the DR tuning parameters corresponding to this frequency, as $g = 2.5$ and $\tau = 0.0142$ s. These parameters are then set within the digital controller using the dSPACE ControDesk software. The raw measured data from a test run with this configuration is presented in Figure 4.12. Notice a clear bias in both signals that needs to be eliminated. The passive system response corresponds to the timeframe

running from 0 to approximately 5 seconds where the control voltage is zero. After that, the control action is turned on, as seen from the nonzero control voltage signal, in addition to a pronounced increase in resistor voltage oscillation amplitude. The exact time instant where control action is turned on is determined as $t = 5.46$ s. The data is separated from this point, meaning that the passive system response is in the interval of (0 s, 5.46 s). The active system response is trimmed to be equal in length, meaning that it corresponds to the interval of (5.46 s, 10.92 s) in the raw data. At this point the bias in the data is also removed and the resistor voltage measurement is divided by the lumped resistance value (12 kΩ) to obtain the shunt circuit current. The processed data is presented in Figure 4.13.

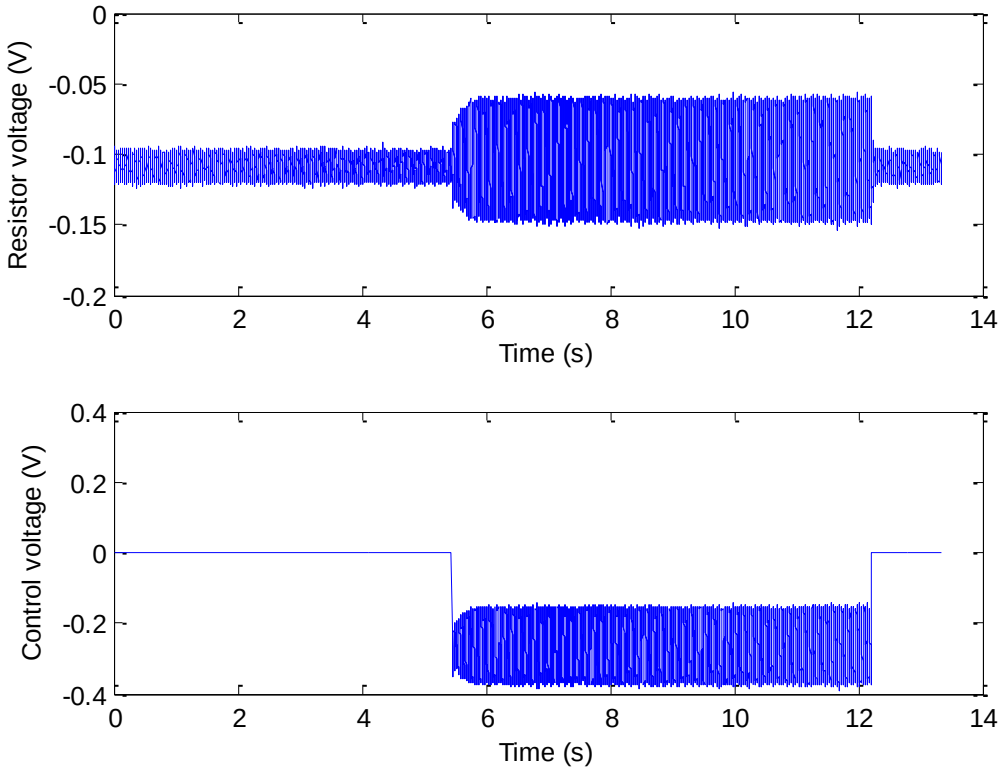

Figure 4.12. Raw measured data from the sample test run.

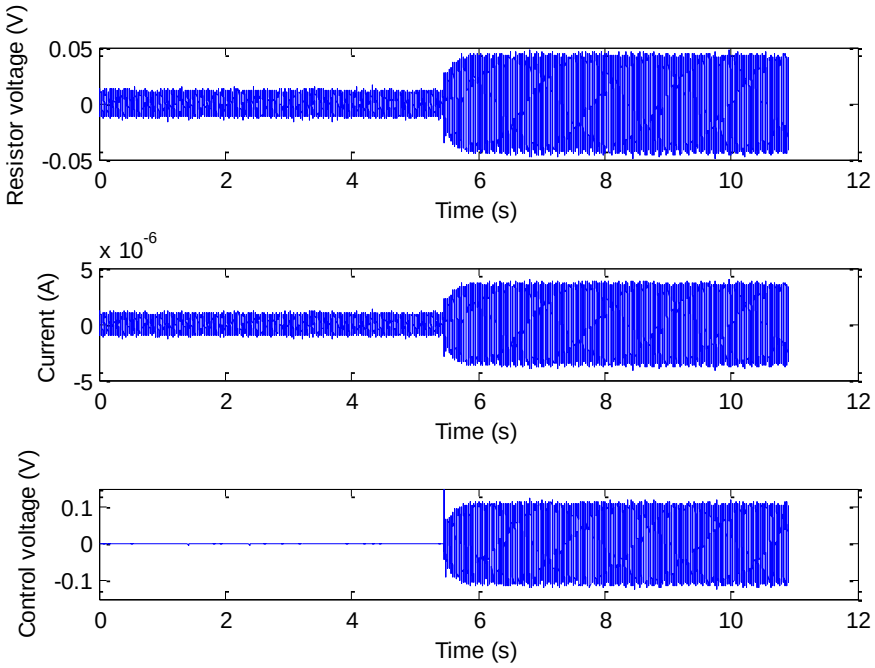

Figure 4.13. Processed data from the sample test run.

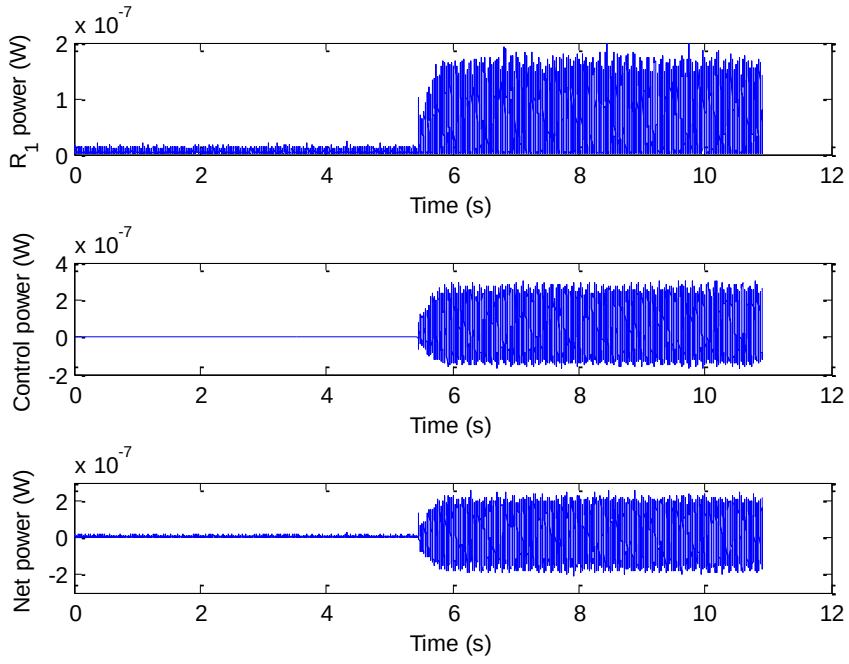

Figure 4.14. Instantaneous powers generated over the resistive load and consumed by control action; net (potentially harvested) instantaneous power.

The instantaneous powers generated over the resistive load and consumed by the control action are calculated now via (3.10) and (3.14), respectively. The *net*, or *potentially harvested*, power is simply the difference of the former two. All these power quantities are presented on Figure 4.14. As the next step, the harvested (net) power signals for the passive and active response are numerically integrated to calculate the potentially harvested energies as $E_{harv}^{passive} = 2.46\,\text{nJ}$ and $E_{harv}^{active} = 10.24\,\text{nJ}$, respectively. Then using (4.30), the increase in energy harvesting capacity is calculated as 316%.

Now that the experimentally observed increase in energy harvesting capacity is obtained, the analytically predicted value is calculated next, for comparison. Converting the time domain data to frequency domain, the excitation frequency is determined as ω_0 = 84.62 Hz (compared to the 85 Hz setting). Using the equations in (4.32), the effective control gain and delay values are $g_0 = 2.533$ and $\tau_0 = 0.0142$ s, respectively (user input was $g_0 = 2.5$ and $\tau_0 = 0.014$ s). The operational parameters associated with the rest run are then substituted in (4.28) and the shunt circuit's current amplitude with respect to unit excitation voltage is calculated (for the passive case, $g = 0$ is substituted). The average harvested power quantities, calculated analytically as per (3.17), are then obtained as $(P_{harv}^{av})_{passive} = 6.55\times10^{-11}\,\text{W}$ and $(P_{harv}^{av})_{active} = 2.89\times10^{-10}\,\text{W}$. Using (3.21), the increase in energy harvesting capacity according to the mathematical model is calculated as 340%. Compared to the experimentally observed value of 316%, a small difference exists, which is natural considering modeling uncertainties.

The procedure demonstrated here is repeated for several other test runs with varying excitation frequency. The results are tabulated and presented in Table 4.1.

Table 4.1. Experimental test data and analytical results for comparison.

User input	Frequency (Hz)	85	85	88	91	93
	Gain	2.5	2.4	2	1.4	1.25
	Delay (s)	0.014	0.014	0.0134	0.013	0.0122
Measured	Frequency (Hz)	84.62	85.19	88.38	91.61	93.03
	Gain	2.533	2.426	2.027	1.418	1.274
	Delay (s)	0.0142	0.0139	0.0134	0.0125	0.0121
Experimental *PI*		316%	−167%	242%	51%	21%
Analytical *PI*		340%	−62%	323%	46%	14%

4.2.7. Discussions on the results and the experimental setup

As seen from the results presented in Table 4.1, the experimentally observed results and analytically predicted values are overall in remarkable agreement. This match between the analytical and experimental domain was achieved by identifying some key parameters through experimental measurements. The frequency response characteristics of the system are used for this purpose. For the mathematical model at hand, these were depicted on the Bode magnitude plots in Figure 4.10. On the experimental setup, the system is excited harmonically at fifteen different frequencies in the vicinity of the second resonant mode, in a range approximately between 85 – 108 Hz. At each test point, the two system outputs, beam displacement and shunt circuit current are recorded, in addition to the input, excitation voltage. Notice that the circuit current is obtained by dividing the resistor voltage measurement by the resistance value, as described earlier. Using this data, an experimental frequency response is constructed. This procedure is again performed by converting the time domain signals to frequency domain using MATLAB's FFT routine. The excitation frequency ω_0 for each test point is determined by

identifying the peak frequency of signals' amplitude spectra. Then, using the corresponding frequency domain data, the amplitude responses are calculated as follows.

$$|G_w| = \left| \frac{w_t(\omega_0)}{V_{ex}(\omega_0)} \right|, \qquad |G_i| = \left| \frac{i_s(\omega_0)}{V_{ex}(\omega_0)} \right| \tag{4.33}$$

These experimentally obtained point-wise frequency response amplitudes are plotted against the analytical Bode magnitude responses, and presented in Figure 4.15.

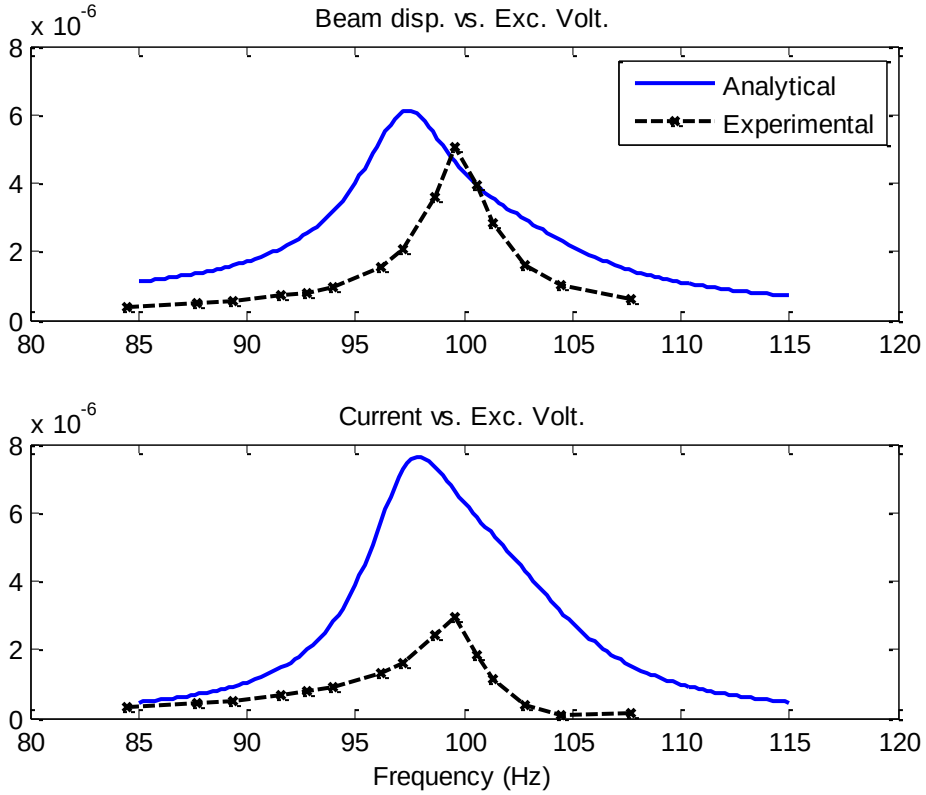

Figure 4.15. Comparison of analytical and experimental frequency response characteristics before experimental parameter identification.

This figure offers some insight into the discrepancies between the analytical model and the experimentally observed behavior. Notice that the peak frequency is offset by a few Hz and the

shunt circuit current response is significantly lower than the analytically expected results. Within the modeling effort, the highest amount of uncertainty is associated to the PZT patches, as it is difficult to accurately and reliably measure quantities such as k_{em1}, k_{em2} and k_{ic}. For this reason, it is suspected that the PZT elements are the main source of discrepancies. The inverse capacitive coefficient k_{ic} is obtained by inverting the capacitance of the PZT patch as measured with a multi-meter. The modal electro-mechanical coupling coefficients k_{em1}, k_{em2} however, cannot be directly measured in a similar fashion, and as a result, these parameters were adjusted in the mathematical model such that the experimentally observed behavior was mimicked. The frequency response comparison after this adjustment is presented in Figure 4.16.

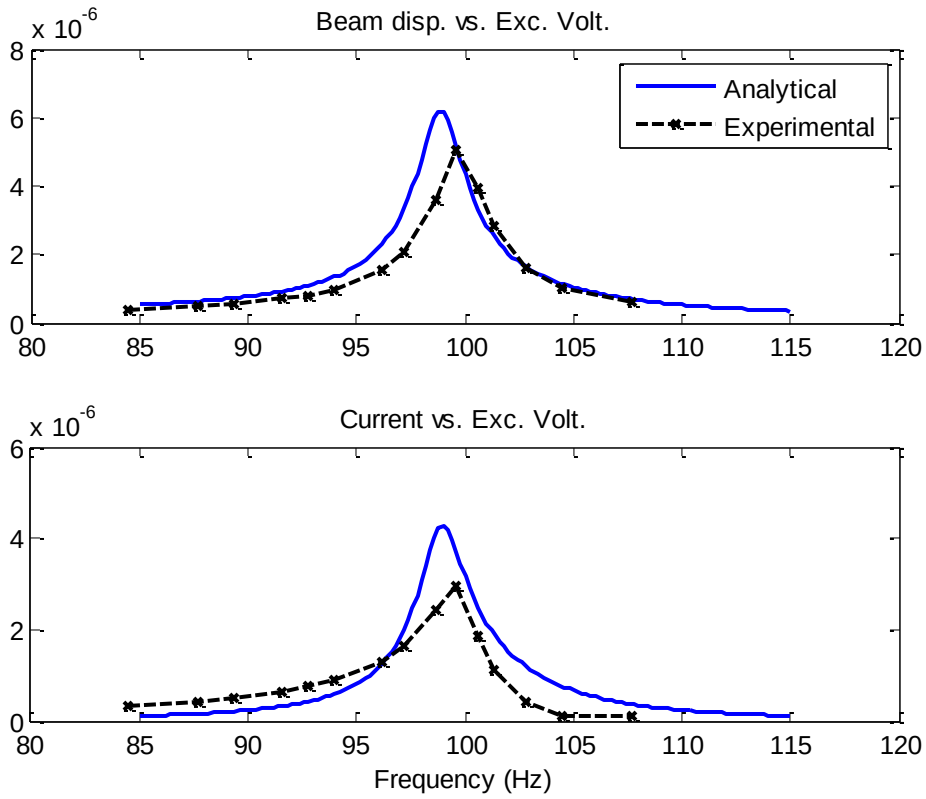

Figure 4.16. Comparison of analytical and experimental frequency response characteristics after experimental parameter identification.

Notice how the correspondence between the analytical and experimental model is significantly improved.

In order to analyze underlying reasons for the initial mismatch, a second type of test is conducted. This time, the shunt circuit is disconnected and instead, the electrodes of the shunting PZT patch are directly connected to a voltmeter. In this configuration, the circuit dynamics are eliminated, hence the system order reduces to 4. As the shunting PZT patch is open-circuit, there is no current and charge flow. That is $Q_s = 0$ and the voltage across the shunting PZT electrodes becomes

$$k_{em1}u_1 + k_{em2}u_2 = V_s\,. \tag{4.34}$$

The state-space representation for this configuration is

$$\dot{\mathbf{x}}(t) = \mathbf{A}\mathbf{x}(t) + \mathbf{B}v(t)\,, \qquad \mathbf{y}(t) = \mathbf{C}\mathbf{x}(t) \tag{4.35}$$

where

$$\mathbf{x}(t) = \begin{bmatrix} u_1(t) & u_2(t) & \dot{u}_1(t) & \dot{u}_2(t) \end{bmatrix}^T, \quad \mathbf{y}(t) = \begin{pmatrix} w_t(t) \\ V_s(t) \end{pmatrix}, \quad v(t) = V_{ex}(t)$$

$$\mathbf{A} = \begin{bmatrix} 0 & 0 & 1 & 0 \\ 0 & 0 & 0 & 1 \\ (k_{em1}^2/k_{ic} - k_{11})/m_{11} & (k_{em1}k_{em2}/k_{ic} - k_{12})/m_{11} & -c_{11}/m_{11} & -c_{12}/m_{11} \\ (k_{em1}k_{em2}/k_{ic} - k_{12})/m_{22} & (k_{em2}^2/k_{ic} - k_{22})/m_{22} & -c_{12}/m_{22} & -c_{22}/m_{22} \end{bmatrix},$$

$$\mathbf{B} = \begin{bmatrix} 0 \\ 0 \\ -k_{em1}/(k_{ic}m_{11}) \\ -k_{em2}/(k_{ic}m_{22}) \end{bmatrix}, \quad \mathbf{C} = \begin{bmatrix} \phi_1(x_t) & \phi_2(x_t) & 0 & 0 \\ k_{em1} & k_{em2} & 0 & 0 \end{bmatrix} \tag{4.36}$$

The transfer functions can now be obtained similarly to (4.25).

$$\begin{pmatrix} \dfrac{w_t(s)}{V_{ex}(s)} \\ \dfrac{V_s(s)}{V_{ex}(s)} \end{pmatrix} = \mathbf{C}(s\mathbf{I} - \mathbf{A})^{-1}\mathbf{B} \tag{4.37}$$

For the tests conducted in this configuration, we investigate the voltage across the shunting PZT electrodes, divided by the beam tip displacement. That is

$$\frac{V_s(s)}{w_t(s)} = \frac{k_{em1}u_1 + k_{em2}u_2}{\phi_1(x_t)u_1 + \phi_2(x_t)u_2}. \tag{4.38}$$

The reason for analyzing this relationship is that the test are conducted in the vicinity of second resonant mode, for which $u_2 > u_1$ and hence substituting $u_1 = 0$ in (4.38),

$$\frac{V_s(s)}{w_t(s)} \approx \frac{k_{em2}}{\phi_2(x_t)}. \tag{4.39}$$

This means that, according to the mathematical model at hand, dividing the PZT voltage by the beam displacement in the vicinity of a resonant mode should yield a characteristic that resembles a constant. In other words, the frequency response of (4.38) should ideally have flat amplitude and zero phase angle (or 180 degrees for negative quantity). The analytical description for (4.38) easily obtained by dividing the transfer functions from (4.37). Substituting numerical values, it is obtained as

$$\frac{V_s(s)}{w_t(s)} = \frac{2.327\times10^{-13}s^3 + 3235s^2 + 2.369\times10^4 s + 8.454\times10^7}{3.375\times10^{-14}s^3 - 0.1311s^2 - 0.9604s + 1.396\times10^4}. \tag{4.40}$$

The experimental calculation of this quantity is carried out in a similar fashion to the frequency response analysis in (4.33). Once again, the excitation frequency ω_0 is determined from the amplitude spectra and then the frequency domain data corresponding to this frequency is used to calculate the complex frequency response quantity as $V_s(\omega_0) / w_t(\omega_0)$. The amplitude and phase angle are compared by superimposing the experimentally calculated results with the analytically predicted ones. These are presented in Figure 4.17.

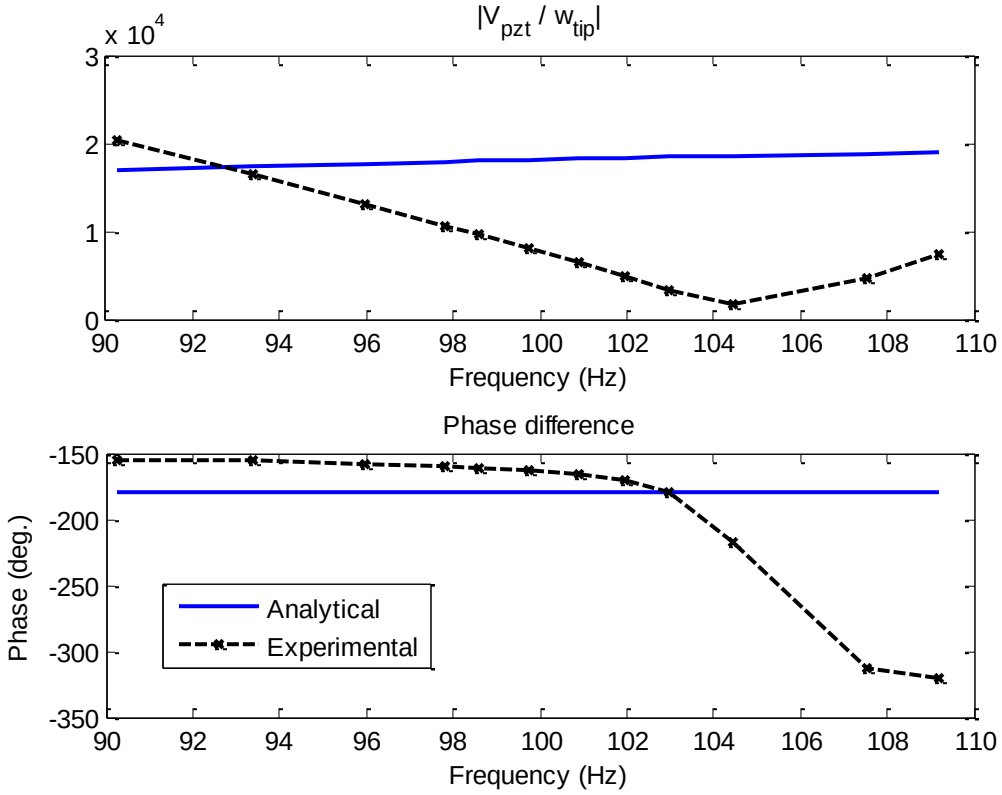

Figure 4.17. Comparison of analytical and experimental frequency response characteristics.

These results shown in Figure 4.17 reveal significant non-ideal behavior. First of all, notice that the analytical frequency response indeed resembles a constant, with near-flat amplitude response and steady −180 degree phase angle. The experimentally measured behavior, however, is quite different and offers explanations to discrepancies observed earlier. It is seen

that the amplitude of PZT voltage decreases steadily until a minimum around 104 Hz, and increases afterwards. As seen from (4.39), the behavior of the system here is strongly influenced by the electro-mechanical coupling coefficient k_{em2} and the beam's shape function ϕ_2. This implies that either one of these terms, or both, exhibit non-ideal behavior and do not remain constant. Li et al. (1991) report from experimental results that the coupling coefficient in PZT ceramics can vary depending on electrical field levels. In this case, the electrical field across the electrodes increases at frequencies closer to resonance, which may offer some explanation to the behavior seen in Figure 4.17. The beams used in this experiment are made of Aluminum, with very thin profiles. Another possibility is that the beam deformation does not obey to the shape function as vibration amplitude increases around resonance. It is known that in general, piezoelectric materials may exhibit non-linear and non-ideal behavior at high stresses and larger deformations (Cao and Evans, 1993). The experimental results from this second test (Figure 4.17) document several non-ideal characteristics of the experimental setup used within this work. Under the light of this information, certain discrepancies in system modeling are quite natural and expected.

Chapter 5. Conclusions and Future Work Recommendations

5.1.Review of Highlight Contributions

The highlights of this work can be listed as follows.

- The main analytical contribution is the development of time delayed feedback control laws to sensitize energy harvesting structures. Control parameter compositions are synthesized for this objective and the influence of various factors on energy harvesting performance is investigated. It is shown analytically and experimentally that energy harvesting capacity can be significantly increased with this approach.

- Time delayed feedback control laws are introduced to active piezoelectric networks. The contributions in this front are on two distinct aspects:

  (1) Improved vibration suppression performance with delayed resonator tuning in piezoelectric shunt circuits. Development of an open-loop measurement based control parameter correction scheme.

  (2) Implementation of the analytical results on energy harvesting capacity within piezoelectric networks. Development of a state-space model involving dual mode beam dynamics and detailed input-output definitions.

In addition, extensive experimental work is conducted to prove the demonstrated concepts and identify potential practical challenges.

5.2.Summary and Conclusions

This work follows a line of research where time delays are deliberately injected in feedback control laws to exploit some of their unique features. The Delayed Resonator (DR) concept serves as a strong inspiration and its theoretical foundation is revisited in Chapter 1. The concept of inducing marginal stability (i.e., resonance) in an active vibration absorber through the use of a delayed control law is elucidated. The concept of stability maps (stability tableaus) is introduced here, and the D-subdivision method for delay-dependent stability assessment is discussed. Also mentioned is the concept of Delayed Feedback Vibration Absorbers (DFVA), which are a generalization of the DR concept where the feedback law does not induce resonance but tunes the absorber to different requirements. This concept is proven to be quite relevant and of interest within following sections of the document.

The idea of utilizing delayed feedback control to enhance energy harvesting in resonator based systems is proposed under Chapter 2. The analytical development is carried out on a traditional mass-spring-damper type active vibration absorber, where it is assumed that the dissipative element (damper) is a transducer that generates electrical energy. On the other hand, the actuator which exerts the control law consumes energy for this purpose. The generated and consumed energy are investigated from a physics viewpoint. Analytical expressions are derived to describe the energy relations in terms of excitation frequency and the control parameters, gain and delay. In case this active absorber is mounted on a primary structure, analysis shows that tuning the control law to DR conditions does not permit energy harvesting. That is, all energy generated through the transducer equals to the amount of energy required for the tuning effort. At this point, the DFVA concept mentioned under Chapter 1 is introduced. It is shown that the absorber can be sensitized instead of pure resonance, to yield significant gains in energy

harvesting capacity. A numerical case study is presented to further demonstrate the findings. Several detailed topics such as system parameter influence on energy harvesting, and the effects of control branch selection are discussed.

In Chapter 3, piezoelectric materials and the concept of piezoelectric networks is introduced. The bi-directional electro-mechanical coupling induced by piezoelectricity enables the use of electrical circuits to serve in lieu of mechanical vibration absorbers. In this context, resistive-inductive shunt circuits are investigated, which become analogous to mass-spring-damper type resonators through the use of piezoelectric elements. These systems have been used for vibration control purposes in earlier literature and they present a very interesting platform for applying the DR and DFVA theory. A typical benchmark setup that consists of a metal cantilever beam with piezoelectric patches connected to a shunt circuit is considered. Using modal truncation, a single mode is used to describe the beam dynamics. Adopting a method based on Hamilton's principle, a set of coupled differential equations is derived that govern the displacement of the beam and the dynamics in the shunt circuit. A delayed proportional control law is implemented in the circuit. This is achieved by measuring the voltage drop across the resistor element as the feedback signal. The control actuation is achieved via a voltage source in the circuit. On this construct, the DR theory is used to devise control parameters that induce resonance in the shunt circuit such that tonal vibrations in the beam can be suppressed. The results derived under Chapter 2 for energy harvesting are also extended on this construct. In fact, piezoelectric networks serve as a more realistic application platform, as many researchers consider resistive loads for energy harvesting assessment in these types of systems. This means that the resistance in the shunt circuit is assumed to be a load that generates useful electrical energy. A case study is adopted from literature and the developed theory is demonstrated.

Experimental work to verify the analytical findings is presented in Chapter 4. The benchmark setup studied under Chapter 3 is realized, consisting of a cantilever beam with lead zirconate titanate (PZT) type piezoelectric patches attached to a shunt circuit. A typical application challenge, namely an unusually high inductance requirement is encountered. A capacitor parallel to the PZT patch, in conjunction with a synthetic inductor op-amp circuit is used to mitigate the problem. For DR implementation, it is observed that small parameter uncertainties cause problems in achieving the exact resonant configuration. A method is developed to update the control parameters such that ideal performance can be achieved. Open loop measurements are converted to frequency domain using an online Fast Fourier Transform (FFT) routine. Frequency domain analysis methods are then used for fine-tuning the control gain and delay. After DR operation is successfully achieved within the piezoelectric network, the focus is shifted to energy harvesting related results. The experimental setup is modified to serve this purpose. A dual mode beam model is derived for the modified setup because the operating range is chosen to be within the second resonant mode of the beam. Assuming that the resistor element in the shunt circuit is a resistive load, analytical results on this construct declare that energy harvesting capacity can be significantly increased over the excitation frequency spectrum, except resonant frequency neighborhoods. These results are tested experimentally here, by operating on the lower side of the second resonant mode frequency. Experimental results demonstrate that the theory indeed holds and energy harvesting capacity can be increased by using the delayed control laws. Slight discrepancies between analytical and experimental quantities are observed. The system is subjected to several frequency response tests and the experimental parameter identification effort is documented.

5.3.Recommendations for Future Work

Throughout the work that is developed within this document, several points stand out as open challenges where future work would yield improvements. Some of these issues are discussed here, together with recommendations on how they could be improved.

Regarding the theoretical development on delayed feedback and energy harvesting under Chapter 2, the analysis is based on several assumptions and simplifications. The main theory is derived on a generic active mechanical vibration absorber, and it is assumed that the dissipative element (normally a damper) is a transducer that can generates electrical energy instead of dissipating it. The transducer model neglects specifics such as the transducer mechanism and possible associated losses. For a real application involving a mechanical absorber, conversion losses exist, and parasitic damping due to friction is also a concern. Incorporating a higher fidelity transducer model in the analysis could include such effects and may render more realistic results. These discussions are mainly concerned with the assessment of the potentially generated energy from the system. An equally important point is the energy that is consumed by the control actuation effort. In this work, the consumed energy was analyzed from a purely physical perspective (for instance, instantaneous power consumption is taken as product of force and velocity). However the actual energy consumed by a physical actuator is more complex and includes multiple components such as driving amplifiers. Depending on the exact nature of an application, more detailed power consumption characteristics could be included to yield a realistic assessment.

The arguments about energy generation and consumption should be repeated for the experimental case where energy harvesting performance is studied in the piezoelectric shunt circuit. Here it is assumed that the resistance in the circuit is a resistive load that generates useful

electrical energy. Although this approach is widespread in literature, energy harvesting circuits are more complex in nature and do not usually come with purely resistive impedances. Incorporating a more detailed energy harvesting circuit model within the analysis would yield a better understanding of generated energy in real-world applications. Similarly, the power consumed within the active shunt circuit is simply taken as a product of control voltage and circuit current. While this is the physical definition of instantaneous electrical power, certain important points are neglected. For instance, the power consumption of the controller unit is not taken into consideration. Similarly, the voltage amplifier used to exert the control signal has undoubtedly more complex power consumption characteristics that are not included within the analysis here. More specific studies, incorporating more aspects of energy consumption throughout the active control action would yield higher fidelity in the results and would be very beneficial from a practical applications viewpoint.

The use of piezoelectric elements introduces many challenges in experimental studies. The parameters associated with the PZT patches, such as electro-mechanical coupling and inverse-capacitive coefficients carry significant uncertainties with them. In fact, severe non-ideal behavior is measured and documented for the setup used here. An important component that contributes to these deficiencies is the materials and construction of the setup. Relatively inexpensive PZT patches were used, which means that material characteristics might not be as stable and consistent as more expensive counterparts. Similarly, some fabrication methods, specifically the bonding of the PZT patches to the beams is a challenging task. The fabrication of the setup was conducted with limited experience and facilities, which may cause further deterioration. The use of higher fidelity equipment, in conjunction with expert fabrication techniques would undoubtedly yield better performance and more correlation between analytical

and experimental results. On the other hand, even high quality piezoelectric materials have inherent nonlinearities associated with them. Such specifics were neglected within this work, but could be incorporated to increase the fidelity in modeling.

Another potential method to mitigate parameter uncertainties is to use a more advanced control correction scheme. The method used in this work offers limited adaptive performance and relies on the assumption that certain system parameters are constant and precisely known, which is unfortunately not the case. In order to provide more reliable results, especially over a broader frequency range, a different control correction scheme could be pursued. For instance, in the case of vibration suppression, an automatic tuning procedure could be devised that iteratively fine-tunes control parameters until beam vibration is completely eliminated.

Appendix A. Coupled Beam and Piezoelectric Network Model

Throughout this section, subscripts *b* and *p* are used to distinguish parameters associated with the beam and the piezoelectric patches, respectively. The modeling approach in this work is adopted from Tang & Wang (2001) and is based on Hamilton's principle. Detailed expressions for the system parameters are presented below and more information on their derivations is available in the cited document. We simply declare the relations among the key elements in what follows.

Table A.1. Nomenclature

A	Cross-sectional area	c_b	Damping along beam	l	Length
E	Elastic modulus	f	Forcing along beam	w	Width
S	First moment of area	I	Second moment of area	t	Thickness
h_{31}	Piezoelectric constant	β_{33}	Dielectric constant	ρ	Density
x_1, x_2	Starting/ending locations of piezoelectric patch along beam				

$$m_{11} = m_{b11} + 2m_{p11}, \qquad m_{22} = m_{b22} + 2m_{p22},$$

$$k_{11} = k_{b11} + 2k_{p11}, \qquad k_{22} = k_{b22} + 2k_{p22}, \qquad k_{12} = k_{b12} + 2k_{p12},$$

$$m_{b11} = \int_0^{l_b} \rho_b A_b \phi_1^2 dx, \quad m_{p11} = \int_{x_1}^{x_2} \rho_p A_p \phi_1^2 dx, \quad m_{b22} = \int_0^{l_b} \rho_b A_b \phi_2^2 dx, \quad m_{p22} = \int_{x_1}^{x_2} \rho_p A_p \phi_2^2 dx,$$

$$k_{b11} = \int_0^{l_b} E_b I_b (\phi_1'')^2 dx, \quad k_{p11} = \int_{x_1}^{x_2} E_p I_p (\phi_1'')^2 dx, \quad k_{b22} = \int_0^{l_b} E_b I_b (\phi_2'')^2 dx, \quad k_{p22} = \int_{x_1}^{x_2} E_p I_p (\phi_2'')^2 dx,$$

$$k_{b12} = \int_0^{l_b} E_b I_b \phi_1'' \phi_2'' dx, \quad k_{p12} = \int_{x_1}^{x_2} E_p I_p \phi_1'' \phi_2'' dx,$$

$$k_{em1} = \frac{k_{pq1}}{w_p l_p}, \quad k_{em2} = \frac{k_{pq2}}{w_p l_p}, \quad k_{ic} = \frac{k_{pp}}{(w_p l_p)^2},$$

$$k_{pq1} = \int_{x_1}^{x_2} h_{31} S_p \phi_1'' dx, \quad k_{pq2} = \int_{x_1}^{x_2} h_{31} S_p \phi_2'' dx, \quad k_{pp} = \int_{x_1}^{x_2} \beta_{33} A_p dx,$$

$$c_{11} = \int_0^{l_b} c_b \phi_1^2 dx, \quad c_{22} = \int_0^{l_b} c_b \phi_2^2 dx, \quad c_{12} = \int_0^{l_b} c_b \phi_1 \phi_2 dx,$$

$$F_{m1} = \int_0^{l_b} f\phi_1 dx, \quad F_{m2} = \int_0^{l_b} f\phi_2 dx, \quad \phi_1'' = d^2\phi_1 / dx^2, \quad \phi_2'' = d^2\phi_2 / dx^2$$

where the shape functions ϕ_1, ϕ_2 for the beam are (Inman, 2014)

$$\phi_n = \phi_n(x) = \left[\frac{\cosh \alpha_n l_b - \cos \alpha_n l_b}{\sinh \alpha_n l_b - \sin \alpha_n l_b} (\sinh \alpha_n x - \sin \alpha_n x) - \cosh \alpha_n x + \cos \alpha_n x \right], \quad n = 1, 2$$

$$\text{with} \quad \alpha_1 = 1.8751 / l_b, \ \alpha_2 = 4.6941 / l_b.$$

During the calculation of equivalent mass and stiffness, the contribution of piezoelectric elements is multiplied by two, as there are two symmetrical patches on the beam. For the piezoelectric coefficients k_{pq1}, k_{pq2} and k_{pp}, uniform electric displacement field is assumed.

Appendix B. Physical Parameters of Experimental Setup

Table B.1. Physical parameters of the first setup used during DR experiments

l_b	0.279 m	w_b	25 mm	w_p	21 mm	E_b	207 GPa	ρ_b	7750 kg/m^3
x_l	22 mm	t_b	3 mm	t_p	0.55 mm	E_p	65 GPa	ρ_p	7600 kg/m^3
x_r	43 mm	h_{31}	6.695×10^8	β_{33}	5.647×10^7				

Table B.2. Physical parameters of the modified setup used for energy harvesting experiments

l_b	0.2 m	w_b	20 mm	w_p	0.021 mm	E_b	68 GPa	ρ_b	2700 kg/m^3
x_l	3 mm	t_b	0.75 mm	t_p	0.000267 m	E_p	62 GPa	ρ_p	7800 kg/m^3
x_r	28 mm	h_{31}	6.624×10^8	β_{33}	3.227×10^7				

Appendix C. Synthetic Inductor Circuit

The synthetic inductor circuit diagram is depicted in Fig. C.1 (Chen, 1986). The operational amplifiers introduce the following conditions:

i) No voltage difference across input terminals.

ii) Input terminals do not draw current.

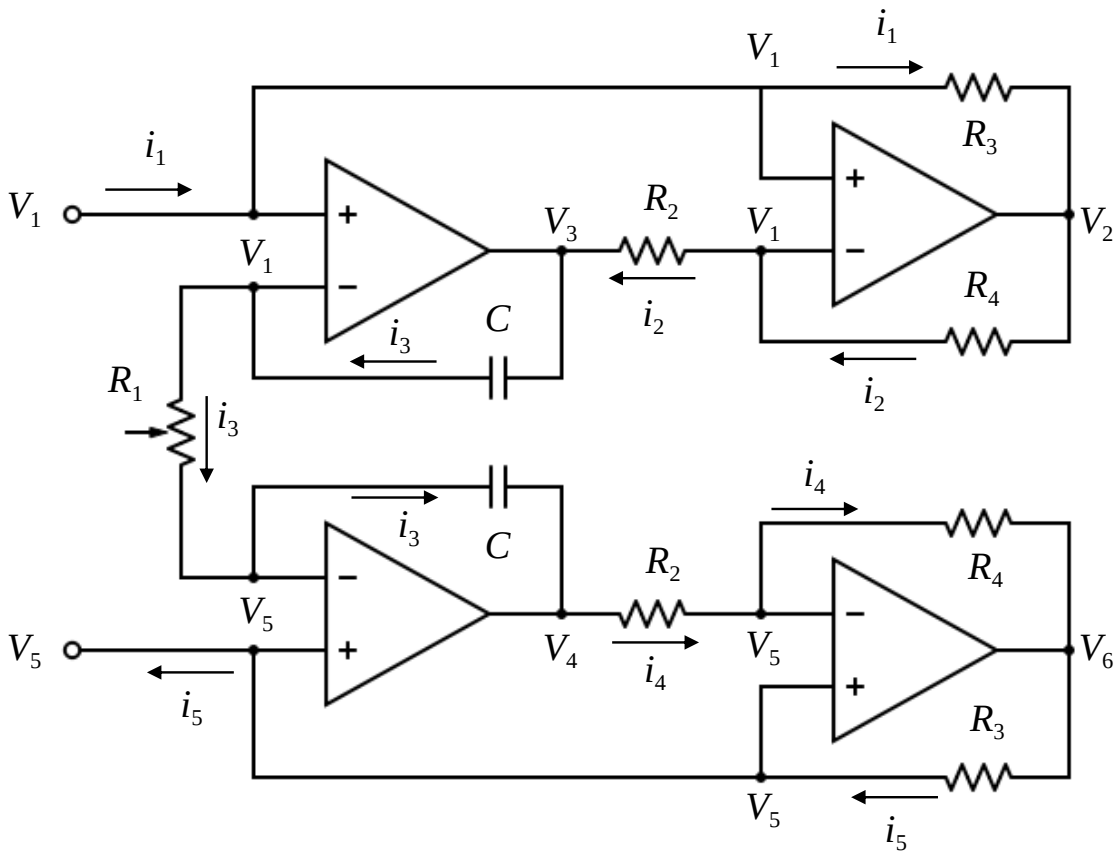

Fig. C.1. Synthetic inductor circuit.

Applying these conditions on the circuit, the distinct voltages and currents are identified and marked on Fig. C.1. Using Kirchhoff's laws, the remaining unknowns can be solved in terms of each other, resulting in the following two relations.

$$i_1(s) = \frac{R_4}{R_1 R_2 R_3 Cs}[V_1(s) - V_5(s)], \quad i_5(s) = \frac{R_4}{R_1 R_2 R_3 Cs}[V_1(s) - V_5(s)] \tag{C.1}$$

Then it is obvious that $i_1 = i_5$, and the equivalent impedance can be derived as

$$Z_{eq}(s) = \frac{V_1(s) - V_5(s)}{i_1} = \frac{R_1 R_2 R_3 C}{R_4} s\,. \tag{C.2}$$

This value can be adjusted by the potentiometer R_1.

References

Agnes, G. S. (1995). Development of a modal model for simultaneous active and passive piezoelectric vibration suppression. *Journal of Intelligent Material Systems and Structures, 6*(4), 482-487.

Bailey, T., & Ubbard, J. E. (1985). Distributed piezoelectric-polymer active vibration control of a cantilever beam. *Journal of Guidance, Control, and Dynamics*, *8*(5), 605-611.

Beeby, S. P., Tudor, M. J., & White, N. M. (2006). Energy harvesting vibration sources for microsystems applications. *Measurement science and technology*, *17*(12), R175.

Behrens, S., Moheimani, S. R., & Fleming, A. J. (2003). Multiple mode current flowing passive piezoelectric shunt controller. *Journal of Sound and Vibration*, *266*(5), 929-942.

Bisgaard, M., la Cour-Harbo, A., & Bendtsen, J. D. (2010). Adaptive control system for autonomous helicopter slung load operations. *Control Engineering Practice*, *18*(7), 800-811.

Cao, H., & Evans, A. G. (1993). Nonlinear deformation of ferroelectric ceramics. *Journal of the American Ceramic Society*, *76*(4), 890-896.

Cepeda-Gomez, R., & Olgac, N. (2013). Exact stability analysis of second-order leaderless and leader–follower consensus protocols with rationally-independent multiple time delays. *Systems & Control Letters*, *62*(6), 482-495.

Chen, W. K. (1986). *Passive and active filters: theory and implementations*. New York: Wiley.

Crawley, E. F., & De Luis, J. (1987). Use of piezoelectric actuators as elements of intelligent structures. *AIAA journal*, *25*(10), 1373-1385.

De Marneffe, B., & Preumont, A. (2008). Vibration damping with negative capacitance shunts: theory and experiment. *Smart Materials and Structures*, *17*(3), 035015.

Den Hartog, J. P., (1956). *Mechanical Vibrations* (Vol. 4). New York: McGraw-Hill.

Dorf, R. C., & Svoboda, J. A. (2010). *Introduction to electric circuits*. John Wiley & Sons.

Ergenc, A. F., Olgac, N., & Fazelinia, H. (2007). Extended Kronecker summation for cluster treatment of LTI systems with multiple delays. *SIAM Journal on Control and Optimization*, *46*(1), 143-155.

Eris, O., Ergenc, A. F., & Kurtulan, S. (2014, November). Use of non-identical multiple delayed resonators in active suspension systems of railway vehicles. In *Control System, Computing and Engineering (ICCSCE), 2014 IEEE International Conference on* (pp. 588-591). IEEE.

Filipović, D., & Olgac, N. (2002). Delayed resonator with speed feedback – design and performance analysis. *Mechatronics*, *12*(3), 393-413.

Fleming, A. J., Behrens, S., & Moheimani, S. O. R. (2003). Reducing the inductance requirements of piezoelectric shunt damping systems. *Smart materials and structures*, *12*(1), 57.

Forward, R. L. (1979). Electronic damping of vibrations in optical structures. *Applied optics*, *18*(5), 690-697.

Gao, Q., & Olgac, N. (2015). Dixon Resultant for Cluster Treatment of LTI Systems with Multiple Delays. *IFAC-PapersOnLine*, *48*(12), 21-26.

Gupta, A., Jendrzejczyk, J. A., Mulcahy, T. M., & Hull, J. R. (2006). Design of electromagnetic shock absorbers. *International Journal of Mechanics and Materials in Design*, *3*(3), 285-291.

Hagood, N. W., Chung, W. H., & Von Flotow, A. (1990). Modelling of piezoelectric actuator dynamics for active structural control. *Journal of Intelligent Material Systems and Structures, 1*(3), 327-354.

Hagood, N. W., & Crawley, E. F. (1991). Experimental investigation into passive damping enhancement for space structures. *Journal of guidance, control, and dynamics, 14*(6), 1100-1109.

Hagood, N. W., & von Flotow, A. (1991). Damping of structural vibrations with piezoelectric materials and passive electrical networks. *Journal of Sound and Vibration*, *146*(2), 243-268.

Harb, A. (2011). Energy harvesting: State-of-the-art. *Renewable Energy*,*36*(10), 2641-2654.

Henry, R. J., Masoud, Z. N., Nayfeh, A. H., & Mook, D. T. (2001). Cargo pendulation reduction on ship-mounted cranes via boom-luff angle actuation. *Journal of Vibration and Control*, *7*(8), 1253-1264.

Heywood, J. B. (1988). *Internal combustion engine fundamentals* (Vol. 930). New York: Mcgraw-hill.

Hosek, M., Elmali, H., & Olgac, N. (1997). A tunable torsional vibration absorber: the centrifugal delayed resonator. *Journal of Sound and Vibration*, *205*(2), 151-165.

Hosek, M., Olgac, N., & Elmali, H. (1999). The centrifugal delayed resonator as a tunable torsional vibration absorber for multi-degree-of-freedom systems. *Journal of Vibration and Control*, *5*(2), 299-322.

Hosek, M., & Olgac, N. (2002). A single-step automatic tuning algorithm for the delayed resonator vibration absorber. *Mechatronics, IEEE/ASME Transactions on*, *7*(2), 245-255.

Huang, X. W., & Zhao, Y. Y. (2013). The Effect of Delayed Feedback Control on Lateral Semi-Active Suspension System for High-Speed Train. *Advanced Materials Research*, 753, 1795-1799.

Iliuk, I., Balthazar, J. M., Tusset, A. M., Piqueira, J. R., de Pontes, B. R., Felix, J. L., & Bueno, Á. M. (2013). Application of passive control to energy harvester efficiency using a nonideal portal frame structural support system. *Journal of Intelligent Material Systems and Structures*, 1045389X13500570.

Inman, D. J., (2014). *Engineering vibration* (Vol. 4). Upper Saddle River: Prentice Hall.

Jalili, N., & Olgac, N. (2000). A sensitivity study on optimum delayed feedback vibration absorber. *Journal of dynamic systems, measurement, and control*, *122*(2), 314-321.

Jalili, N., & Esmailzadeh, E. (2001). Optimum active vehicle suspensions with actuator time delay. *Journal of Dynamic Systems, Measurement, and Control*, *123*(1), 54-61.

Kammer, A. S., & Olgac, N. (2016). Delayed-feedback vibration absorbers to enhance energy harvesting. *Journal of Sound and Vibration, 363*, 54-67.

Karami, M. A., & Inman, D. J. (2011). Equivalent damping and frequency change for linear and nonlinear hybrid vibrational energy harvesting systems. *Journal of Sound and Vibration*, *330*(23), 5583-5597.

Khaligh, A., Zeng, P., & Zheng, C. (2010). Kinetic energy harvesting using piezoelectric and electromagnetic technologies—state of the art. *Industrial Electronics, IEEE Transactions on*, *57*(3), 850-860.

Kolmanovskiĭ, V. B., & Nosov, V. R. (1986). *Stability of Functional Differential Equations*. New York: Academic Press.

Kong, N., Ha, D. S., Erturk, A., & Inman, D. J. (2010). Resistive Impedance Matching Circuit for Piezoelectric Energy Harvesting. *Journal of Intelligent Material Systems and Structures*, *21*(13), 1293-1302.

Lee, Y. S., & Elliott, S. J. (2001). Active position control of a flexible smart beam using internal model control. *Journal of Sound and Vibration*, *242*(5), 767-791.

Lefeuvre, E., Badel, A., Richard, C., & Guyomar, D. (2005). Piezoelectric energy harvesting device optimization by synchronous electric charge extraction. *Journal of Intelligent Material Systems and Structures*, *16*(10), 865-876.

Lesieutre, G. A. (1998). Vibration damping and control using shunted piezoelectric materials. *The Shock and Vibration Digest*, *30*(3), 187-195.

Li, S., Cao, W., & Cross, L. E. (1991). The extrinsic nature of nonlinear behavior observed in lead zirconate titanate ferroelectric ceramic. *Journal of applied physics*, *69*(10), 7219-7224.

Li, Z., Zuo, L., Luhrs, G., Lin, L., & Qin, Y. X. (2013). Electromagnetic energy-harvesting shock absorbers: design, modeling, and road tests. *Vehicular Technology, IEEE Transactions on*, *62*(3), 1065-1074.

Librescu, L., & Marzocca, P. (2005). Advances in the linear/nonlinear control of aeroelastic structural systems. *Acta Mechanica*, *178*(3-4), 147-186.

Litak, G., Friswell, M. I., & Adhikari, S. (2010). Magnetopiezoelastic energy harvesting driven by random excitations. *Applied Physics Letters*, *96*(21), 214103.

Masoud, Z. N., Nayfeh, A. H., & Nayfeh, N. A. (2005). Sway reduction on quay-side container cranes using delayed feedback controller: simulations and experiments. *Journal of Vibration and Control*, *11*(8), 1103-1122.

Mitcheson, P. D., Yeatman, E. M., Rao, G. K., Holmes, A. S., & Green, T. C. (2008). Energy harvesting from human and machine motion for wireless electronic devices. *Proceedings of the IEEE, 96*(9), 1457-1486.

Nakano, K., Suda, Y., & Nakadai, S. (2003). Self-powered active vibration control using a single electric actuator. *Journal of Sound and Vibration*,*260*(2), 213-235.

Niculescu, S. I. (2002). On delay robustness analysis of a simple control algorithm in high-speed networks. *Automatica*, *38*(5), 885-889.

Olgac, N., & Holm-Hansen, B. T. (1994). A novel active vibration absorption technique: delayed resonator. *Journal of Sound and Vibration*, *176*(1), 93-104.

Olgac, N., & Holm-Hansen, B. (1995). Tunable active vibration absorber: the delayed resonator. *Journal of dynamic systems, measurement, and control*,*117*(4), 513-519.

Olgac, N., Elmali, H., Hosek, M., & Renzulli, M. (1997). Active vibration control of distributed systems using delayed resonator with acceleration feedback. *Journal of dynamic systems, measurement, and control*, *119*(3), 380-389.

Olgac, N., & Jalili, N. (1998). Modal analysis of flexible beams with delayed resonator vibration absorber: theory and experiments. *Journal of Sound and Vibration*, *218*(2), 307-331.

Olgac, N., & Sipahi, R. (2002). An exact method for the stability analysis of time-delayed linear time-invariant (LTI) systems. *Automatic Control, IEEE Transactions on*, *47*(5), 793-797.

Olgac, N., & Sipahi, R. (2005). A unique methodology for chatter stability mapping in simultaneous machining. *Journal of Manufacturing Science and Engineering, 127*(4), 791-800.

Olgac, N., Zalluhoglu, U., & Kammer, A. S. (2014). Predicting Thermoacoustic Instability: A Novel Analytical Approach and Its Experimental Validation. *Journal of Propulsion and Power, 30*(4), 1005-1015.

Ottman, G. K., Hofmann, H. F., Bhatt, A. C., & Lesieutre, G. A. (2002). Adaptive piezoelectric energy harvesting circuit for wireless remote power supply. *Power Electronics, IEEE Transactions on*, *17*(5), 669-676.

Paradiso, J. A., & Starner, T. (2005). Energy scavenging for mobile and wireless electronics. *Pervasive Computing, IEEE, 4*(1), 18-27.

Renzulli, M. E., Ghosh-Roy, R., & Olgac, N. (1999). Robust control of the delayed resonator vibration absorber. *Control Systems Technology, IEEE Transactions on*, *7*(6), 683-691.

Richard, J. P. (2003). Time-delay systems: an overview of some recent advances and open problems. *Automatica*, *39*(10), 1667-1694.

Roundy, S., & Wright, P. K. (2004). A piezoelectric vibration based generator for wireless electronics. *Smart Materials and structures, 13*(5), 1131-1142.

Saha, C. R., O'donnell, T., Wang, N., & McCloskey, P. (2008). Electromagnetic generator for harvesting energy from human motion.*Sensors and Actuators A: Physical, 147*(1), 248-253.

Sipahi, R., & Olgac, N. (2006). A unique methodology for the stability robustness of multiple time delay systems. *Systems & control letters,55*(10), 819-825.

Sodano, H. A., Inman, D. J., & Park, G. (2004). A review of power harvesting from vibration using piezoelectric materials. *Shock and Vibration Digest*, *36*(3), 197-206.

Sodano, H. A., Inman, D. J., & Park, G. (2005). Comparison of piezoelectric energy harvesting devices for recharging batteries. *Journal of Intelligent Material Systems and Structures*, *16*(10), 799-807.

Stephen, N. G. (2006). On energy harvesting from ambient vibration. *Journal of sound and vibration*, *293*(1), 409-425.

Talole, S. E., Ghosh, A., & Phadke, S. B. (2006). Proportional navigation guidance using predictive and time delay control. *Control Engineering Practice*, *14*(12), 1445-1453.

Tang, J., & Wang, K. W. (2001). Active-passive hybrid piezoelectric networks for vibration control: comparisons and improvement. *Smart Materials and Structures*, *10*(4), 794.

Tang, X., & Zuo, L. (2012). Simultaneous energy harvesting and vibration control of structures with tuned mass dampers. *Journal of Intelligent Material Systems and Structures*, *23*(18), 2117-2127.

Taylor, G. W., Burns, J. R., Kammann, S. M., Powers, W. B., & Wel, T. R. (2001). The energy harvesting eel: a small subsurface ocean/river power generator. *Oceanic Engineering, IEEE Journal of*, *26*(4), 539-547.

Udwadia, F. E., & Phohomsiri, P. (2006). Active control of structures using time delayed positive feedback proportional control designs. *Structural Control and Health Monitoring*, *13*(1), 536-552.

Vasques, C. M. A., & Rodrigues, J. D. (2006). Active vibration control of smart piezoelectric beams: comparison of classical and optimal feedback control strategies. *Computers & structures*, *84*(22), 1402-1414.

Vyhlídal, T., & Zítek, P. (2009). Mapping based algorithm for large-scale computation of quasi-polynomial zeros. *Automatic Control, IEEE Transactions on*, *54*(1), 171-177.

Vyhlídal, T., Olgac, N., & Kučera, V. (2014). Delayed resonator with acceleration feedback–Complete stability analysis by spectral methods and vibration absorber design. *Journal of Sound and Vibration*, *333*(25), 6781-6795.

Wang, K. W., Lai, J. S., & Yu, W. K. (1996). An energy-based parametric control approach for structural vibration suppression via semi-active piezoelectric networks. *Journal of vibration and acoustics*, *118*(3), 505-509.

Wu, S. Y. (1996, May). Piezoelectric shunts with a parallel RL circuit for structural damping and vibration control. In *1996 Symposium on Smart Structures and Materials* (pp. 259-269). International Society for Optics and Photonics.

Zuo, L., Scully, B., Shestani, J., & Zhou, Y. (2010). Design and characterization of an electromagnetic energy harvester for vehicle suspensions. *Smart Materials and Structures*, *19*(4), 045003.

Zuo, L., & Tang, X. (2013). Large-scale vibration energy harvesting. *Journal of intelligent material systems and structures*, *24*(11), 1405-1430.